

DRAFT VERSION JUNE 14, 2022

Typeset using L^AT_EX preprint style in AASTeX63

Meta-analysis of photometric and asteroseismic measurements of stellar rotation periods: the Lomb-Scargle periodogram, autocorrelation function, wavelet and rotational splitting analysis for 92 Kepler asteroseismic targets

YUTING LU,¹ OTHMAN BENOMAR ^{2,3} SHOYA KAMIKA ^{1,4} AND YASUSHI SUTO ^{1,3}

¹*Department of Physics, The University of Tokyo, Tokyo 113-0033, Japan*

²*National Astronomical Observatory of Japan, Mitaka, Tokyo 181-0015, Japan*

³*Research Center for the Early Universe, School of Science, The University of Tokyo, Tokyo 113-0033, Japan*

⁴*Daikin Industries, Ltd., Kita-ku, Osaka 530-8323, Japan*

(Received; Revised; Accepted)

Submitted to ApJ

ABSTRACT

We perform photometric (the Lomb-Scargle periodogram, autocorrelation, and wavelet) and asteroseismic analyses of 92 Kepler solar-like main-sequence stars to understand the reliability of the measured stellar rotation periods. We focus on the 70 stars without reported stellar companions, and classify them into four groups according to the quarter-to-quarter variance of the Lomb-Scargle period and the precision of the asteroseismic period. We present detailed individual comparison among photometric and asteroseismic constraints for these stars. We find that most of our targets exhibit significant quarter-to-quarter variances in the photometric periods, suggesting that the photometrically estimated period should be regarded as a simplified characterization of the true stellar rotation period, especially under the presence of the latitudinal differential rotation. On the other hand, there are a fraction of stars with a relatively small quarter-to-quarter variance in the photometric periods, most of which have consistent values for asteroseismically and photometrically estimated rotation periods. We also identify over ten stars whose photometric and asteroseismic periods significantly disagree, which would be potentially interesting targets for further individual investigations.

Keywords: asteroseismology – stars: rotation – stars: planetary systems – methods: data analysis – techniques: photometric

1. INTRODUCTION

Observational studies of stellar rotation play a fundamental role in understanding the physics of stars. The rotation rate of stars evolves substantially over their main-sequence stage due to a variety of angular momentum loss processes. Various empirical relations between the period, age and mass have been derived, known as gyrochronology (e.g. [Skumanich 1972](#); [García et al. 2014](#); [van Saders et al. 2016](#)). The determination of rotation periods for a large number of stars with different masses and ages is critical for verifying and understanding the physics behind these relations. In reality, stars are supposed to exhibit latitudinal and internal radial differential rotation. Thus the observed stellar rotation period is not a unique quantity, but should be interpreted as a weighted average dependent on specific observational methods.

Indeed, the rotation period of the Sun is known to vary along both latitudinal (via spectroscopy, e.g. [Howard & Harvey 1970](#)) and radial (via helioseismology, e.g. [Schou et al. 1998](#)) directions. The internal radiative core of the Sun ($r < 0.67R_{\odot}$) is well-approximated by a solid rotation of $P_{\text{rot}} \approx 27$ days. In contrast, beyond the transition region between the radiative and outer convective zones at $r \approx 0.7R_{\odot}$ (so-called tachocline), the rotation period P_{rot} becomes significantly dependent on the latitude ([Thompson et al. 2003](#)), varying from ≈ 25 days ($\ell = 0^\circ$) to ≈ 32 days ($\ell = 60^\circ$).

Such detailed rotational profiles, however, are poorly understood for other solar-like stars except the Sun. Furthermore, the Sun shows a magnetic activity cycle of 11-years, that is thought to be related to near-surface convection and stellar rotation (e.g. [Thompson et al. 2003](#); [Hartmann & Noyes 1987](#)). Due to this link, the large range of activity observed among stars suggest caution when interpreting the measures of rotation periods.

With the high precision photometry from Kepler and TESS, measurements of stellar rotation periods have been significantly improved in both quantity and accuracy. Since the starspots over the stellar surface are mainly responsible for the variation of stellar light intensity, the surface rotation period may be inferred from the photometric variations using the Lomb-Scargle periodogram (e.g. [Nielsen et al. 2013](#)), auto-correlation function (ACF, e.g. [McQuillan et al. 2013](#); [McQuillan et al. 2014](#)) and wavelet analysis (e.g. [García et al. 2014](#); [Ceillier et al. 2016](#)).

Note that those photometric measurements are sensitive to the observed distribution of spots on the stellar surface. The number of spots varies in a time-dependent manner due to the continuous creation and annihilation processes, and those spots spread over a range of different latitudes. All of them inevitably complicate the correspondence between the observed photometric variation and the stellar rotation in particular due to the stellar differential rotation. Furthermore, the photometric variation is produced solely by those spots located at the range of latitudes on the hemisphere visible to the observer. Thus, the measured rotation periods should depend on both the stellar inclination relative to the observer's line-of-sight and the non-stationary latitudes of the visible spots as discussed in detail by [Suto et al. \(2022\)](#).

Spectroscopic data of the stellar lines measure the projected rotation velocity $v \sin i_*$. If additional information for the stellar radius R and inclination i_* is available, it also provides an independent estimate for the stellar rotation period; further discussion is given in [Kamiaka et al. \(e.g. 2018\)](#).

Yet another complementary estimate for the stellar rotation period can be derived from asteroseismic analysis, which models the stellar oscillation pattern in power spectrum (e.g. [Kjeldsen & Bedding 1995](#); [Appourchaux et al. 2008](#); [Kamiaka et al. 2018](#); [García et al. 2019](#)). Unlike the photometric variation of the stellar light curves, asteroseismic analysis estimates the averaged rotation period over

a range of stellar latitude and radius. In this sense, the stellar rotation periods estimated with the two complementary methods do not have to be identical, depending on the degree of the differential rotation. In turn, the comparison of the two results for a sample of stars puts interesting constraints on the differential rotation, if the reliability of both measurements is confirmed.

It should be noted that the rotation profile of stars has been investigated using the high-quality photometry. Reinhold & Gizon (2015) attempted to detect surface differential rotation by studying significant peaks in the Lomb-Scargle periodogram for more than ten thousand Kepler stars. In addition, Benomar et al. (2018) measured the latitudinal differential rotation in the convection zones for 40 Sun-like stars by asteroseismology.

In this paper, we compute the rotation periods using three independent photometric methods (the Lomb-Scargle periodogram, auto-correlation function, and wavelet) for 92 Kepler Sun-like stars, which were selected as targets for asteroseismic analysis by Kamiaka et al. (2018). Nielsen et al. (2015) compared the rotation periods derived from the Lomb-Scargle and asteroseismic analyses, P_{LS} and P_{astero} , for their six Sun-like target stars, and found that they agree within the measurement uncertainty.

In the present study, we expand the sample size to 92 Kepler solar-type stars, and compute the stellar rotation period from three photometric methods. The reliability of such photometric rotation periods can be tested through the agreement among the three independent methods, while their variation in different quarters over four years may probe the latitudinal differential rotation as proposed by Suto et al. (2022). In addition, comparison against the asteroseismic estimates of the rotation periods may constrain the stellar inclination (Kamiaka et al. 2018; Kamiaka et al. 2019; Suto et al. 2019). Thus, the result enables us to evaluate the reliability of the measurements, as well as to extract the possible signature of, and/or put constraints on, their differential rotations.

The rest of the paper is organized as follows. Section 2 presents our sample of 92 Sun-like stars selected from the Kepler data, and the flow of our data processing. We identify 22 possible binary/multiple star systems. In section 3, we classify the remaining 70 stars into four groups according to the variance of the photometric rotation periods from the Lomb-Scargle analysis in different quarters, and the fractional uncertainties in the asteroseismic periods. Section 4 compares photometric and asteroseismic rotation periods for the 70 stars individually, while their statistical comparison among photometric analyses and between photometric and asteroseismic results is given in sections 5 and 6, respectively. Section 7 presents implications of our results. Finally, section 8 is devoted to summary and conclusions of the paper. In appendix, we describe our methods to estimate the rotation period, various comparison against previous results, the Lomb-Scargle periodograms and asteroseismic constraints for potentially interesting stars that are mentioned in the main text.

2. OUR SAMPLE AND DATA PROCESSING OF LIGHT CURVES

2.1. *Our sample of stars*

We use the sample of stars selected by Kamiaka et al. (2018). The sample includes the *Kepler* dwarfs LEGACY sample which consists of 66 stars with the best asteroseismic data so far in solar-type category (see e.g. Lund et al. 2017; Aguirre et al. 2017), and additional 28 KOI (Kepler Object of Interest) with detectable oscillation amplitudes. Kamiaka et al. (2018) performed an asteroseismic analysis of this sample, and estimated their stellar rotation periods and inclinations. Figure 1 plots the location of our targets on their surface gravity and effective temperature plane. Stellar evolutionary

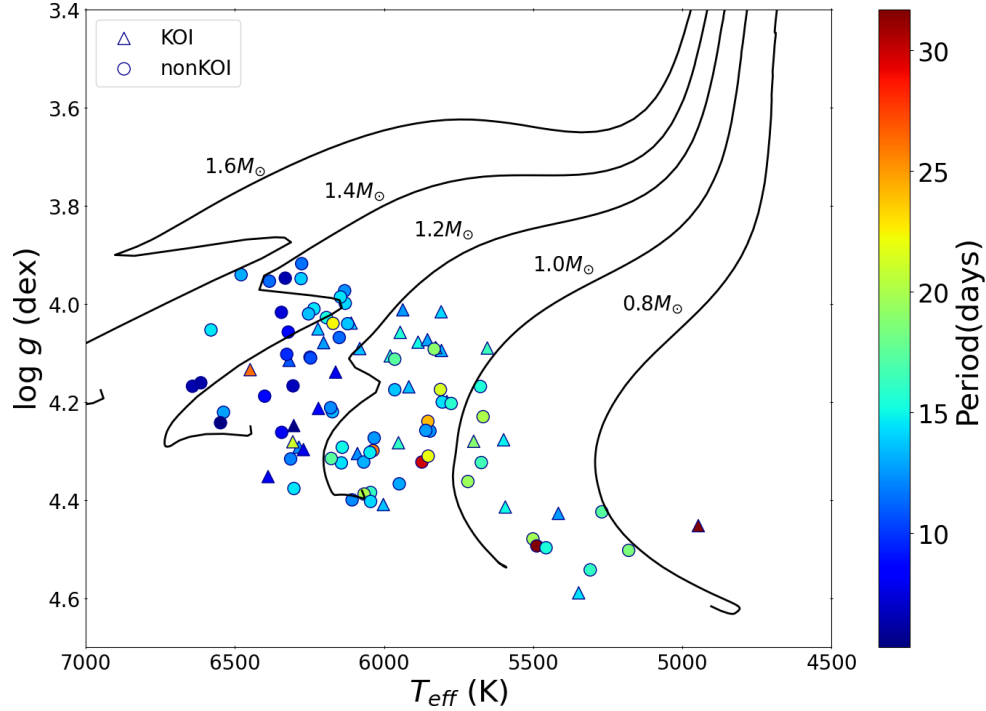


Figure 1. Log surface gravity in function of effective temperature for the 92 stars of our sample. Colors indicate the period measured with the LS method ($\langle P_{LS,q} \rangle$). Triangles are for KOI stars and circles for stars without planets. Indicative evolution tracks are at solar metallicity (solid black lines) for masses between $0.8M_{\odot}$ and $1.6M_{\odot}$.

tracks are computed with MESA code (Modules for Experiments in Stellar Astrophysics; Paxton et al. (2011)) for stars with initial mass of 0.8, 1.0, 1.2, 1.4, and $1.6 M_{\odot}$ from their pre-main-sequence phase to white dwarf phase, assuming the solar metallicity.

For the photometric analysis, we use the *Kepler* long-cadence PDC light curve (PDC-msMAP, Stumpe et al. 2014), Data Release 25, from Mikulski Archive for Space Telescope (MAST). The data consist of quarters of ~ 90 day duration with a cadence of 29.4 minutes over four years. We choose the light curves for Q2-Q14 quarters.

KOI-268 (KIC 3425851) has one of the best-quality light curves in our sample and a precisely determined photometric period (see Figures 4 and 44 below). We first compute the fraction of the available data for KOI-268 in each quarter, and find that it varies between 81 and 96 percents, with an average ~ 90 percents. Then, we remove those quarters for other stars if the corresponding fraction is less than 75% of the reference value for KOI-268, in order to secure the statistical significance of each quarter. Furthermore, we require that the targets must have at least 7 quarters of available data, which removes 16 Cyb A (KIC 12069424) and 16 Cyb B (KIC 12069449) from our sample. Thus, the number of our final targets for subsequent analyses becomes 92.

2.2. Preprocessing stellar light curves

We preprocess the light curves of the 92 stars before performing the photometric analysis, which is summarized in Figure 2.

In order to remove the systematic trend in the light curves, we first fit the original data $L_{\text{init}}(t)$ in each quarter to a 4-th order polynomial function $p_4(t)$. Then, we obtain the detrended light curves in

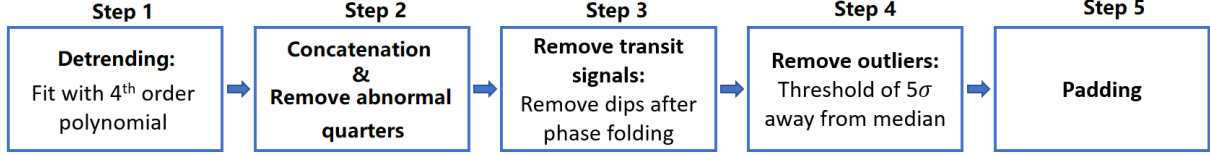


Figure 2. Flow chart of our preprocessing of stellar light curves.

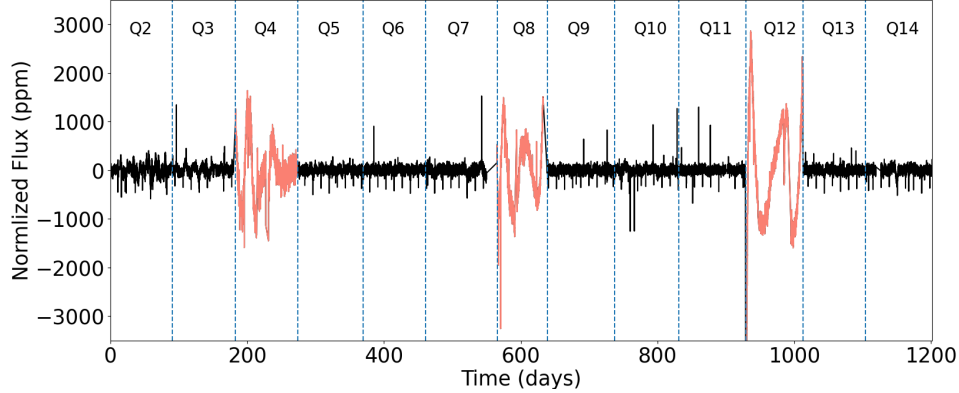


Figure 3. The detrended light curve of *Kepler*-1655 (KIC 4141376, KOI-280) for Q2 to Q14 quarters. We remove the three quarters, Q4, Q8, and Q12, in the subsequent photometric analysis, which exhibit anomalous variations illustrated in red.

units of the fitted polynomials separately in each quarter: $L(t) = L_{\text{init}}(t)/p_4(t) - 1$ (Step 1 of Figure 2).

Next, we concatenate the detrended light curves in available quarters between Q2 and Q14 for each target star into a single array of time series while preserving gaps between the quarters (Step 2 of Figure 2). We set the starting time of this series to be $t = 0$.

For several stars, the detrended light curves still exhibit large anomalous variations in some quarters. Figure 3 illustrates such an example for *Kepler*-1655 (KIC 4141376, KOI-280). The light curves in quarters Q4, Q8, and Q12 (plotted in red) show strange behavior that seems to be uncorrelated with nearby quarters. We suspect that they are due to unknown contamination or instrumental effects. Thus, we decided to remove those quarters if the median absolute flux variation in a particular quarter is three times larger than those of the neighboring quarters. We removed such anomalous quarters from six targets: *Kepler*-1655 (KIC 4141376, KOI-280), *Kepler*-100 (KIC 6521045), *Kepler*-409 (KIC 9955598, KOI-1925), KOI-72 (KIC 11904151), KIC 8694723, and KIC 10730618.

As shown in Figure 3, the detrended light curves also contain the dips due to the planetary transits (for KOI stars) and other possible outliers. We remove them according to the following procedure (Steps 3 and 4 of Figure 2).

In order to remove the periodic dips due to the planetary transit, we first fold the light curve using the orbital period of each planet candidate and remove the data for the transit epochs corresponding to the folded duration. We also remove the expected secondary eclipse signal from the light curve at the opposite phase assuming a circular orbit. Since the eclipse dips are invisible except for a few of our KOI targets, however, this procedure does not affect the estimate of the stellar rotation period

of the order of days. In addition, we remove outliers which are 5σ away from the median of the concatenated light curve for each target.

Incidentally, we are not able to detect the transit signal for KOI-5.02 and *Kepler*-37b after folding, and we do not remove any transit dips nor the expected eclipse dips. We suspect that KOI-5.02 is a false-positive, and Barclay et al. (2013) reported that the transit signal of *Kepler*-37b is less than 20 ppm. Thus possible transiting signals of these two targets would have negligible influence on the determination of stellar rotation period.

We note that the 90 day duration of each Kepler quarter effectively puts an upper limit of detectable periods around 45 days. Indeed, the rotation periods of main-sequence stars similar to our sample (Figure 1) are usually less than 50 days (e.g. Kamiaka et al. 2018). So, we apply our own box-car filter of a 50-day width even though the PDC-SAP light curves has applied smoothing to reduce long-term period systematics. Since the *Kepler* data is nearly evenly sampled, we map the light curve to a uniformly sampled grid at an interval of $\delta t = 29.4$ minutes.

Finally, we pad all removed portions in the light curves (removed quarters, planetary transits, secondary eclipses, outliers, and missing data) by Gaussian noise of zero mean and the variance of σ_{noise} that is computed from the detrended light curve for each target (Step 5 of Figure 2). We also tried the zero padding for comparison, and made sure that the two padding schemes hardly change the estimated values of the photometric rotation period, implying that the padding does not affect the result in reality.

2.3. Identification of Possible Binary/Multiple-star Systems

A significant fraction of stars are in multiple systems. The multiplicity may lead to a systematic bias on the rotation period estimated from the photometric variation of the target star. Thus, we try to identify possible members in binary and multiple-star systems in our sample.

For that purpose, we primarily adopt Renormalized Unit Weight Error (RUWE) value from Gaia DR3, which measures the goodness of fit with respect to a single-star model derived from the Gaia astrometry (Fabricius et al. 2021). A star with RUWE exceeding 1.4 is commonly suspected to have an unresolved companion (Evans 2018; Wolniewicz et al. 2021). We list 14 target stars with $\text{RUWE} \geq 1.4$ from the Gaia DR3 catalog as possible candidates of binary/multiple-star systems.

In addition, we identify three eclipsing binaries from *Kepler* Eclipsing Binary Catalogue¹, two binary systems from NASA Exoplanet Archive², four multiple-star systems and two binaries from Table 4 of García et al. (2014), one binary from Eylen et al. (2014), and one binary from Lillo-Box et al. (2014). Among the 13 systems, five stars have $\text{RUWE} \geq 1.64$, while the other eight stars have $\text{RUWE} \geq 1.05$.

In total, we identify 22 stars with possible companions, and summarize them in Table 2. We compute their photometric rotation periods in the same manner as other 70 stars with no reported stellar companion (Appendix A), but they may be interpreted with caution. We separately discuss seven KOI stars out of them in §7.2 since they may be potentially important targets for planetary studies. In what follows, however, we mainly focus on the other 70 stars; their estimated rotation periods are summarized in Tables 3, 4, 5 and 6.

3. CLASSIFICATION OF STARS

¹ *Kepler* EB catalogue <http://keplerebs.villanova.edu/>, last check 2021 November 14

² NASA Exoplanet Archive <https://exoplanetarchive.ipac.caltech.edu/index.html>, DOI: 10.26133/NEA6

We measure rotation periods using three different photometric methods, including the Lomb-Scargle (LS) periodogram, Auto-correlation function (ACF) and wavelet analysis (WA). The details of the photometric methods as well as a brief introduction to the asteroseismic analysis by Kamiaka et al. (2018) are provided in Appendix A. In this section, we classify the 70 stars based on photometric and asteroseismic results, in order to examine the reliability of the measured rotation period and/or to constrain the differential rotation. We adopt the LS measurement for the photometric classification, and use ACF and WA as complementary information to test the robustness of the derived rotation period.

3.1. Photometric classification based on the variance of rotation periods in different quarters

The rotation period estimated using the LS method for the q -th quarter $P_{\text{LS},q}$ may be different from the period P_{LS} computed for the entire observed duration T_0 . Distribution of starspots at different quarters should change with time due to the creation/annihilation processes over a range of latitudes. Thus, combined with their possible latitudinal differential rotation, each quarter may exhibit the fractional variation of the period on the order of ten percent.

If the typical lifetime of starspots is less than 90 days, their pattern on the surface at different quarters can be regarded as an uncorrelated realization drawn from the same statistical distribution. Even if the lifetime of starspots has a broad distribution, the variance of $P_{\text{LS},q}$ among different quarters would reflect the differential rotation for stars. This possibility has been theoretically studied by Suto et al. (2022) using analytic model and mock observations. It is also possible that the large variance is simply due to the low signal-to-noise ratio (*e.g.*, due to a very low number of spots or to the fact that the star is very faint) of the light curve for some quarters. These two possibilities could be distinguished by comparing the LS result with those based on ACF, WA, and asteroseismology on an individual basis (see §3.2 below).

In order to quantify the fractional variance of the rotation periods among different quarters, we introduce the following parameter Δ_{LS} for each star:

$$\Delta_{\text{LS}} = \frac{1}{N_Q \langle P_{\text{LS},q} \rangle} \sum_q |P_{\text{LS},q} - \langle P_{\text{LS},q} \rangle|, \quad (1)$$

where N_Q is the number of quarters with measured $P_{\text{LS},q}$, and $\langle \cdots \rangle$ denotes the median value operator.

Nielsen et al. (2013) proposed a similar indicator called MAD (Median Absolute Deviation) $\langle |P_{\text{LS},q} - \langle P_{\text{LS},q} \rangle| \rangle$. Our indicator, equation (1), differs from MAD in the following two ways. We use the *fractional* variance, which would be more appropriate in classifying stars with a broad range of rotation periods. In addition, we average the deviation over all the quarters because the median of deviation sometimes underestimates the real intrinsic variation of the distribution. This will be discussed below individually for each target.

After trial-and-errors, we classify the stars into two groups: Group A with $\Delta_{\text{LS}} \leq 0.20$ and Group B with $\Delta_{\text{LS}} > 0.20$. There are 23 stars in Group A and 47 stars in Group B, out of the 70 stars with no reported stellar companion; see §2.3. Figure 4 presents results of our photometric analysis for the reference star KOI-268 (KIC 3425851; see section 2) that is classified in Group A with $\Delta_{\text{LS}} = 0.014$, as well as for KIC 6116048 (Group B with $\Delta_{\text{LS}} = 0.372$).

Group A contains targets with a relatively robust periodic component in their light curves, and their P_{LS} values are reliably estimated from the prominent single peak as shown in the left panels of Figure 4.

In contrast, Group B, with $\Delta_{\text{LS}} > 0.20$, consists of two different types in general. The first type shows either a variation of measured periods among different quarters or multiple co-existing periodic signals (see *e.g.*, the right panels of Figure 4). Possible scenarios for the latter include differential rotation on stellar surface, harmonics (see §A.1.1), unresolved companions, residuals of a systematic trend, and other unknown contaminations. The second type shows very weak periodic signals, whose estimated periods are less reliable and subject to significant uncertainties.

Note that the large variation of period measurements for the first type of targets in Group B may not necessarily indicate that their rotation periods are unreliable, but could be due to the physical variation on stellar surface such as the differential rotation.

3.2. Classification based on asteroseismic analysis

We also classify our targets based on asteroseismically estimated periods by Kamiaka et al. (2018), in a complementary manner to the photometric classification. For that purpose, we adopt the ratio $\Delta P_{\text{astero}}/P_{\text{astero}}$, where ΔP_{astero} is the sum of upper and lower error of period estimation, *i.e.*, $\Delta P_{\text{astero}} = (\Delta P_{\text{astero}})_+ + (\Delta P_{\text{astero}})_-$; see equations (A7) and (A8) in §A.2.

We set the threshold value of 0.4 after trial-and-errors, and introduce two groups; Group a with $\Delta P_{\text{astero}}/P_{\text{astero}} \leq 0.4$ has 33 stars, while Group b with $\Delta P_{\text{astero}}/P_{\text{astero}} > 0.4$ has 37 stars.

<div>asteroseismology</div> <div>photometry</div>	Group <i>a</i>	Group <i>b</i>	Total
Group <i>A</i>	14 (7)	9 (4)	23 (11)
Group <i>B</i>	19 (3)	28 (12)	47 (15)
Total	33 (10)	37 (16)	70 (26)

Table 1. Groups A and B include stars with $\Delta_{\text{LS}} \leq 0.20$ and > 0.20 respectively from the LS result, while groups a and b contain stars with $\Delta P_{\text{astero}}/P_{\text{astero}} \leq 0.4$ and > 0.4 respectively from the asteroseismic result. The numbers in the parenthesis indicate the number of stars with planetary candidates (KOI catalogue).

Combining the photometric and asteroseismic classification yields four groups labeled as Aa, Ab, Ba, and Bb, which are summarized in Table 1. Figure 5 plots the locations of 70 stars on the $\Delta P_{\text{astero}}/P_{\text{astero}} - \Delta_{\text{LS}}$ plane, and the left and right panels of Figure 6 show the correlations between $\langle P_{\text{LS},q} \rangle$ and Δ_{LS} , and between P_{astero} and $\Delta P_{\text{astero}}/P_{\text{astero}}$, respectively.

4. REMARKS ON INDIVIDUAL STARS

We plot the rotation periods for 70 stars with no obvious stellar companion in Figure 7 (7 KOI stars in Group Aa), Figure 9 (7 non-KOI stars in Group Aa), Figure 10 (4 KOI stars in Group Ab), Figure 11 (5 non-KOI stars in Group Ab), Figure 12 (3 KOI stars in Group Ba), Figure 13 (16 non-KOI stars in Group Ba), Figure 14 (12 KOI stars in Group Bb), and Figure 15 (16 non-KOI stars in Group Bb).

In those figures, gray crosses indicate the values of $P_{\text{LS},q}$ for different quarters with the orange vertical lines being their median value $\langle P_{\text{LS},q} \rangle$, while the blue, green, red, and black dots with error-bars represent the values of P_{LS} , P_{ACF} , P_{WA} , and P_{astero} with their uncertainties defined in section A. Those values are summarized in appendix; Tables 3 (Group Aa), 4 (Group Ab), 5 (Group Ba), and

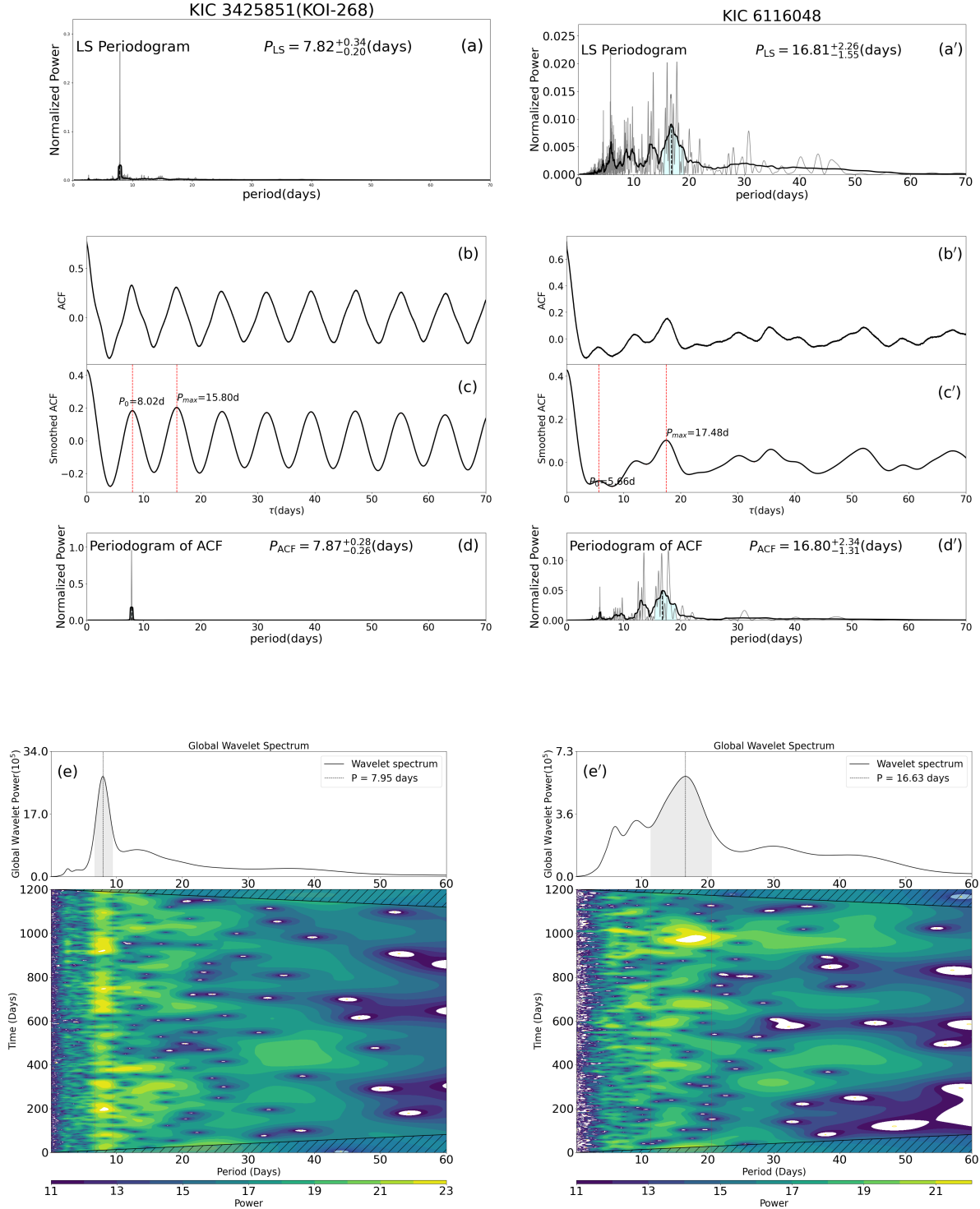


Figure 4. Results for KOI-268 (KIC 3425851; Group A with $\Delta_{LS} = 0.014$; panels a to e) and KIC 6116048 (Group B with $\Delta_{LS} = 0.372$; panels a' to e'). Panels a and a' show the LS periodogram. The middle panels are the ACF (b,b'), smoothed ACF (c,c'), and the LS periodogram of the smoothed ACF (d,d'), where P_0 denotes the period associated to the first maximum and P_{max} labels the period associated to the highest maximum. Panels e and e' show the WPS and GWPS from wavelet analysis.

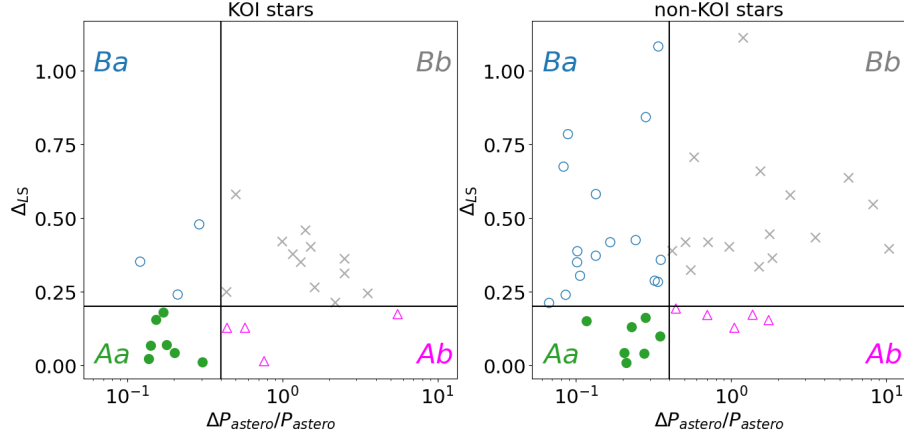


Figure 5. Classification of 70 targets on the $\Delta P_{\text{astero}}/P_{\text{astero}} - \Delta_{\text{LS}}$ plane. The solid lines indicate the thresholds, $\Delta_{\text{LS}} = 0.20$ and $\Delta P_{\text{astero}}/P_{\text{astero}} = 0.4$, that we adopt in the classification. Green filled circles, blue open squares, magenta open triangles, and gray crosses correspond to stars in Group Aa, Ba, Ab, and Bb, respectively.

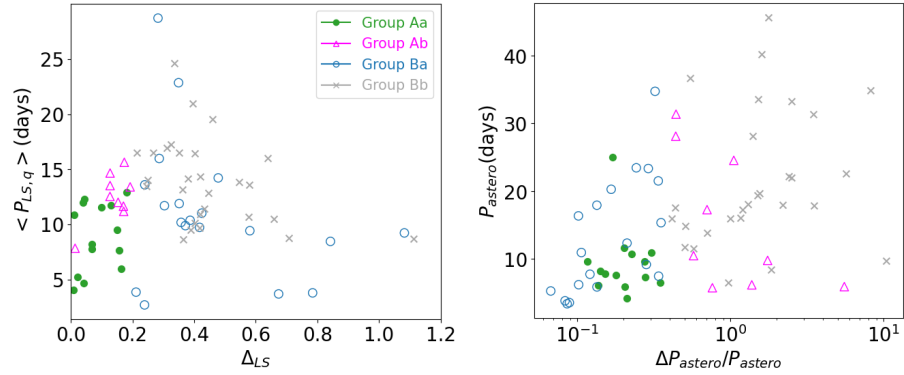


Figure 6. $\langle P_{\text{LS},q} \rangle$ against Δ_{LS} (left) and P_{astero} against $\Delta P_{\text{astero}}/P_{\text{astero}}$ (right). Green, blue, magenta, and gray symbols correspond to Groups Aa, Ba, Ab, and Bb, respectively.

6 (Group Bb). In those Tables, we quote the upper and lower error-bars with respect to the median value $\langle P_{\text{LS},q} \rangle$ by introducing

$$\Delta \langle P_{\text{LS},q} \rangle_+ \equiv \langle P_{\text{LS},q} - \langle P_{\text{LS},q} \rangle \rangle_+, \quad \Delta \langle P_{\text{LS},q} \rangle_- \equiv \langle \langle P_{\text{LS},q} \rangle - P_{\text{LS},q} \rangle_-, \quad (2)$$

where $\langle \dots \rangle_+$ and $\langle \dots \rangle_-$ denote the median operators for quarters with $P_{\text{LS},q} > \langle P_{\text{LS},q} \rangle$ and $P_{\text{LS},q} < \langle P_{\text{LS},q} \rangle$, respectively. For a majority of stars, equation (2) gives a very similar value of the Half Width at Half Maximum (HWHM) of the highest peak computed from the LS periodogram over the entire observation span. In some cases, however, it becomes much larger reflecting the significant skewness of the distribution of $P_{\text{LS},q}$. We adopt equation (2) as a complementary measure to emphasize the presence of such skewness, which are listed in Tables 3, 4, 5 and 6.

Before considering the statistical comparison and implications, we comment on individual results for a few targets in different groups. In the following discussion, we assume solid rotation for simplicity, and estimate the stellar rotation period P_{rot} from the spectroscopically determined rotation velocity

$v \sin i_*$:

$$P_{\text{spec}} = \frac{2\pi R}{v \sin i_*} \sin i_* \approx 50.6 \sin i_* \left(\frac{R}{R_\odot} \right) \left(\frac{1 \text{ km s}^{-1}}{v \sin i_*} \right) \text{ days}, \quad (3)$$

and from the asteroseismically determined rotation frequency $\delta\nu_*$:

$$P_{\text{astero}} \approx 11.6 \left(\frac{1 \mu\text{Hz}}{\delta\nu_*} \right) \text{ days}. \quad (4)$$

4.1. KOI stars in Group Aa: Kepler-100

As Figure 7 clearly indicates, KOI stars in Group Aa show good agreement among $\langle P_{\text{LS},q} \rangle$, P_{LS} , P_{ACF} , P_{WA} , and P_{astero} . Indeed, the major part of the scatter around $P_{\text{LS},q}$ for those stars is dominated by a small number of quarters with low signal-to-noise ratios.

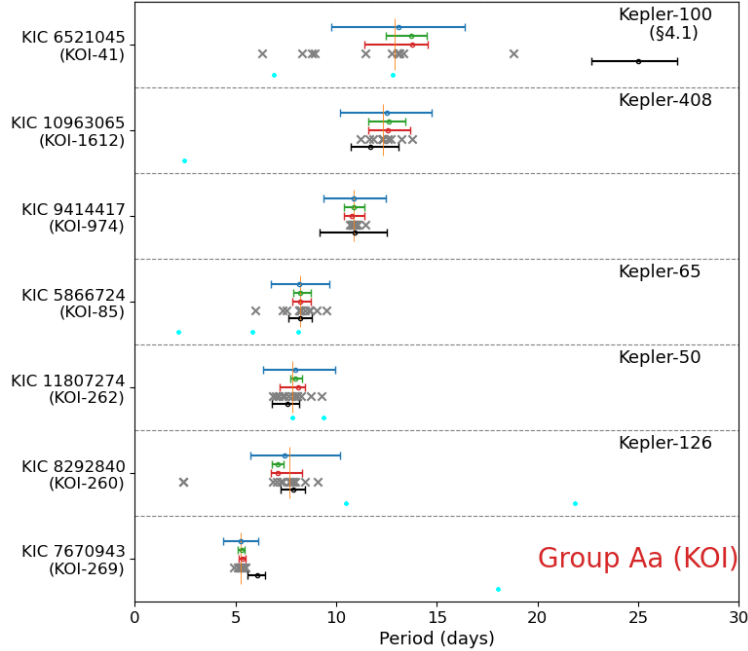


Figure 7. Rotation periods for seven KOI stars classified in Group Aa. We plot the values of $P_{\text{LS},q}$ for different quarters in gray crosses, with the orange vertical lines indicating their median value $\langle P_{\text{LS},q} \rangle$ for each target. For comparison, we show the other three photometric rotation periods, P_{LS} , P_{ACF} , P_{WA} , in red, green, and blue dots with error-bars (corresponding to their HWHMs), respectively. Black dots indicate the asteroseismic results P_{astero} with quoted errors representing the 16 and 84 percentiles. For reference we plot the orbital periods of transiting planets in each system as cyan dots.

The only exception is *Kepler-100* (KIC 6521045, KOI-41) with $\Delta_{\text{LS}} = 0.18$ that is close to our threshold value of 0.2. Its photometrically estimated periods ($\langle P_{\text{LS},q} \rangle$, P_{LS} , P_{ACF} , and P_{WA}) consistently point to ≈ 13 days, while $P_{\text{astero}} \approx 25$ days. Intriguingly, [McQuillan et al. \(2013\)](#) and [Ceillier et al. \(2016\)](#) concluded $P_{\text{ACF}} \approx 25$ days. Thus, we conduct a further examination of *Kepler-100*.

The LS periodograms of *Kepler-100* for different quarters (Figure 30) shows apparent variations in measured period. While it is not easy to define a robust period, six quarters (Q2, Q4, Q7, Q8, Q9, Q11) out of the 12 quarters (except Q6) have the highest peaks around 13 days. Our analysis excludes

Q6 because its median absolute flux variation is more than three times of those of the neighboring quarters (§2.2). Nevertheless, the quarter has a very strong peak at $P_{LS,q} \approx 25$ days. We found that our own P_{ACF} becomes ≈ 25 days if we include the Q6 data, which recovers the result of McQuillan et al. (2013) and Ceillier et al. (2016).

We refer to spectroscopic measurement of rotational velocity. According to Table 1 of Marcy et al. (2014), *Kepler*-100 have $v \sin i_* = 3.7 \text{ km s}^{-1}$ and $R = 1.49 \pm 0.04 R_\odot$. Thus equation (3) implies that $P_{\text{spec}} \approx 20.4 \sin i_*$ days. A value of $\sin i_* \sim 0.6$ is required to agree with $\langle P_{LS,q} \rangle \sim 13$ days, but it is inconsistent with the asteroseismic result of $\sin i_* \approx 1$ and $P_{\text{astero}} \approx 26.4^{+1.2}_{-1.7}$ days ($\delta\nu_* = 0.44^{+0.03}_{-0.02} \mu\text{Hz}$; see Figure 31).

We note that the orbital periods of its three transiting planets (Marcy et al. 2014) are 6.9 days (*Kepler*-100 b), 12.8 days (*Kepler*-100 c), and 35.3 days (*Kepler*-100 d), one of which are close to our measured rotation period (~ 13 days). We visual inspect the light curves to check whether our photometric estimate is somehow contaminated by the removal of the transit signal of *Kepler*-100 b. As Figure 8 suggests, however, the lightcurves exhibit clear periodic oscillations that are not aligned with the location of the transit dip. Therefore, it is unlikely to be an artifact of the transit signal removal.

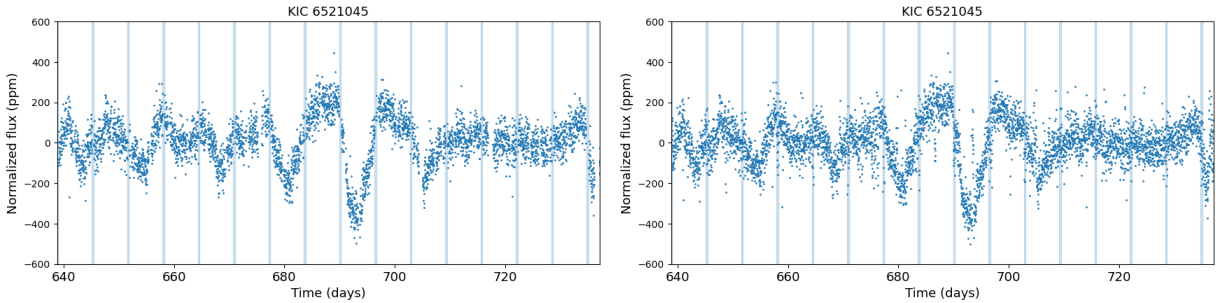


Figure 8. The lightcurve of *Kepler*-100 for Q9. Left and right panels show the lightcurves with no padding and Gaussian noise-padding. The vertical bars indicate the padded epochs corresponding to the primary transit and the secondary eclipse.

A possible explanation is that the 13-day period is the second harmonics of 25 days. The variation of the period in different quarters may suggest that *Kepler*-100 has multiple large active spots over the surface. Indeed, our visual inspection of light curve (Figure 8) shows a pattern of a deeper trough accompanied by a shallower trough. This pattern may be a signature of multiple spots, which leads to the presence of the harmonics (peak at $P_{\text{rot}}/2$) in periodogram. Without visual inspection, the automatic period detection method may the period associated with harmonics as the actual rotation period. In any case, we conclude that *Kepler*-100 remains as one of the intriguing systems that deserve for further investigation.

4.2. non-KOI stars in Group Aa: KIC 5773345

Photometric rotation periods $\langle P_{LS,q} \rangle$, P_{LS} , P_{ACF} , and P_{WA} agree within error-bars for all the non-KOI targets in Figure 9. In contrast, $P_{\text{astero}} \approx 6.5$ days of KIC 5773345 is a factor of two smaller than the photometrically derived values of 12 days. Thus, we examine KIC 5773345 in detail below.

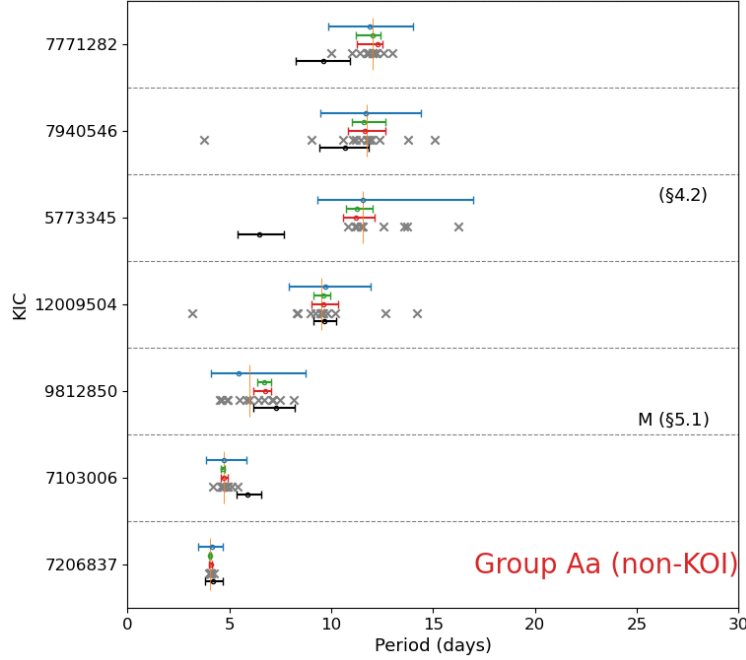


Figure 9. Same as Figure 7 but for seven non-KOI stars classified in Group Aa.

Figure 32 indicate that KIC 5773345 has persistent periodic signals of $P \sim 12$ days over the entire observed span (except for the removed quarters), while there is no significant signal around 6.5 days. Asteroseismic constraints on i_* and $\delta\nu_*$ for KIC 5773345 are shown in Figure 33.

Another complementary constraint on the rotation period P_{rot} is provided from the spectroscopic data. For KIC 5773345, Bruntt et al. (2012) and Molenda-Żakowicz et al. (2013) obtained $v \sin i_* = 6.6 \pm 1.46$ km/s and $v \sin i_* = 3.4 \pm 1.1$ km/s, respectively. The factor of two difference likely comes from the difficulty of modeling the turbulence as pointed out by Kamiaka et al. (2018); see their Figure 8. Adopting $R = 2.00^{+0.05}_{-0.07} R_\odot$ (Chaplin et al. 2013), equation (3) gives $P_{\text{spec}}/\sin i_* \approx 15.2^{+4.3}_{-2.8}$ days and $29.5^{+14.1}_{-7.2}$ days, respectively.

Our photometric estimate of $P_{\text{rot}} \sim 12$ days becomes consistent with $P_{\text{spec}}/\sin i_*$ of Bruntt et al. (2012) and Molenda-Żakowicz et al. (2013) if $\sin i_* \sim 0.8$ and $\sin i_* \sim 0.4$, respectively. Incidentally, it is known that the asteroseismology constrains the parameter $\delta\nu_* \sin i_*$ primarily, instead of $\delta\nu_*$ or $\sin i_*$ (Kamiaka et al. 2018). Substituting $\delta\nu_* \sin i_* = 0.93^{+0.1}_{-0.09} \mu\text{Hz}$ (Figure 33) into equation (4) implies $P_{\text{astero}}/\sin i_* = 12.5^{+1.3}_{-1.2}$ days, which agrees with the result of Bruntt et al. (2012) within their 1σ uncertainty while inconsistent with that of Molenda-Żakowicz et al. (2013).

Therefore, the discrepancy between our photometric and asteroseismic periods for KIC 5773345 may come from an intrinsic problem of asteroseismic analysis in separating $\delta\nu_* \sin i_*$ into $\delta\nu_*(=1/P_{\text{astero}})$ and $\sin i_*$ in asteroseismic analysis. In such case, the photometric estimate of $P \sim 12$ is likely the true rotation period. Nevertheless, it may be premature to conclude at this point, and KIC 5773345 should be regarded as another interesting target for follow-up observation.

4.3. KOI and non-KOI stars in Group Ab: Kepler-409, KIC 7970740, and KOI-268

In general, stars classified as Group Ab have consistent estimates for the photometric rotation period as shown in Figure 10. The asteroseismic measurements for group b targets have large uncertainties so

that targets do not show statistically significant discrepancy between photometric and asteroseismic periods, except for *Kepler*-409 (KIC 9955598, KOI-1925) and KIC 7970740.

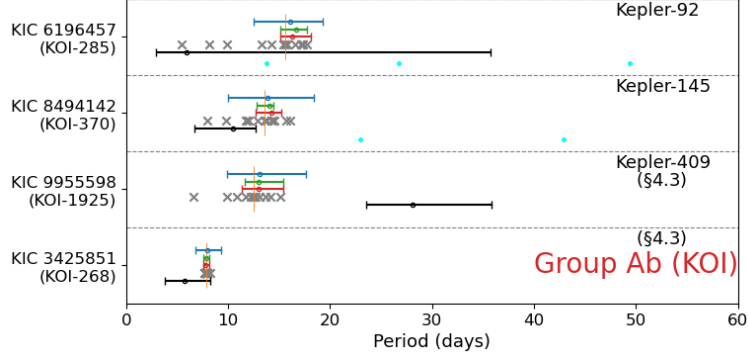


Figure 10. Same as Figure 7 but for six KOI stars classified in Group Ab.

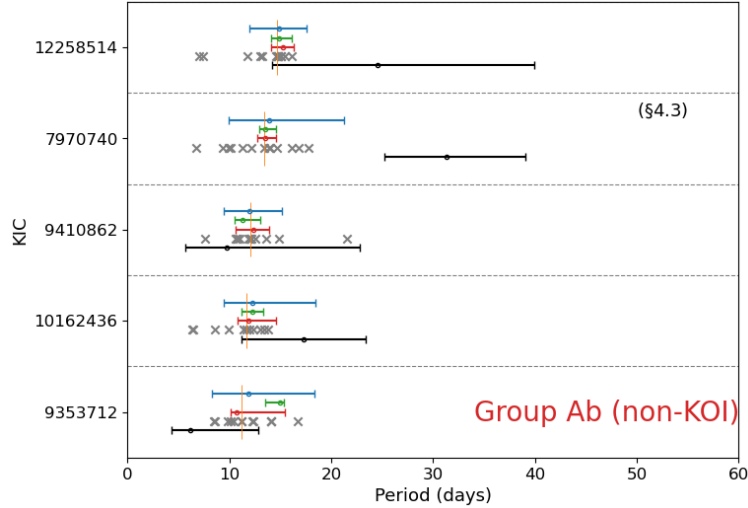


Figure 11. Same as Figure 7 but for five non-KOI stars classified in Group Ab.

For *Kepler*-409, photometric results consistently point to $P_{\text{rot}} \sim 13$ days, while $P_{\text{astero}} \sim 29$ days (Figure 40). We also refer to spectroscopic estimations for comparison. Equation (3) and (4) suggest that $P_{\text{spec}} \approx 22.3 \sin i_*$ days if $v \sin i_* = 2$ km/s (Marcy et al. 2014) while $P_{\text{astero}} \approx 37.4^{+4.0}_{-3.3} \sin i_*$ days for $\delta\nu_* \sin i_* = 0.31 \pm 0.03 \mu\text{Hz}$ (Figure 41).

For KIC 7970740, $P_{\text{LS},q}$ varies from 9 to 18 days (Figure 42), while $P_{\text{astero}} \sim 41.1^{+5.0}_{-4.0} \sin i_*$ days for $\delta\nu_* = 0.28 \pm 0.03 \mu\text{Hz}$ (Figure 43).

Another interesting target is KIC 3425851 (KOI-268) for which the photometric period is precisely measured (Figure 44). If we perform the asteroseismic analysis with the prior for $\delta\nu_*$ from photometric estimate, one may be able to constrain the stellar inclination more tightly; see Figure 45.

4.4. KOI stars in Group Ba: *Kepler*-25, 93, and 128

There are three planet-hosting stars in Group Ba (Figure 12). *Kepler*-25 (KIC 4349452, KOI-244) is one of the two transiting planetary systems for which the real spin-orbit misalignment angle has

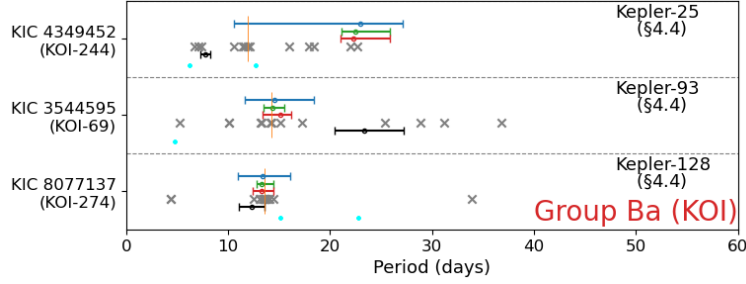


Figure 12. Same as Figure 7 but for three KOI stars classified in Group Ba.

been estimated jointly from the Rossiter-McLaughlin effect and asteroseismology (Benomar et al. 2014; Campante et al. 2016).

Figure 34 indicates that the photometric rotation period for *Kepler-25* varies significantly from quarter to quarter and not reliable. On the other hand, the asteroseismic rotation period seems to be very precisely estimated; $P_{\text{astero}} \approx 7.9^{+0.5}_{-0.4}$ days. Adopting $v \sin i_* \approx 9.5 \text{ km/s}$ and $R = (1.31 \pm 0.02)R_{\odot}$ (Marcy et al. 2014), $P_{\text{spec}} \approx 6.9 \sin i_*$ which is in rough agreement with P_{astero} .

Kepler-93 (KIC 3544595, KOI-69) also exhibits large variation in $P_{\text{LS},q}$ (Figure 36). Referring to spectroscopic measurement from (Marcy et al. 2014), we obtain $P_{\text{spec}} \approx 92 \sin i_*$ days with $v \sin i_* \approx 0.5 \text{ km/s}$ and $R = (0.92 \pm 0.02)R_{\odot}$. However, such a small value of $v \sin i_*$ is not so reliable as it is subject to a large uncertainty in turbulence modeling. On the contrary, asteroseismic analysis provides a relatively precise estimation of $P_{\text{astero}} \approx 23.3^{+0.5}_{-0.4}$ days (Figure 37).

Finally, we note that *Kepler-128* (KOI-274, KIC 8077137) is classified as Group B because of three apparent outliers, which are $P_{\text{LS},q} \approx 4$ days for Q11 and Q14 and $P_{\text{LS},q} \approx 32$ days for Q2. Except for the three quarters, $P_{\text{LS},q} \approx (13 - 14)$ days persistently, and indeed agrees well with $P_{\text{astero}} = 12.3 \pm 1.3$ days. Thus, *Kepler-128* had better be classified as Group A in reality.

4.5. non-KOI stars in Group Ba

Sixteen non-KOI stars in Group Ba exhibit a diverse distribution of periodicities in the LS periodogram at different quarters. Most of them have multiple peaks whose relative heights vary among different quarters so that it is not easy to determine the photometric rotation period robustly. We show two examples (KIC 6225718 and 9965715) in Figures 46 to 48. As examined in §4.4, P_{astero} is likely to provide better period estimate for stars in Group Ba.

Finally, we show the results for KOI and non-KOI stars in Group Bb (Figures 14 and 15), without discussing them individually.

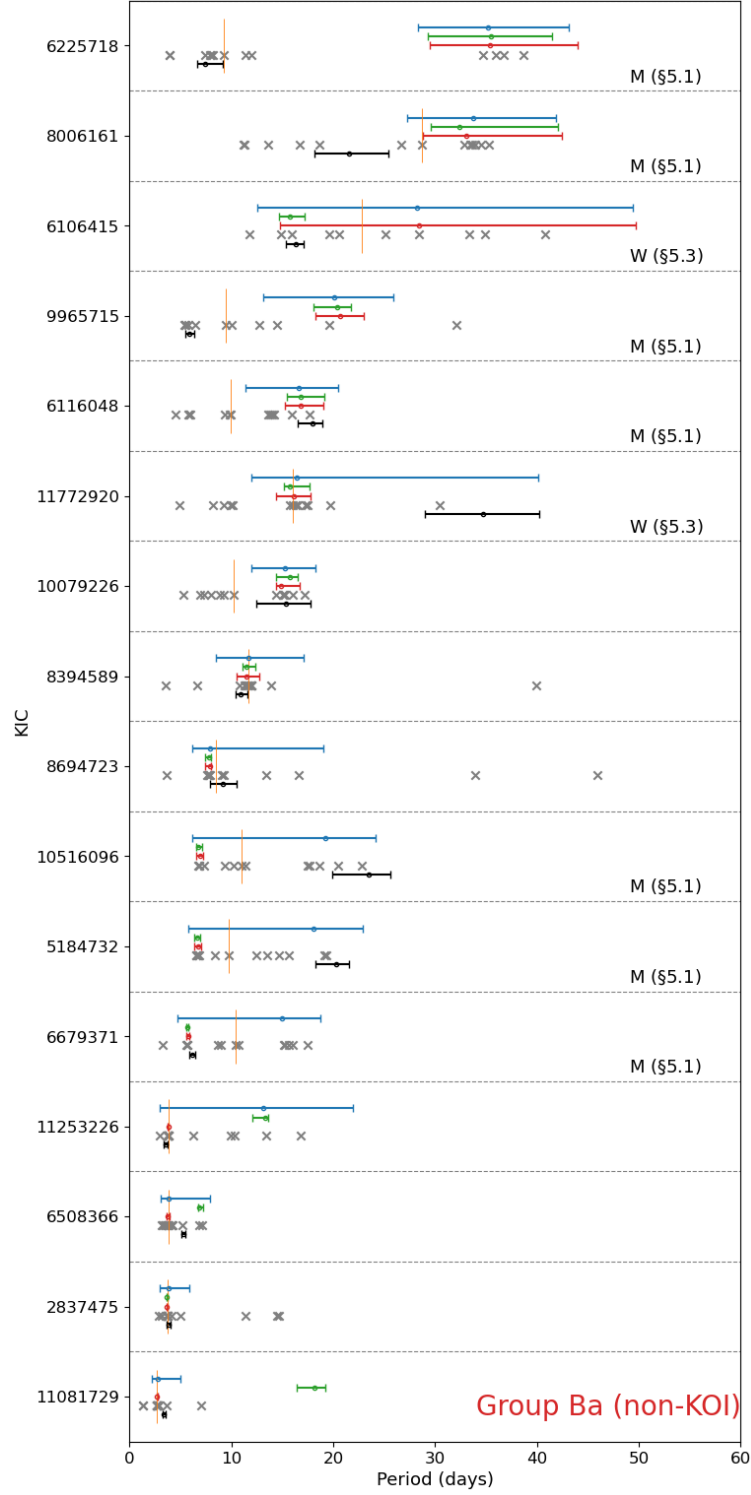


Figure 13. Same as Figure 7 but for 16 non-KOI stars classified in Group Ba.

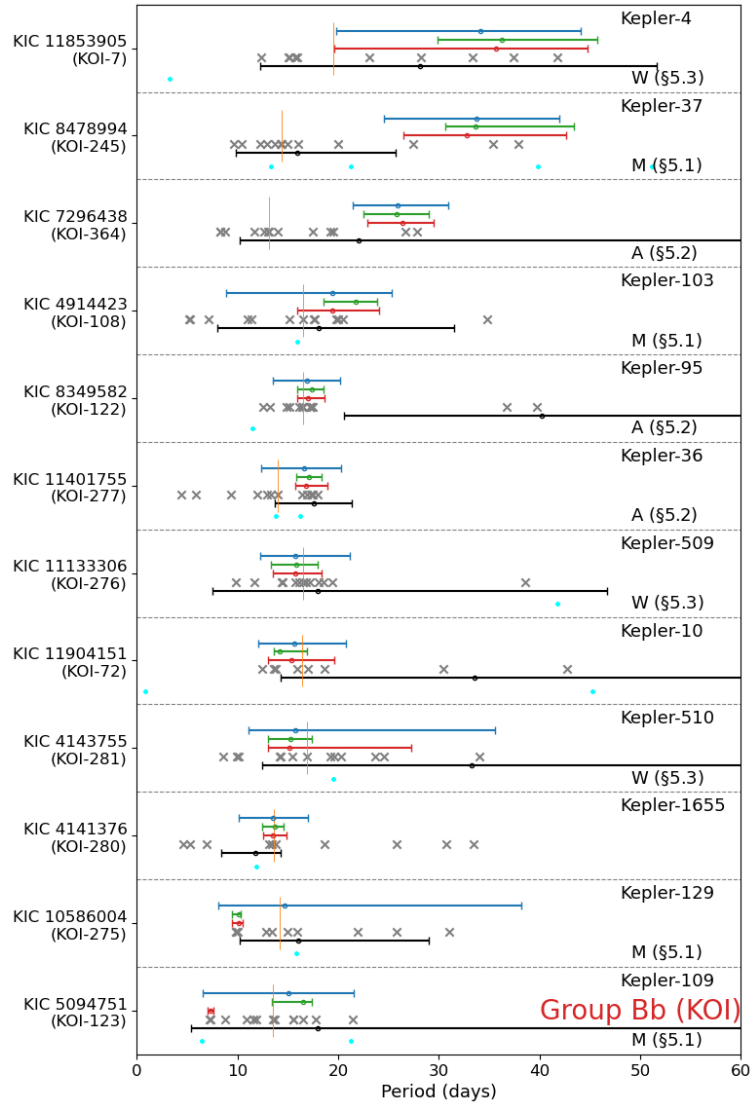


Figure 14. Same as Figure 7 but for 10 KOI stars classified in Group Bb.

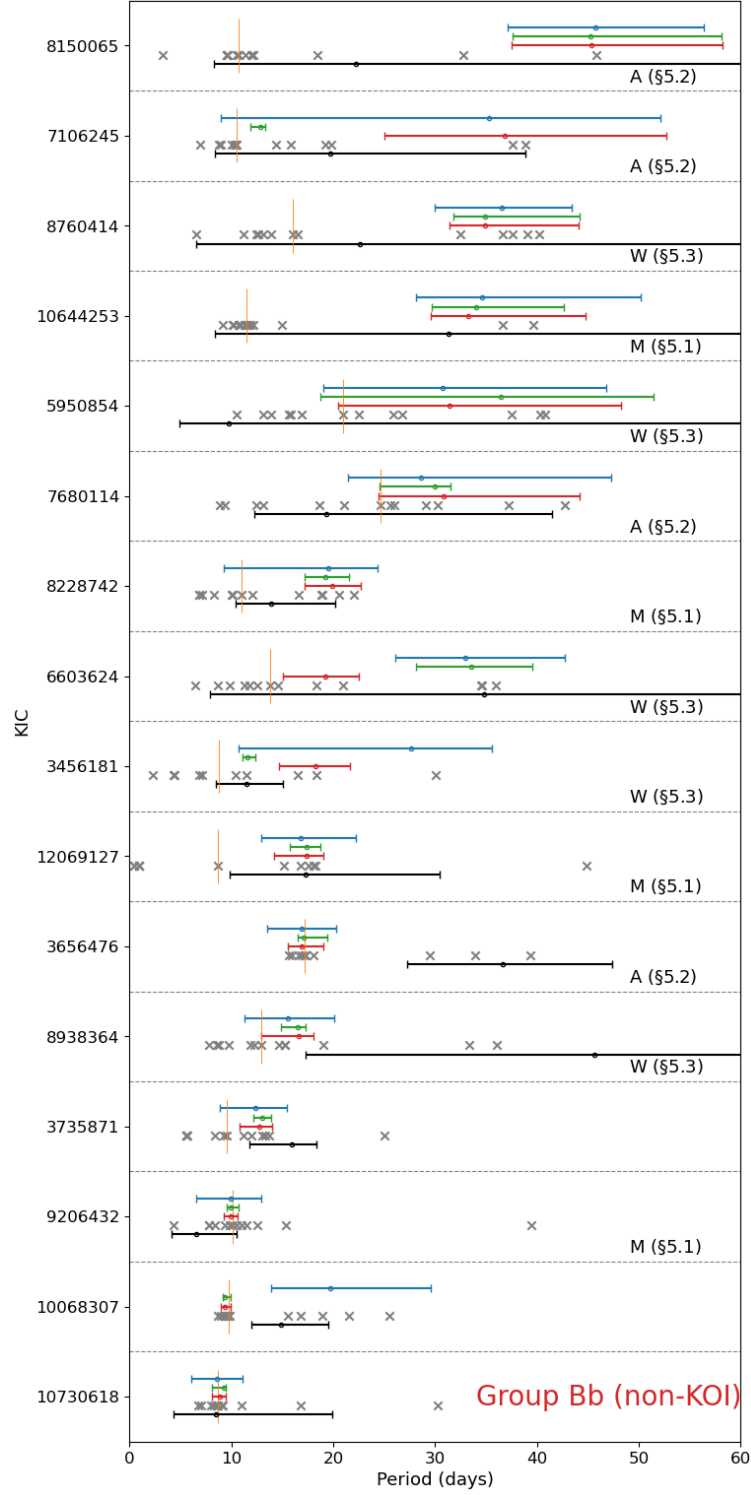


Figure 15. Same as Figure 7 but for 16 non-KOI stars classified in Group Bb.

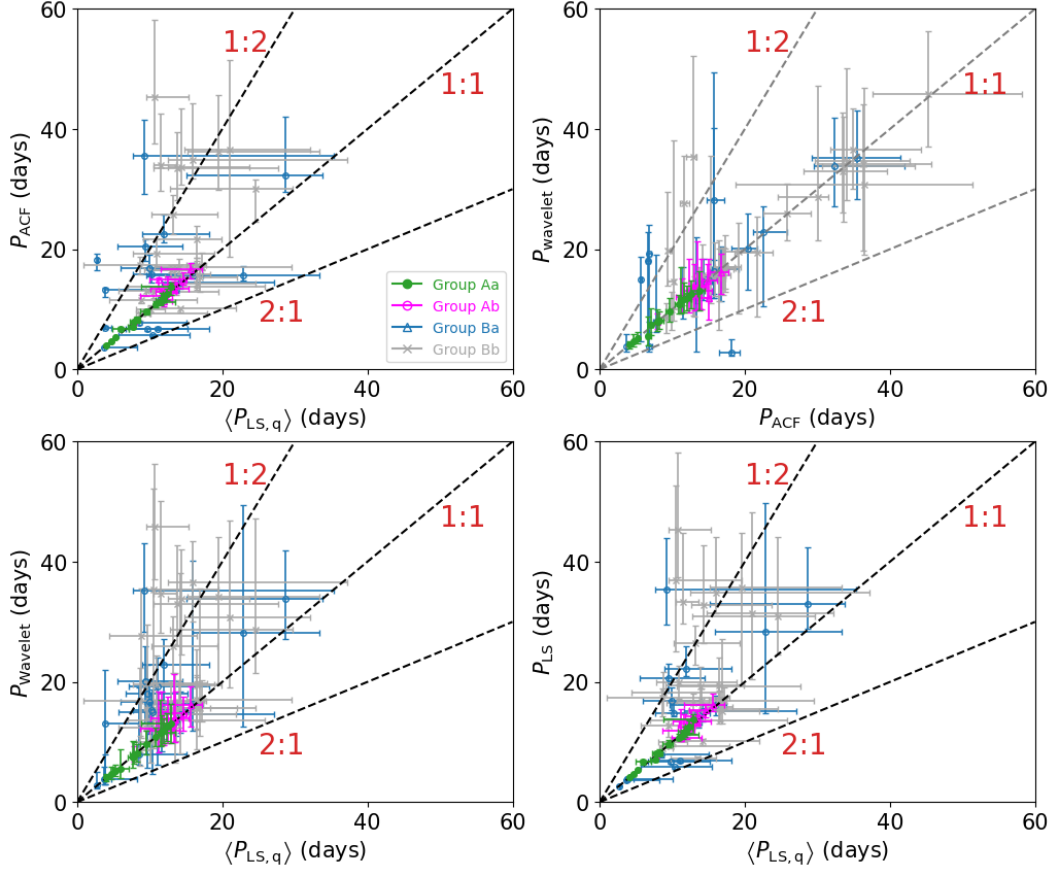


Figure 16. Comparison among four different photometrically measured rotation periods: P_{ACF} vs. $\langle P_{\text{LS},q} \rangle$ (upper-left), P_{WA} vs. P_{ACF} (upper-right), P_{WA} vs. $\langle P_{\text{LS},q} \rangle$ (lower-left), and P_{LS} vs. $\langle P_{\text{LS},q} \rangle$ (lower-right). We use green, magenta, blue and gray to represent stars in Groups Aa, Ab, Ba, and Bb, respectively.

5. COMPARISON AMONG PHOTOMETRIC ANALYSES

Figure 16 presents the comparison of the rotation periods P_{LS} , P_{ACF} , P_{WA} , and $\langle P_{\text{LS},q} \rangle$. The quoted error-bars for each method are computed according to the description in section A. Thus, they do not necessarily represent the same confidence level, and should be interpreted with caution.

We classified our targets based on Δ_{LS} defined by equation (1). Thus, the good agreement between P_{LS} and $\langle P_{\text{LS},q} \rangle$ for Group A is as expected; see the lower-right panel of Figure 16. On the other hand, agreement among P_{LS} , P_{ACF} , and P_{WA} implies that those photometrically measured periods are reliable and robust, at least for 23 stars in Group A. This should be kept in mind when we discuss the comparison against P_{astero} in subsection 6 below.

The majority of 47 targets in Group B still exhibit consistent rotation periods even though their error-bars are relatively large. Figure 16 shows that 8 stars have inconsistent estimates among P_{LS} , P_{ACF} , and P_{WA} ; after careful examination, we find five targets with multiple periodic components, two targets with an anomalous quarter, and one target with no clear periodic signal. We discuss those eight targets individually below.

5.1. Multiple periodic components: KIC 1108172, 11253226, 6508366, 10068307, 5094751

When multiple periodic components exist in the lightcurve, photometric analyses are not enough to discern the true rotation period. In such case, three different analyses assign different relative power to candidate peaks in spectra which occasionally leads to inconsistencies in period detected. For instance, the GWPS is known to increase the power of the fundamental period of a signal (Ceillier et al. 2017), and the ACF method uses a Gaussian smoothing to suppress the short-term modulation including the possible influence of harmonics. Thus both of them may be biased toward a longer period. Here, we provide our interpretation for 5 stars that exhibit multiple periodic components and have different estimates among P_{LS} , P_{ACF} , and P_{WA} .

- KIC 11081729 and 11253226: their P_{LS} is much shorter than P_{ACF} . The visual inspection of their wavelet power spectra indicates that the short period component persists more than half of the entire observed time span. Thus, P_{LS} is more likely to represent their true rotation periods.
- KIC 6508366 and 10068307: they both have two components roughly different by a factor of two. For KIC 6508366, the shorter period component is observed in the wavelet spectra for all quarters, while the longer period is visible only for a few quarters. For KIC 10068307, in contrast, the two components exist simultaneously within all of the quarters. Thus, we interpret the longer period corresponding to P_{LS} as the true rotation period, while the shorter period being its second harmonics.
- KIC 5094751 (*Kepler*-109, KOI-123): It has multiple periodic components in Q4 and Q6 with P_{LS} being longer than both P_{ACF} and P_{WA} ; see also the right panel of Figure 4. It could be due to a complex spot configuration and/or stellar surface differential rotation, and we can not be certain about which represents the true rotation period.

5.2. Abrupt increase of photometric variation in a single quarter: KIC 3456181, 7106245

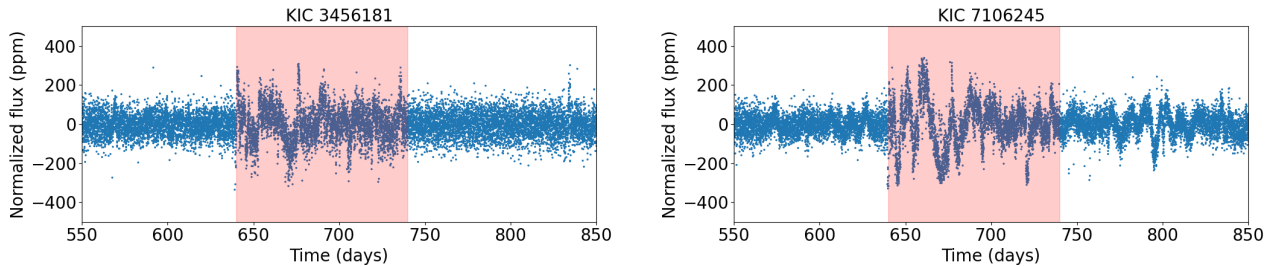


Figure 17. Part of quarters of light curves of KIC 3456181 and KIC 7106245. The shaded region mark the anomalous quarters where the flux variation suddenly increases.

As described in Section 2.2, using a systematic method, we removed anomalous quarters whose median absolute flux variations are three times larger than those of the neighboring quarters for six targets in total; *Kepler*-1655 (KIC 4141376, KOI-280), *Kepler*-100 (KIC 6521045), *Kepler*-409 (KIC 9955598, KOI-1925), KOI-72 (KIC 11904151), KIC 8694723, and KIC 10730618. The goal is to reduce the risk of having a biased measurement. However, among the stars for which the procedure does not detect anomalous quarters (that is, stars for which no quarter removal is performed), there

still remains some irregular and abrupt increases in flux, though less prominent, which may affect the estimation of the rotation period.

These abnormal parts might be partly due to residual systematics, or a contamination from other neighbor sources. Such abnormal variation usually give a dominating peak in the power spectrum, over-weighting other weaker peaks that are more likely associated with the actual rotational signals. Examples of this type of light curves are given in Figure 17, whose shaded region shows a strong but transient flux variation. We visual inspect the wavelet spectra of the two given targets and notice that measured low frequency peaks (~ 27 days in P_{WA} for KIC 3456181 and ~ 35 days in P_{WA} and P_{LS} for KIC 7106245) are associated with the abnormal regions instead of periodic modulation that we look for. In such circumstance, $\langle P_{LS,q} \rangle$ is less biased by those abnormal quarters.

For all targets in our sample with abrupt increase in flux variation, we check the module and channel number of the abnormal quarters to see whether it comes from a specific CCD plate. However, we notice that such abrupt variations are found in various modules and channels. In addition, we check the position of image on the plate and ensure that the location of image is not around the edge. It is natural to think of the increase in variation as the modulation from a large spot. Nevertheless, known that the lifetime of a spot scales with its size, abrupt variations which last for only 30-40 days seems less likely to be the lifetime of a large spot. Alternatively, such abnormal variation could be the residual of systematics like 30-day re-orientation of telescope. Especially, for relatively 'quiet' stars with few active regions, there is barely any rotational modulation in the light curve. The residual of systematics would become significant and act like a sudden increase in flux variation.

5.3. Weak or ambiguous periodic variation: KIC 6603624

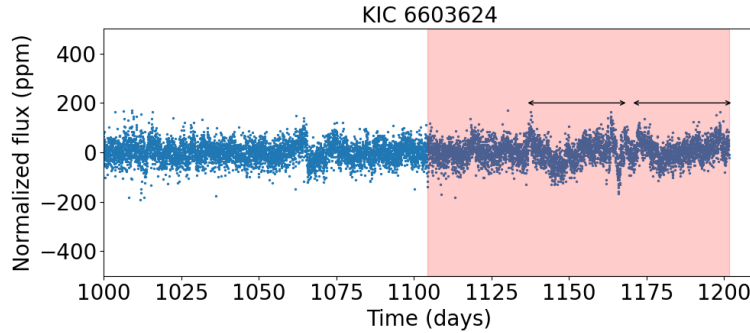


Figure 18. Part of light curves for KIC 6603624, and the shaded region corresponds to Q14. Two black arrows indicate the locations of possible 30-day periodic signal.

Figure 18 illustrates part of light curves for KIC 6603624 as an example of stars exhibiting a weak flux variation. The WA power spectrum for this type of targets is generally very noisy, and we find that it is simply dominated by the peak at $P \sim 32$ days in Q14 alone for KIC 6603624. As Figure 18 indicated, however, it lasts just for two cycles and it is not clear if it should be interpreted as a rotational feature. Thus, for this type of targets, the *measured* period is very unreliable, and should be taken with caution. We identify eight such targets with weak or ambiguous periodic components, and label them by “W” in the ‘Remark’ column of Table 3, 4, 5, and 6.

6. COMPARISON BETWEEN PHOTOMETRIC AND ASTEROSEISMIC ESTIMATES

Figure 19 compares the rotation period of our targets derived from asteroseismic analysis by [Kamiaka et al. \(2018\)](#) against our four photometric estimates: $\langle P_{LS,q} \rangle$ (upper-left), P_{LS} (upper-right), P_{ACF} (lower-left), and P_{WA} (lower-right). Figure 20 plots 17/19 stars whose $\langle P_{LS,q} \rangle$ and P_{astero} do not agree within their uncertainties defined by equations (2), (A7) and (A8). Since we have already discussed most of the 17 targets in §4, we do not repeat such discussion here on an individual basis, but present a few general conclusions below.

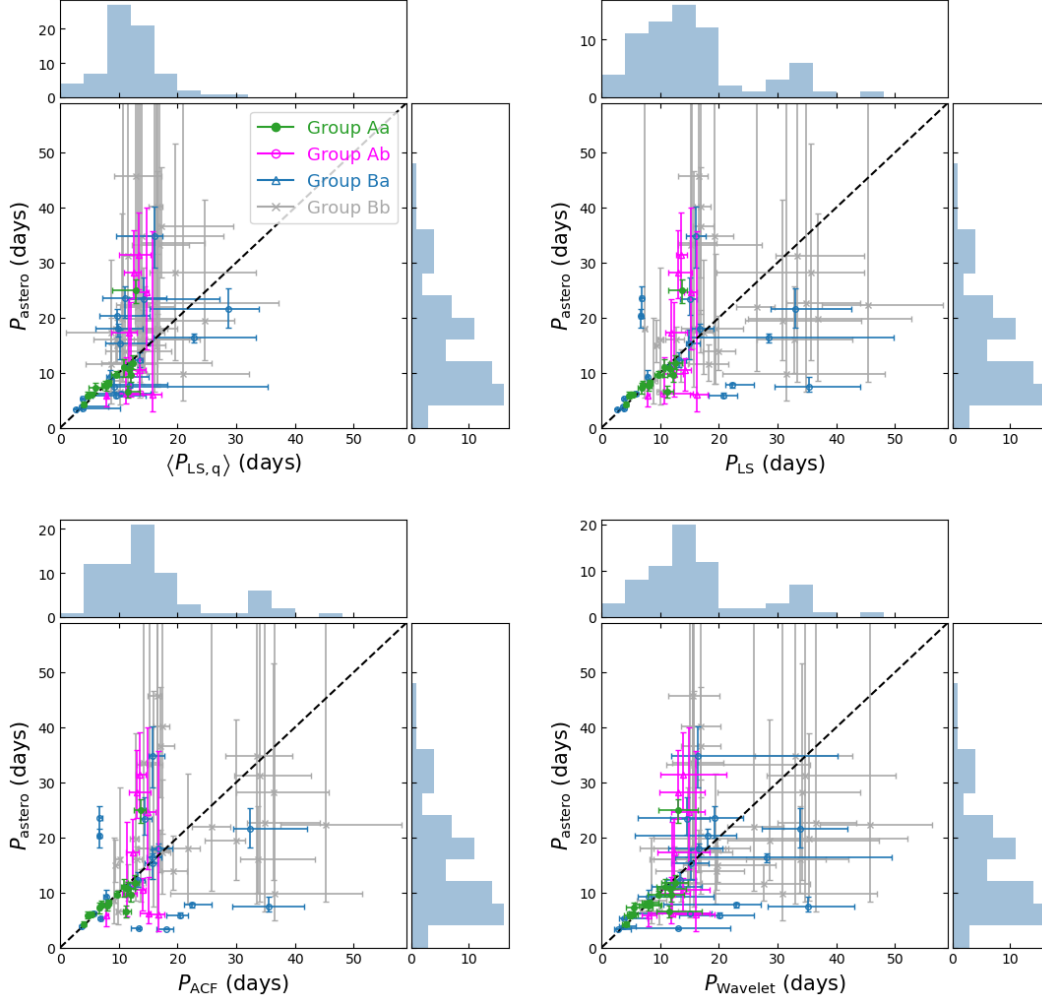


Figure 19. Comparison of P_{astero} against photometrically derived rotation periods; $\langle P_{LS,q} \rangle$ (upper-left), P_{LS} (upper-right), P_{ACF} (lower-left), and P_{WA} (lower-right). Green, blue, magenta, and gray symbols with error-bars correspond to Groups Aa, Ba, Ab, and Bb, respectively.

First, stars classified as Group Aa are in good agreement except *Kepler-100* (§4.1). While it is quite expected from the definition of our classification scheme, it is still encouraging. Second, there exist a population of stars whose P_{astero} is approximately twice of the corresponding photometric estimate. For those stars in Group Ba, P_{astero} is likely to be the true period. For those in Group Ab, on the other hand, it may not necessarily imply that $\langle P_{LS,q} \rangle$ is closer to the true value due to a possible bias toward shorter period for $\langle P_{LS,q} \rangle$.

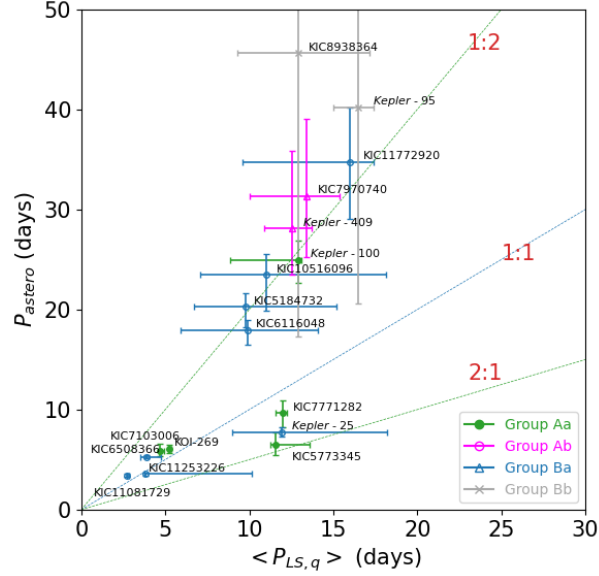


Figure 20. $\langle P_{LS,q} \rangle$ versus P_{astero} for 17 targets. There are 19 targets that do not agree within their uncertainties, but we do not plot *Kepler*-100 and *Kepler*-409 here because part of their quarters are removed during the lightcurve processing. Green, blue, magenta, and gray symbols with error-bars correspond to Groups Aa, Ba, Ab, and Bb, respectively.

Of course, the difference between $\langle P_{LS,q} \rangle$ and P_{astero} may point to an interesting physical effect, instead of an unknown artifact. Photometric estimates are based on the stellar surface variation, and thus sensitive to the latitudinal and size distribution of starspots, as well as other surface activities, while asteroseismic analysis is supposed to provide an averaged rotation period over a range of latitudes and depths inside the star. On the other hand, Figure 20 seems to suggest a tendency of $P_{astero} \sim 2\langle P_{LS,q} \rangle$. This may be interpreted that $\langle P_{LS,q} \rangle$ represents the second harmonics of the true rotation period of P_{astero} , as already pointed out by [García et al. \(2013\)](#). If confirmed, it implies the importance of the complementary visual inspection of automatic photometric analyses.

7. DISCUSSION

7.1. Possible implications for differential rotation

Figures 7 to 15 show that a majority of our targets have a range of different values of $P_{LS,q}$ in different quarters. The origin of those variations is not easy to identify, and may be a combination of stellar surface activity, instrumental effect, and unknown noise/contamination.

Of course, the variation of $P_{LS,q}$ could be of physical origin, at least for some targets. The most likely possibility includes an effect of the latitudinal differential rotation coupled with the surface distribution and dynamics of starspots. For instance, the presence of n active regions along the same latitude would result in significant peaks with the n -th harmonics of the rotation period in the LS periodogram. Such alias would outweigh the fundamental rotation period if such active regions are equally spaced along the same latitude band (e.g. [Chowdhury et al. 2018](#)). Furthermore, the co-existence of dark spots (the central darker part, *umbra*, and surrounding lighter part, *penumbra*) and brighter spots (*faculae*) may cancel out part of the photometric variation, which complicates the extraction of the true rotational signal. Our Sun is an example of stars with complex surface configuration (frequent appearance of multiple active regions) which leads to unstable and occasionally

low variability in both chromospheric and photometric measurements (see e.g. Donahue et al. 1996; Reinhold et al. 2020). As Donahue et al. (1996) pointed out, it is very likely solar-like star with similar surface configuration to our Sun may not pass the threshold for reliable detection of rotation period.

Consider a simple model of the latitudinal differential rotation (Reiners & Schmitt 2003; Hirano et al. 2012):

$$\omega(\ell) \approx \omega_{\text{eq}}(1 - \alpha \sin^2 \ell), \quad (5)$$

where $\omega(\ell)$ is the angular velocity of the stellar surface at latitude ℓ , ω_{eq} is its value at the equator ($\ell = 0$), and α is a parameter characterizing the strength of the differential rotation. For the Sun, $\alpha \approx 0.2$.

In order to proceed further, we need to assume the size and latitude distribution functions of starspots and their dynamics (migration over the stellar surface and creation/annihilation timescales), which is unknown. Suto et al. (2022) examined the variation of $P_{\text{LS},q}$ assuming that the spot distribution in each quarter is independently drawn from the empirical distribution to match the observed flux modulation of the Sun.

For simplicity, we may equate our Δ_{LS} to the variation of $\alpha \sin^2 \ell$ in equation (5). Furthermore, if the spot latitude ℓ_{spot} varies between 0° and 45° , $\Delta_{\text{LS}} \sim \alpha/2$. Thus, in principle, we may estimate α individually for our targets. In reality, however, most of the variation of $P_{\text{LS},q}$ in Figures 7 to 15 are very diverse, implying that the differential rotation combined with the spot distribution may not be dominant except for stars exhibiting modest variations. While we do not conduct further quantitative examination, *Kepler*-408, KOI-974, *Kepler*-50, KOI-269, KIC 7103006, KIC 7206837, and KOI-268 may be potentially interesting targets for tightly constraining their differential rotation.

7.2. KOI stars in stellar binary/multiple systems

We have 22 stars with possible stellar companions (§2.3). Since their lightcurves might be contaminated by the companions, we exclude them from our main analysis. Nevertheless, we examine seven KOI stars in this subsection because they may have interesting implications for their planetary architecture. Figure 21 plots their rotation periods in the same manner as Figure 7. Among them, we select the following three stars that are potentially interesting, the LS periodogram and asteroseismic constraints of which are shown in §C.11, §C.12, and §C.13.

Kepler-2 (HAT-P-7, KOI-2, KIC 10666592) is one of the two transiting planetary systems along with *Kepler*-25 for which the real spin-orbit misalignment angle has been estimated jointly from the Rossiter-McLaughlin effect and asteroseismology (Benomar et al. 2014; Campante et al. 2016). In reality, however, it is not easy to identify its rotation period photometrically from Figure 50. On the other hand, $P_{\text{astero}} \approx 12$ days from Figure 51 seems to be a reliable estimation of rotation period. This is a good example of the complementary power of asteroseismology.

Kepler-410 (KOI-41, KIC 8866102) has precise estimates for both photometric and asteroseismic rotation periods, but their values are very different ($\langle P_{\text{LS},q} \rangle \sim 4P_{\text{astero}}$). Intriguingly, Figure 52 indicates that the LS periodograms for all quarters have persistent secondary peaks at ≈ 10 days, which is very close to the second harmonics of the starspot modulation analytically predicted by Suto et al. (2022). Thus, it is possible that $\langle P_{\text{LS},q} \rangle \approx 20$ days, instead of $P_{\text{astero}} \approx 6$ days, is the true rotation period of *Kepler*-410. On the other hand, *Kepler*-410 is a binary system (Van Eylen et al.

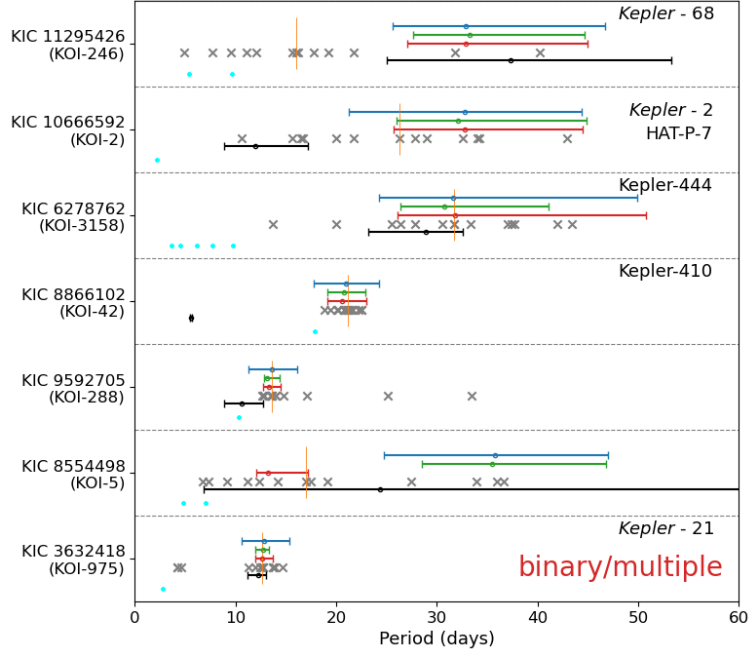


Figure 21. Same as Figure 7 but for 7 KOI stars in stellar binary/multiple systems.

2014), and it is also likely that either asteroseismic or photometric analyses may be contaminated by the companion star to some extent.

Finally, $\langle P_{LS,q} \rangle$ and P_{astero} of KOI-288 (KIC 9592705) agree within their error-bars. Figure 54 shows that its photometric periods are very robust. Thus, the joint photometric and asteroseismic analysis of KOI-288 may put a tighter constraint on its inclination. Incidentally, this is an example of systems whose P_{astero} is close to the orbital period of the planetary companion (Suto et al. 2019), although it may be just by chance.

7.3. Photometric and asteroseismic rotation periods as a function of stellar effective temperature

Stars lose the angular momentum through magnetic winds, and the loss rate is supposed to be sensitive to the depth of the convective zone, and therefore to their mass and effective temperature. Indeed, it is known observationally that stars with $T_{\text{eff}} < 6200\text{K}$ have a thicker convective envelope and much slower rotation rate than those with $T_{\text{eff}} > 6200\text{K}$ (Kraft 1967). Winn et al. (2010) found that hot Jupiters around stars with $T_{\text{eff}} < 6200\text{K}$ prefer the orbital axis well-aligned to the stellar spin axis, and proposed that the spin-orbit alignment results from the stronger tidal interaction between close-in giant planets and their host stars with a thicker convective envelope.

Figure 22 plots the photometric and asteroseismic rotation periods against the stellar effective temperature. We adopt the SDSS T_{eff} from Table 7 of Pinsonneault et al. (2012) for 60 stars. Our result is basically consistent with Figure 3 of Hall et al. (2021) and qualitatively reproduce the Kraft break. On the other hand, our targets with $P_{\text{astero}} > 30$ days often have smaller values of $\langle P_{LS,q} \rangle$ and may not properly represent the surface rotation period. Furthermore, the uncertainties of the asteroseismic measurements seem to be anti-correlated with T_{eff} (see Figures 19 and 20).

7.4. Stellar inclinations as a function of stellar effective temperature

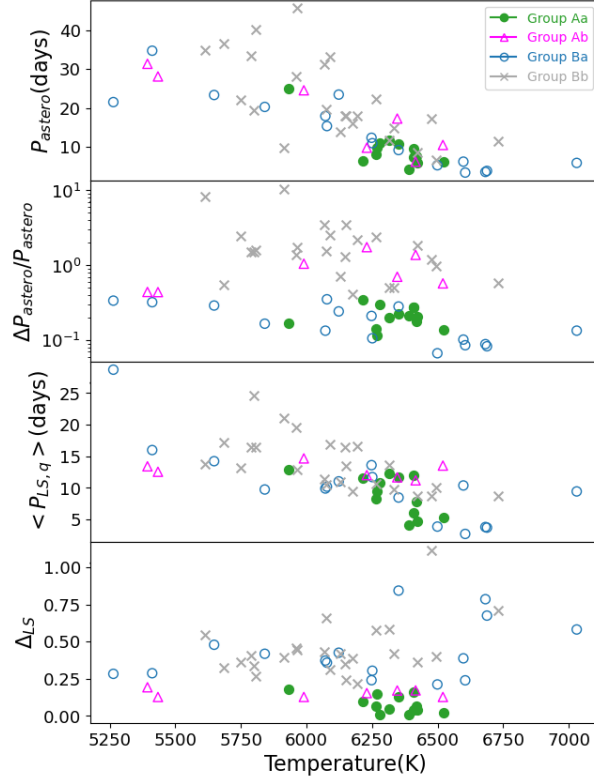


Figure 22. Stellar rotation periods against the effective temperature. From top to bottom, P_{astero} , $\Delta P_{\text{astero}}/P_{\text{astero}}$, $\langle P_{\text{LS},q} \rangle$, and Δ_{LS} are plotted as a function of the stellar effective temperature. Green, blue, magenta, and gray symbols correspond to Groups Aa, Ba, Ab, and Bb, respectively.

Finally, we study the stellar inclination as it could be an indicator of misalignment for planetary systems observed by transit and also has an imprint of the genesis of the stars. The stars are considered as a single population, from which we seek to identify the underlying distribution of stellar inclination and its dependence with temperature. The adopted criteria is the $\sin i$, which is obtained following the method described below.

For the asteroseismic sample of stars, we directly convert the posterior distribution of i_* by Kamiaka et al. (2018), and compute the distribution of $\sin i_{*,\text{astero}}$. For the spectroscopic determination of $\sin i_{*,\text{spec}}$, it is required to use equation (3), which depends on R , P_{spec} (substituted by the photometric rotation period P_{LS} for the current purpose) and $v \sin i_*$. Furthermore, it is necessary to consider the distribution functions of R and P_{LS} and $v \sin i_*$. Here, we assume uncorrelated Gaussian distributions for R and $v \sin i_*$ with their mean being the measured value and standard deviation being its 1σ error. Finally, in order to evaluate the distribution of the period, we directly use the LS periodogram of P_{LS} as the underlying probability distribution. However, we only use a range of the LS periodogram that spans over a slice that is twice the HWHM around the highest peak. This distribution is also normalised by integration over the considered range mentioned above. All of the probability distributions of the variables being defined, we then compute the distribution of $\sin i_{*,\text{spec}}$ via Monte Carlo sampling of R , P_{LS} and $v \sin i_*$.

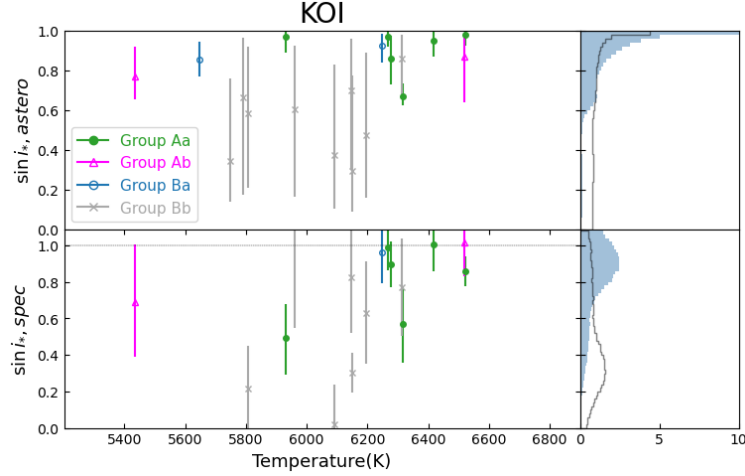


Figure 23. Stellar inclination $\sin i_*$ against the effective temperature for KOI stars. Left panels plot the values of $\sin i_*$ derived from asteroseismology (Kamiaka et al. 2018) and the photo-spectroscopic method adopting spectroscopic $v \sin i$ values from California-Kepler Survey Petigura et al. (2017) and Huber et al. (2013). Green, blue, magenta, and gray symbols with error-bars correspond to Groups Aa, Ba, Ab, and Bb, respectively. Right panels show the distribution functions of $\sin i_*$; black lines consider all stars, while shaded regions correspond to stars in Groups Aa, Ba and Ab excluding the least reliable Group Bb.

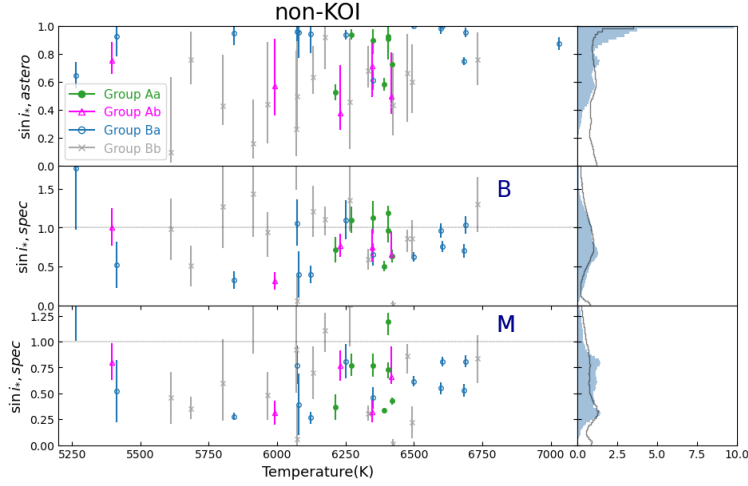


Figure 24. Same as Figure 23 but for non-KOI stars. Spectroscopic $v \sin i$ values for deriving $\sin i_{*,spec}$ are adopted from Lund et al. (2017), Molenda-Żakowicz et al. (2013), Bruntt et al. (2012) and Brewer et al. (2016). For some targets, there are more than one available $v \sin i$ values. In the second panel, we adopt Bruntt et al. (2012) if there are both $v \sin i$ from Bruntt et al. (2012) and from other literature. In the third panel, we use $v \sin i$ from Molenda-Żakowicz et al. (2013) if multiple values are available.

Left panels of Figure 23 plot $\sin i_{*,astero}$ and $\sin i_{*,spec}$ for KOI stars against the stellar effective temperature following the same procedure as described in Kamiaka et al. (2018) (in their Section 5.3), while right panels show the corresponding distribution functions.

Although the sample of KOI stars is small, we note that if one excludes stars from Group Bb (the least reliable stars), KOIs tend to have $\sin i_*$ clustered around unity, and that spectroscopy and seismology are in good agreement. This indicates that a majority of stars with planets show a

preference for a spin-orbit alignment, which is consistent with the previous conclusion by Kamiaka et al. (2018).

Figure 24 focuses on non-KOI stars. Excluding stars from Group Bb, $\sin i_{*,\text{astero}}$ exhibits a broader distribution compared to KOI stars. We note that the distribution is not uniform in $\sin i_*$ as it would be expected if there was no preference in their rotational spin direction on the sky. As shown by Kamiaka et al. (2018), asteroseismology overestimates inclinations below $i \simeq 30^\circ$, corresponding to $\sin i_* \lesssim 0.5$. This is likely the cause for a lack of population with reliable measurement when $\sin i_* < 0.4$. In addition, as pointed out by Kamiaka et al. (2018), available spectroscopic measurements are unreliable for some stars, in particular when the $v \sin i_*$ is low (due to the dominance of the stellar turbulence). Therefore, spectroscopic results from Molenda-Żakowicz et al. (2013) and from Bruntt et al. (2012) sometimes lead to a mathematically inconsistent result of $\sin i_* > 1$. If we exclude these impossible cases, there is no clear preferential stellar inclination. This is again consistent with an isotropic distribution of stars and contrasts with results from the KOI case shown in Figure 24.

8. SUMMARY AND CONCLUSIONS

We have performed a comprehensive photometric and asteroseismic analysis of 92 solar-like main-sequence stars observed by *Kepler*. We focus on 70 stars that do not have stellar companions, and classify them in four groups (Aa, Ab, Ba, and Bb) according to the fractional variance and precision of the rotation periods $\langle P_{\text{LS},q} \rangle$ and P_{astero} ; see §3.1 and 3.2. We have presented detailed comparison among photometric and asteroseismic constraints for those stars on an individual basis.

Group Aa has 14 stars with robust estimates for both $\langle P_{\text{LS},q} \rangle$ and P_{astero} . Twelve out of the 14 stars have $\langle P_{\text{LS},q} \rangle \approx P_{\text{astero}}$ as expected. The remaining two include *Kepler*-100 ($\langle P_{\text{LS},q} \rangle \approx 13$ days and $P_{\text{astero}} \approx 25$ days), and KIC 5773345 ($\langle P_{\text{LS},q} \rangle \approx 12$ days and $P_{\text{astero}} \approx 6.5$ days); see §C.1 and C.2. They are potentially interesting targets for further study. Group Ab has 9 stars. For these stars, $\langle P_{\text{LS},q} \rangle$ is consistent with P_{astero} , except for *Kepler*-409 and KIC 7970740; see §C.6 and C.7.

There are 19 stars in Group Ba and 28 stars in Group Bb. Since their photometric rotation periods vary from quarters to quarters, it is not easy to assign definite rotation periods photometrically. For stars in Group Ba, P_{astero} provides a better estimate for the true rotation period without being affected by the stellar surface activity. It is interesting to note that the stars for which photometric and asteroseismic periods are different exhibit a tendency of $P_{\text{astero}} \sim 2\langle P_{\text{LS},q} \rangle$ (Figure 20). This may imply that $\langle P_{\text{LS},q} \rangle$ represents the second harmonics of the true rotation period of P_{astero} , at least for some of those stars.

We find that there are 4 KOI stars in our sample whose rotation period agrees with the orbital period of their planetary companion; *Kepler*-65 (Group Aa), *Kepler*-50 (Group Aa), *Kepler*-1655 (Group Bb), and KOI-288. Due to a limited number of our sample, this may be simply a statistical fluke and not definitive, but could imply a possible interaction between the star and planet in those systems (Suto et al. 2019).

Most of stars exhibit significant quarter-to-quarter variations of $P_{\text{LS},q}$, which come from the combined effects of the differential rotation, various stellar surface activities, and other noises. Among them, 7 targets including *Kepler*-408, KOI-974, *Kepler*-50, KOI-269, KIC 7103006, KIC 7206837, and KOI-268 may be potentially interesting in constraining their differential rotation.

Our main findings are summarized as follows.

1. Most of our targets exhibit significant quarter-to-quarter variances in the photometric periods. This is reasonable, given the complicated dynamics and activities of the stellar surface and starspots. Thus, the estimated photometric period should be regarded as a simplified characterization of the true stellar rotation period, especially under the presence of the latitudinal differential rotation.
2. There is a fraction of stars with a relatively small quarter-to-quarter variance in the photometric periods (Group A; 23 out of 70 stars in our sample), for which the three photometric methods (the Lomb-Scargle periodogram, autocorrelation function, and wavelet analysis) enable the precise determination of the stellar rotation period in a consistent manner. Furthermore, it is encouraging that the asteroseismic rotation period for most of those stars agrees with the photometric rotation period within their uncertainties. Thus, rotation periods for stars satisfying our photometric classification condition should be reliable and accurate even without the asteroseismic estimate (that is not available in most cases).
3. Rotation periods more than ~ 30 days either photometrically or asteroseismically are not reliable in our *Kepler* sample. They may suffer from some residual systematics or correspond to the harmonics, and should be interpreted with caution.
4. There are over ten stars whose photometric and asteroseismic periods are not consistent. They should be potentially interesting targets deserved for further individual investigations.

We would like to note that the large variability observed in some stars and reflected by our classification might be further explored in another study. Indeed, in some stars and through a spot modeling, it may be possible to estimate the latitudes of the spots, their migration over time and the stellar rotation profile.

ACKNOWLEDGMENTS

We gratefully acknowledge the support from Grants-in Aid for Scientific Research by the Japan Society for Promotion of Science (JSPS) No.18H012 and No.19H01947, and from JSPS Core-to-core Program “International Network of Planetary Sciences”. We thank S. Aigrain for providing simulated Kepler light curves introduced in Aigrain et al. (2015).

This research made use of Astropy,³ a community-developed core Python package for Astronomy (Astropy Collaboration et al. 2013, 2018), Lightkurve, a Python package for Kepler and TESS data analysis (Lightkurve Collaboration et al. 2018), Waipy, a Python package for wavelet analysis (Mabelcalim 2014), Matplotlib (Hunter 2007), Astroquery (Ginsburg et al. 2019), tesscut (Brasseur et al. 2019) and pandas (Wes McKinney 2010).

APPENDIX

³ <http://www.astropy.org>

A. METHODS TO ESTIMATE THE STELLAR ROTATION PERIOD

There are a variety of methods to identify the periodicity in the photometric variations of the light curve. Among them, the Lomb-Scargle (LS) periodogram, autocorrelation function (ACF), and wavelet analysis (WA) have been applied extensively to the high-quality photometric data from space missions including *Kepler*.

For instance, [Nielsen et al. \(2013\)](#) applied the LS periodogram to 12,151 *Kepler* main-sequence stars and detected their rotation periods. [McQuillan et al. \(2014\)](#) measured rotation periods of 34,030 *Kepler* main-sequence stars using autocorrelation function. [García et al. \(2014\)](#) estimated the rotation period of 310 solar-like stars by combining autocorrelation function and wavelet analysis. Finally, we consider the asteroseismic rotation periods obtained by [Kamiaka et al. \(2018\)](#).

Even though those methods have been widely used in the literature, they may have their own advantage and disadvantage. Thus, we compute the rotation periods separately derived from the four methods. The detailed comparison of the resulting values is useful in understanding their robustness and reliability. In what follows, we briefly describe the basic principle of the four methods, together with typical examples of their outputs.

A.1. Photometric analysis

A.1.1. The Lomb-Scargle periodogram

The LS periodogram is one of the most popular methods to detect periodic signals embedded in the data ([Lomb 1976](#); [Scargle 1982](#)). Specifically, we adopt the generalized LS periodogram by [Zechmeister & Kürster \(2009\)](#), which fits the data to a single -mode sinusoidal function of frequency f and a constant term. We denote the resulting best-fit squared residuals at each frequency as $\chi^2(f)$. In the present paper, we adopt the standard normalization:

$$P(f) = \frac{\chi_0^2 - \chi^2(f)}{\chi_0^2}, \quad (\text{A1})$$

where χ_0^2 is the best-fit squared residuals with respect to a non-varying constant reference model.

We compute equation (A1) for each target at frequencies:

$$f_n = f_{\min} + n \delta f (< f_{\max}), \quad (\text{A2})$$

where n is an integer, and we set $f_{\min} = (71\text{day})^{-1} = 0.16\mu\text{Hz}$ and $f_{\max} = (0.24\text{day})^{-1} = 48\mu\text{Hz}$ so as to cover the range of the rotation period of the solar-type stars. The frequency interval δf is set to be $(n_0 T_0)^{-1}$, where T_0 is the total time span of the light curve for each star (typically $\sim 1200\text{days}$), the oversampling factor n_0 is chosen to be 20 (see [VanderPlas 2018](#), e.g.).

Finally, we smooth the periodogram sampled at f_n using a box-car filtering over $0.1 \mu\text{Hz} = (116\text{days})^{-1}$ to suppress the spurious discreteness effect in the frequency space.

Figure 25 shows an example of the LS periodogram in time domain, *i.e.*, $P(T) \equiv P(f = 1/T)$. We identify the highest peak in the smoothed periodogram, and estimate the LS rotation period P_{LS} and the associated errors $(\Delta P_{\text{LS}})_+$ and $(\Delta P_{\text{LS}})_-$ from the peak location and the corresponding HWHM (half width at half maximum) as illustrated in the vertical line and boundaries in the blue shaded region of Figure 25.

We repeat the same procedure using the light curve for the q -th quarter (each with $T_0 \approx 90$ days) separately, and obtain $P_{\text{LS},q}$ ($q = 2, \dots, 14$). As we discuss extensively below, the distribution of

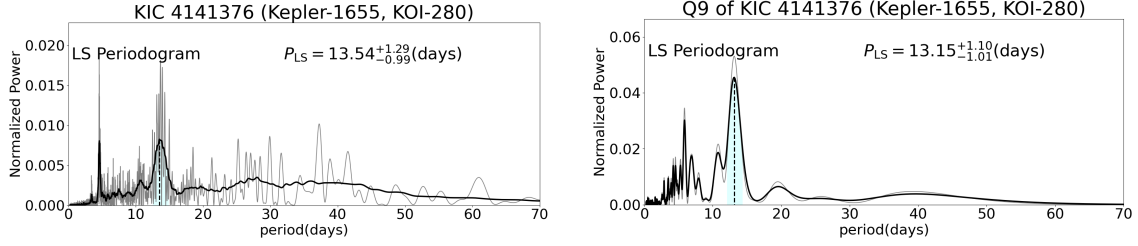


Figure 25. An example of the LS periodogram for *Kepler*-1655 (KIC 4141376, KOI-280). Left: LS periodogram computed from entire light curve. Right: periodogram computed from Q9. The thick black line indicates the boxcar-smoothed result (over $0.1 \mu\text{Hz}$) of the original LS periodogram (thin gray curves). The vertical blue dashed line indicates the location of P_{LS} , and the associated blue shaded area corresponds to HWHM in both sides.

$P_{\text{LS},q}$ for different q and the comparison against P_{LS} are useful in examining both the reliability of the measurements and the degree of the latitudinal differential rotation due to the non-static nature of starspots.

We note here a fairly common problem in selecting the the highest peak in the LS periodogram as the stellar rotation period P_{LS} . Figure 25, for example, shows another significant peak around 4 days, and it could correspond to a true rotation period, a higher harmonic, or a false positive due to stellar surface activity, instrumental noise, and/or contamination from possible companions (e.g. Reinhold & Reiners 2013; Santos et al. 2017; Chowdhury et al. 2018). It could also come from the symmetric distribution of starspots (Suto et al. 2022). Hence, we examine the reliability of the highest peak in the LS periodogram by repeating the analysis in individual quarters and also through the close comparison against other complementary methods, in particular a time-localized spectrum-wavelet power spectrum.

A.1.2. Autocorrelation function

We compute auto-correlation function (see e.g. McQuillan et al. 2013; McQuillan et al. 2014) of the light curve $L(t)$:

$$A(\tau) = \frac{\int_0^{T_0/2} dt L(t) L(t + \tau)}{\int_0^{T_0/2} dt L(t) L(t)}. \quad (\text{A3})$$

Then, we smooth $A(\tau)$ using the Gaussian filter of $50\delta t \approx 1\text{day}$ in order to suppress the short-term modulations unrelated to, and/or the harmonics of, the stellar rotation.

Figure 26 shows examples of the ACF analysis for *Kepler*-1655 (KIC 4141376, KOI-280). The periodic patterns in the top and middle panels are the clear signature of the stellar rotation. A substantial fraction of our current targets, however, exhibits a more complicated pattern. So we apply the generalized LS periodogram to the smoothed ACF, and extract the embedded period. Following the procedure described in §A.1.1, we define the stellar rotation period P_{ACF} and the associated uncertainties from the ACF method.

A.1.3. Wavelet

Wavelet analysis (WA) is one of the widely applied methods that identify time-dependent signals in a time-frequency domain. Since the photometric variations in the stellar light curves are time-dependent over the observed duration (T_0) reflecting the dynamical nature of spots on the stellar

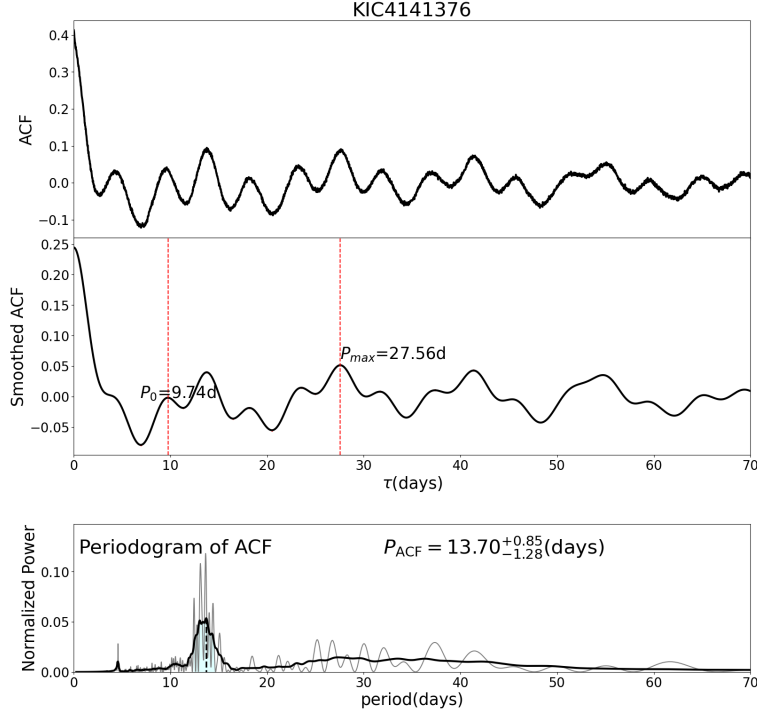


Figure 26. Examples of ACF analysis for KIC 4141376 (KOI-280, *Kepler*-1655). Top, middle and bottom panels show ACF, smoothed ACF, and LS periodogram of the smoothed ACF. In the middle panel, P_0 is the period associated with the first maximum and P_{max} is the one associated with the highest maximum.

surface, WA is naturally suited for the detection of the underlying stellar rotation period including the possible effect of the differential rotation.

Following [Torrence & Compo \(1998\)](#); [García et al. \(2014\)](#), we adopt the Morlet wavelet that corresponds to a sinusoidal wave localized in the time domain using a Gaussian window of the form:

$$\psi(t; s) = \frac{1}{\pi^{1/4}} e^{i w_0 t / s} \exp\left(-\frac{t^2}{2s^2}\right), \quad (\text{A4})$$

and search for the best-fit value of the scale s . The dimensionless parameter w_0 is introduced to control the resolution in the time-domain, and we adopt the common value of $w_0 = 6$. The scale s is related to the period of the signal in the standard Fourier mode P as

$$P = \frac{4\pi}{w_0 + \sqrt{2 + w_0^2}} s, \quad (\text{A5})$$

[Torrence & Compo \(1998\)](#). In practice, we search for s in the range between 0.1 days and 65 days in a linearly equal bin of 0.1 days.

Figure 27 presents an example of WA for *Kepler*-1655 (KIC 4141376, KOI-280). The left panel shows the wavelet power spectrum (WPS), while the right panel is the corresponding global wavelet power spectrum (GWPS). GWPS is defined as the average of WPS over time axis multiplied by the variance of the time series. Note that the wavelet spectra in the present paper are plotted against P , equation (A5), instead of s . Finally, we define the WA rotation period P_{WA} from the highest peak in the GWPS, and compute the uncertainties based on its HWHM.

While the above definition of the uncertainties in GWPS turns out to be generally larger than those in LS and ACF, this may be simply due to a matter of definition, given the fact that a majority of their peak profiles is far from Gaussian nor symmetric. Thus, their quantitative interpretation and comparison against other results should be made with caution.

Instead, we would like to emphasize that WPS provides useful information on the time-dependence of the measured stellar rotation period over the entire observing time, which is likely related to the strength of the differential rotation of each star. This is the most important and complementary aspect of WA. For instance, the left panel of Figure 27 indicates that the measured rotation period is relatively stable and does not show any detectable variation, implying that the differential rotation is very weak and/or that those spots responsible for the photometric variations are static over a timescale of 1200 days.

It is also important to note that Figure 27 clearly indicates that the peak around 4 days exhibited in Figures 25 and 26 mainly come from the contribution of Q2. While it is not clear why Q2 behaves very differently from the other quarters, WA strongly indicates that the 4 day period does not correspond to the true stellar rotation period. This illustrates the complementary role of the WA relative to other methods.

A.2. Asteroseismic analysis

Asteroseismic analysis estimates the stellar rotation frequency $\delta\nu_*$ and inclination i_* by modeling the pulsation pattern of stars around a few thousands μHz (see Ledoux 1951; Tassoul 1980; Gizon & Solanki 2003; Mosser et al. 2013, e.g.).

Figure 28 shows an example of constraints on i_* and $\delta\nu_*$ for *Kepler*-1655 (KIC 4141376, KOI-280), derived from asteroseismic analysis by Kamiaka et al. (2018). Following them, we define the asteroseismic rotation period and their uncertainty as

$$P_{\text{astero}} = \frac{1}{\delta\nu_*(50\%)}, \quad (\text{A6})$$

$$(\Delta P_{\text{astero}})_+ = \frac{1}{\delta\nu_*(16\%)} - P_{\text{astero}}, \quad (\text{A7})$$

$$(\Delta P_{\text{astero}})_- = P_{\text{astero}} - \frac{1}{\delta\nu_*(84\%)}, \quad (\text{A8})$$

where $\delta\nu_*(p)$ refers to the value at the percentile p in its one-dimensional marginalized density (top-left panel in Figure 28). We emphasize that the above definitions are not necessarily unique, and that the comparison against the photometric rotation period needs to be interpreted with caution especially when $\Delta P_{\text{astero}}/P_{\text{astero}}$ is large. We adopt the asteroseismic result by Kamiaka et al. (2018) for all the target stars. Further details of their analysis may be found in Kamiaka et al. (2018), Kamiaka et al. (2019), and Suto et al. (2019).

B. COMPARISON WITH PREVIOUS PHOTOMETRIC ANALYSIS

Among our 70 targets discussed in the previous section, 44 have their photometric rotation periods published in previous literature. Left panel of Figure 29 plots the comparison of the rotation periods derived from the same photometric method. We use different colors to distinguish the four groups that we introduced in the previous section, while different symbols indicate different papers shown in the caption; P_{LS} from Nielsen et al. (2013) and Karoff et al. (2013), P_{ACF} from McQuillan et al.

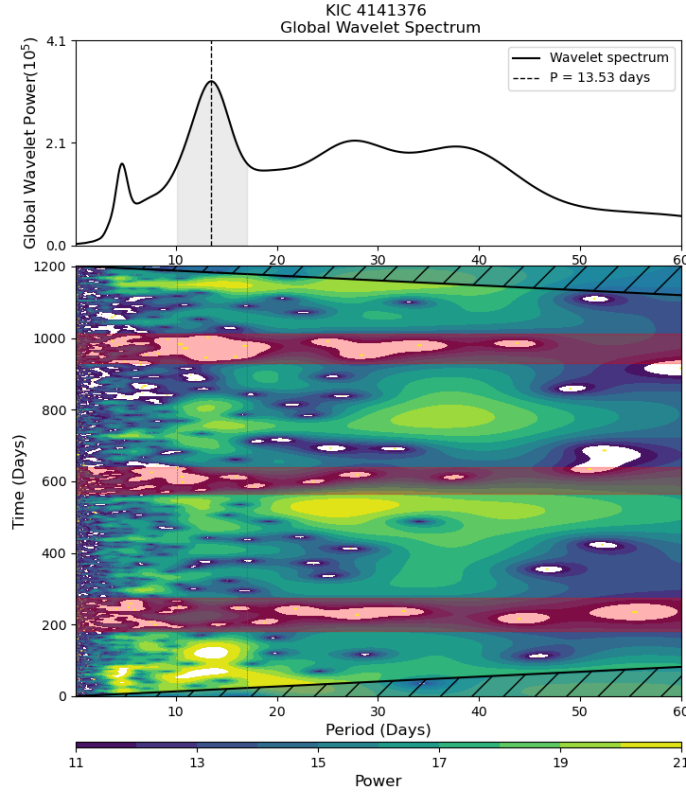


Figure 27. Wavelet power spectrum (lower panel) and global wavelet power spectrum (upper panel) of *Kepler*-1655 (KIC 4141376, KOI-280). The brighter color in wavelet power spectrum indicate a larger power. The cross-hatched region near the bottom edge of the waver power spectrum is the cone of influence within which power is less reliable. The dotted line in the right panel marks the maxima of GWPS, which corresponds to the measured period. The removed quarters are indicated in magenta. The shaded region in the upper panel covers the HWHM in both sides of the peak.

(2013) and McQuillan et al. (2014), and P_{WA} from Ceillier et al. (2016) and García et al. (2014). Right panel of Figure 29 plots the rotation periods in previous literature against our P_{LS} on which our photometric classification is based. In what follows, we present detailed discussion of the comparison against those papers individually.

B.1. *Nielsen et al. (2013)*

Nielsen et al. (2013) first conducted the LS analysis for Q2 to Q9 separately, using the *Kepler* PDC-SAP light curve (SAP is light curve without removal of systematic effect. msMAP is light curve which has been processed, e.g. removal of systematic effect). They assume that $P_{\text{LS},q}$ should be within $[1, 30]$ days and define the median of those $P_{\text{LS},q}$ as as the rotation period, P_{rot} . Among their final sample of 12151 stars, we have 7 targets in common; 5 targets belong to our category of likely binary/multiple-star systems (see Table 2) which we exclude in the comparison, and the other two stars (KIC 7206837 and 9812850) belong to our Group Aa and their rotation periods are in good agreement with our $\langle L_{\text{LS}} \rangle$.

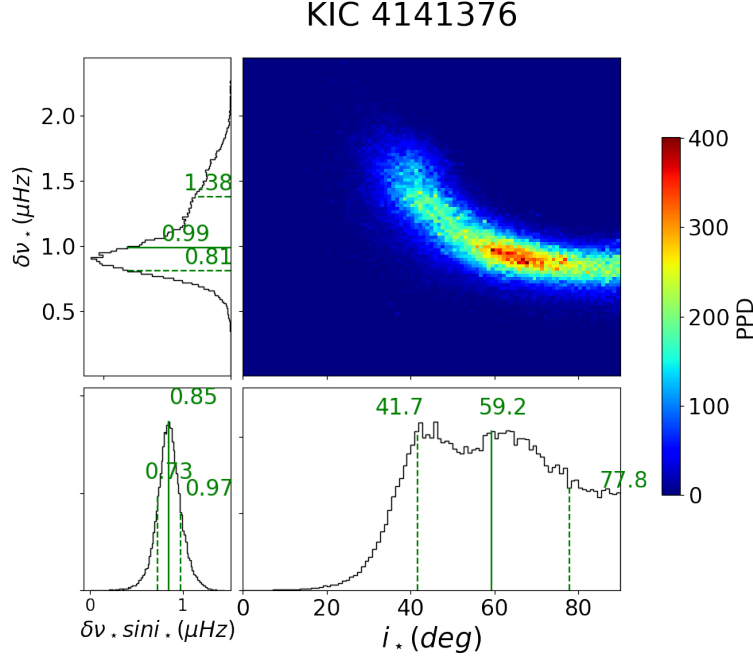


Figure 28. Posterior probability density (PPD) on the stellar inclination i_* and rotation frequency $\delta\nu_*$ for *Kepler*-1655 (KIC 4141376, KOI-280) marginalized over all other parameters. Top-left, bottom-left, and bottom-right panels plot one-dimensional marginalized densities of $\delta\nu_*$, $\delta\nu_* \sin i_*$, and i_* , respectively. Solid and dashed lines in those panels indicate the median and 16%–84% intervals for those parameters derived from asteroseismology alone.

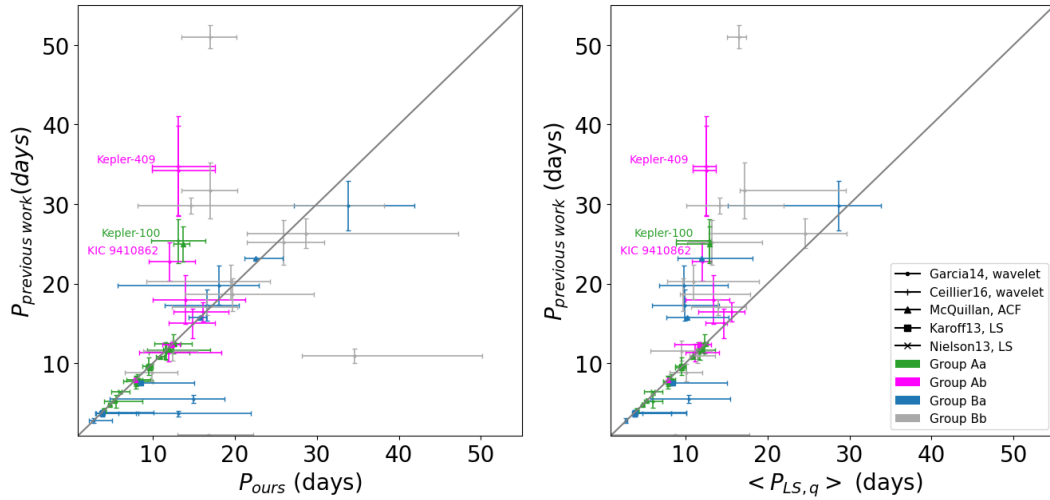


Figure 29. Comparison of the rotation periods for 44 stars overlapped in the previous literature and our sample. Left panel shows the comparison based on the same photometric method, while right panel plots their rotation periods against our P_{LS} . Different colors indicate four groups that we introduced in the previous section, while different symbols indicate different papers; P_{LS} from Nielsen et al. (2013) and Karoff et al. (2013), P_{ACF} from McQuillan et al. (2013) and McQuillan et al. (2014), and P_{WA} from Ceillier et al. (2016) and García et al. (2014).

B.2. *Karoff et al. (2013)*

Similarly, *Karoff et al. (2013)* performed a quarter-wise LS analysis for a sample of 20 stars using Q2-Q14 of *Kepler* PDC-SAP. They defined P_{rot} from the peak with S/N higher than 4 in all 14 quarters. We have 8 overlapped targets, 4 in the category of likely binary/multiple-star systems. The remaining 4 targets in Group Aa (KIC 12009504) and Group Ba (KIC 2837475, KIC 11253226, KIC 8694723) have rotation periods consistent with our results.

Incidentally, we note that KIC 11253226 is one of the 8 targets for which our LS, ACF and WA methods indicate different rotation periods (Figure 13). As we discuss in Section 5.1, when multiple peaks occur in spectra, the LS analysis tends to prefer the high frequency signal which lasts for over half of the entire observation, while ACF and WA select a lower frequency signal. Since *Karoff et al. (2013)* required the signal to exist clearly in all quarters of Q2-Q14, their value for KIC 11253226 is consistent with our estimates of $\langle P_{\text{LS},q} \rangle \approx P_{\text{astero}} \approx 4$ days, instead of $P_{\text{ACF}} \approx P_{\text{WA}} \approx 13$ days.

B.3. *McQuillan et al. (2013) and McQuillan et al. (2014)*

McQuillan et al. (2013) and *McQuillan et al. (2014)* applied ACF method on Q3-Q14 of *Kepler* PDC-MAP lightcurve. PDC-MAP is an earlier version of data release for *Kepler* PDC light curve. It differs from PDC-msMAP in that the later one conducts a stricter correction of the 30 days Earth-point recovery artifact *Stumpe et al. (2014)*. We have 20 stars in common, including 10 KOI stars and 10 non-KOI stars; ten stars belong to Group Aa, two stars to Group Ba, two stars to Group Ab, and the remaining six stars are in likely binary/multiple star systems.

Among 14 stars with no apparent stellar companion, *Kepler*-100 is the only case for which our P_{ACF} (≈ 14 days) is different from their estimate (≈ 25 days). This potentially interesting case has been carefully examined in §4.1.

B.4. *García et al. (2014)*

García et al. (2014) applied both wavelet analysis and ACF(*McQuillan et al. 2013*) method on concatenated Q0-Q14 *Kepler* light curves. When the two different methods estimate the rotation periods in agreement within 20%, they adopt the peak location of the GWPS as P_{rot} and the HWHM of the corresponding peak as its uncertainty.

We have 28 stars in common; three targets in Group Aa, eight in Group Ba, five in Group Ab, nine in Group Bb, and three in the category of possible binary/multiple star systems. Among single star systems, two stars in Group Ab (KIC 9410862 and *Kepler*-409) and three stars in Group Bb (KIC 12069127, 10644253 and 3656476) have rotation periods inconsistent with their results.

The rotation periods for KIC 9410862, *Kepler*-409, and 3656476 reported in *García et al. (2014)* are about two to three times larger than our results. We examined the GWPS spectra for these three targets, and were unable to identify significant periodic components corresponding to their values.

For KIC 9955598 (*Kepler*-409, KOI-1925), we recover a period consistent with the value of 27.25 days (*García et al. 2014*) if we include an anomalous quarter Q13 with sudden increase in photometric variation that is removed in our analysis (Figure 10). Further discussion on *Kepler*-409 is found in §4.3.

For KIC 9410862 (Figure 11) and 3656476 (Figure 15), the high-pass filter of a frequency of $1/20$ day $^{-1}$ applied to the latest PDC-SAP light curve (and PDC-msMAP) tends to suppress the signal of fundamental period for slow rotators (*Santos et al. 2019; García et al. 2014*). This may explain why our result prefers shorter periods than theirs. Our $P_{\text{astero}} \approx 10$ days for KIC 9410862 is consistent

with our photometric value, while $P_{\text{astero}} \approx 40$ days for KIC 3656476 is a factor of two larger than our photometric estimate and indeed consistent with the value of [García et al. \(2014\)](#).

As for the other two stars in Group Bb, KIC 12069127 (Figure 15) is one of the targets with multiple significant periodic components in the GWPS spectra. The low frequency peak with $P \sim 17$ days is selected by us while the high frequency peak with $P \sim 1$ day is selected by [García et al. \(2014\)](#). Despite both peaks are detected in our GWPS spectra, smoothing applied to the raw power suppress the extremely high frequency which would lead to a different selection of period. It would be important to note that a periodicity less than 1 day is close to the frequency range of stellar pulsation. In our sample, there are two targets showing significant peak at period less than 1 day (KIC 12069127 and 9139163).

KIC 10644253 is also a target with multiple periodic components, a continuous high frequency signal and a short low frequency signal. Our quarter-wise measurements prefer $\langle P_{\text{LS,q}} \rangle$ over P_{LS} , P_{ACF} and P_{WA} (Figure 15 and Table 6). Result from [García et al. \(2014\)](#) is consistent with our $\langle P_{\text{LS,q}} \rangle$ instead of P_{LS} , P_{ACF} and P_{WA} .

The rotation periods of [García et al. \(2014\)](#) for the other 20 targets are in agreement with our P_{WA} . We note here, however, that there are four targets whose values of P_{WA} disagree with our P_{LS} and/or P_{ACF} ; their P_{rot} for KIC 10068307 disagrees with our P_{LS} and P_{ACF} (Figure 15), and those for KIC 11081729, 11253226, and 6508366 agree with our P_{LS} , but disagree with our P_{ACF} (Figure 13).

B.5. *Ceillier et al. (2016)*

[Ceillier et al. \(2016\)](#) basically followed the method of [García et al. \(2014\)](#), and measured the rotation period of 11 KOI stars, all of which are included in our sample; four stars are in Group Aa, two stars are in Group Ab, three in Group Bb, and the other two stars are in likely binary/multiple star systems. There are three out of 11 stars for which their P_{rot} is different from our P_{WA} ; P_{rot} of *Kepler*-100 is around twice of our P_{WA} , and P_{rot} of *Kepler*-95, and *Kepler*-409 is around three times larger than our P_{WA} .

For *Kepler*-100 and *Kepler*-409, we confirmed that we could recover P_{WA} consistent with P_{rot} of [Ceillier et al. \(2016\)](#) if we repeat the analysis with keeping somewhat anomalous quarters; see discussion in §4.1 and 4.3, respectively. Their measured period for *Kepler*-95 (KIC 8349582, KOI-122) is longer than 50 days, which is beyond our detection limit (~ 50 days).

It is also useful to add the fact that the inconsistency for the above targets arise mainly due to the different choice of light curves; [Ceillier et al. \(2016\)](#) and [García et al. \(2014\)](#) adopt KADACS, which tends to select longer period signals than PDC-msMAP light curve that is adopted in the present paper.

C. POTENTIALLY INTERESTING TARGETS

There are several targets that are potentially interesting and deserve further studies. We show their LS periodogram for all quarters and asteroseismic constraint in this section.

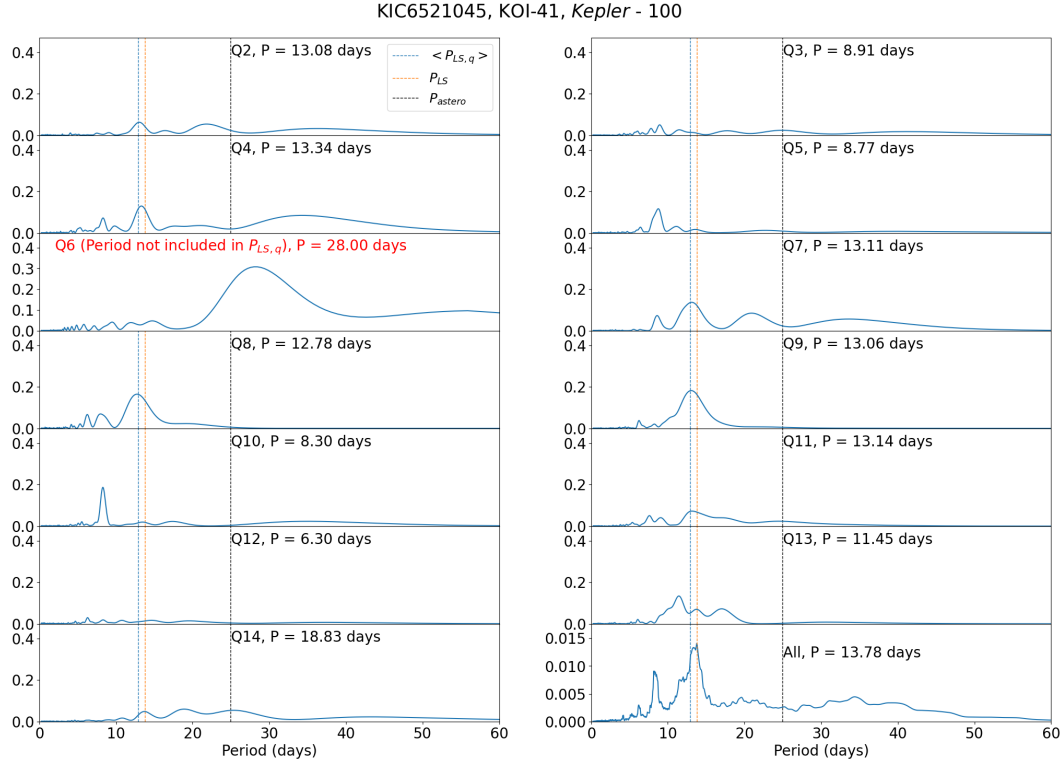
C.1. *Kepler-100* (KIC 6521045, KOI-41)

Figure 30. The LS periodograms of *Kepler-100* (Group Aa) for different quarters.

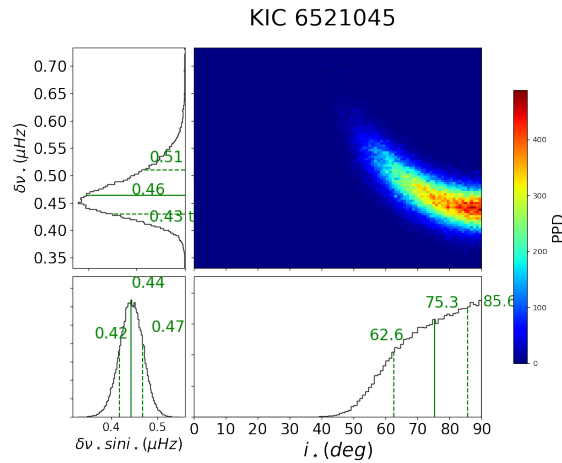


Figure 31. Asteroseismic constraints on $\delta\nu_*$ and i_* for *Kepler-100* (Group Aa).

C.2. KIC 5773345

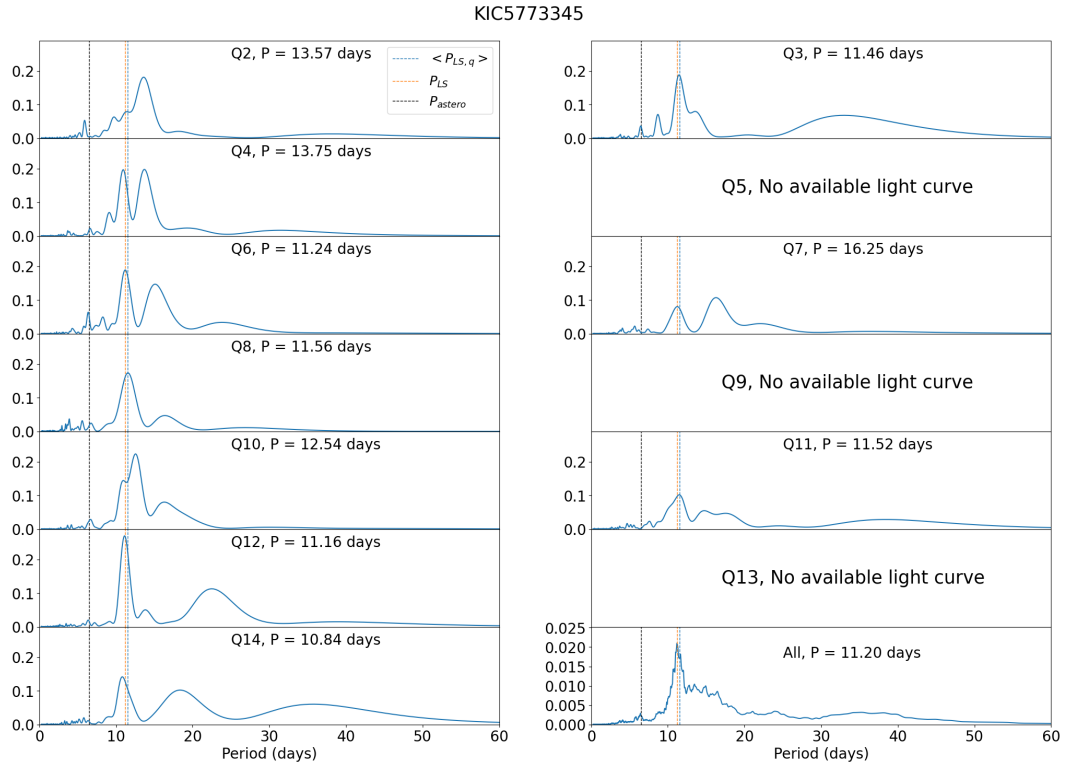


Figure 32. The LS periodograms of KIC 5773345 (Group Aa) for different quarters.

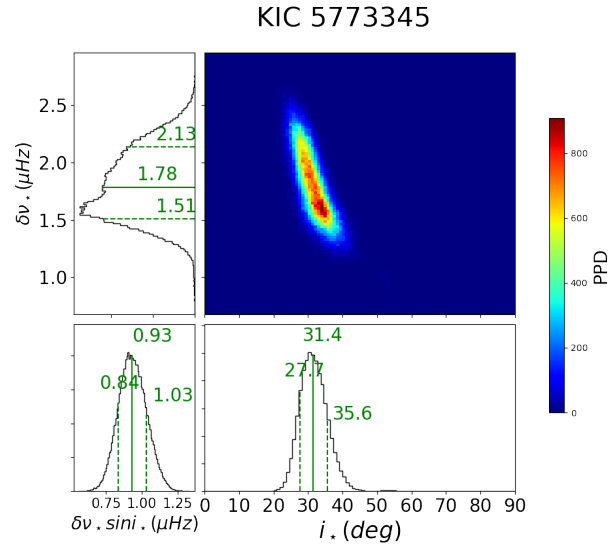


Figure 33. Asteroseismic constraints on $\delta\nu_*$ and i_* for KIC 5773345 (Group Aa).

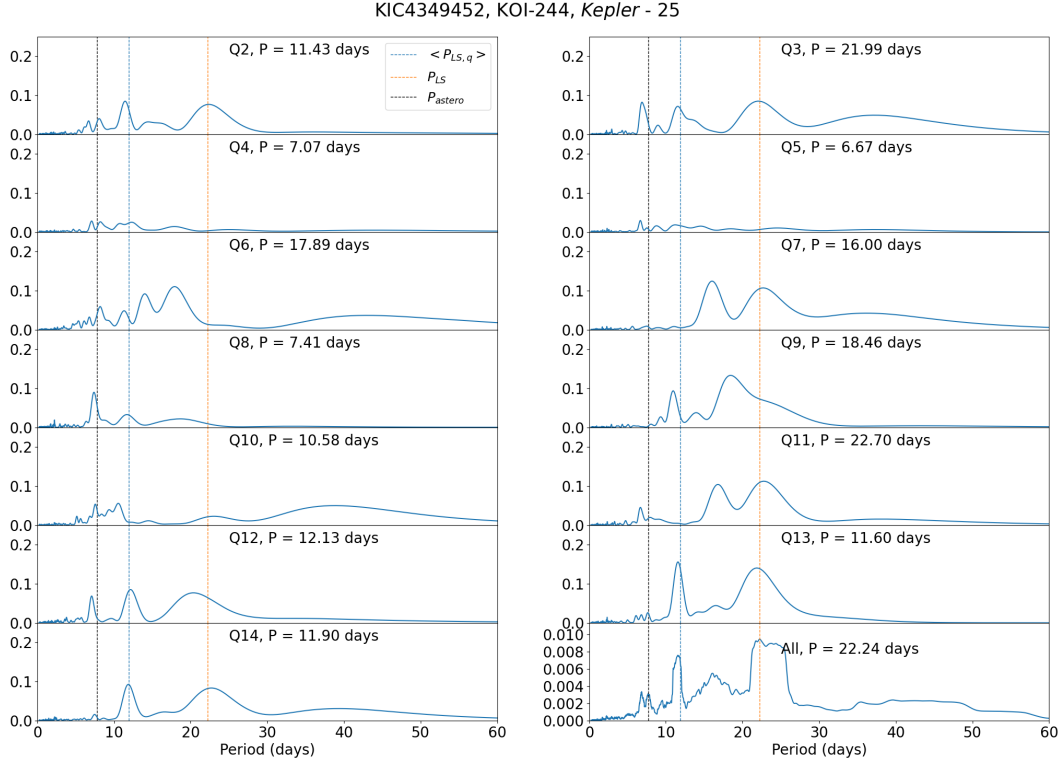
C.3. *Kepler-25* (KIC 4349452, KOI-244)

Figure 34. The LS periodograms of *Kepler*-25 (Group Ba) for different quarters.

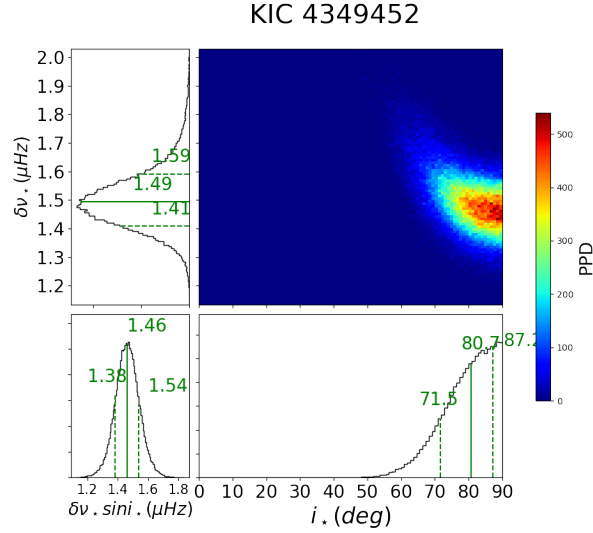
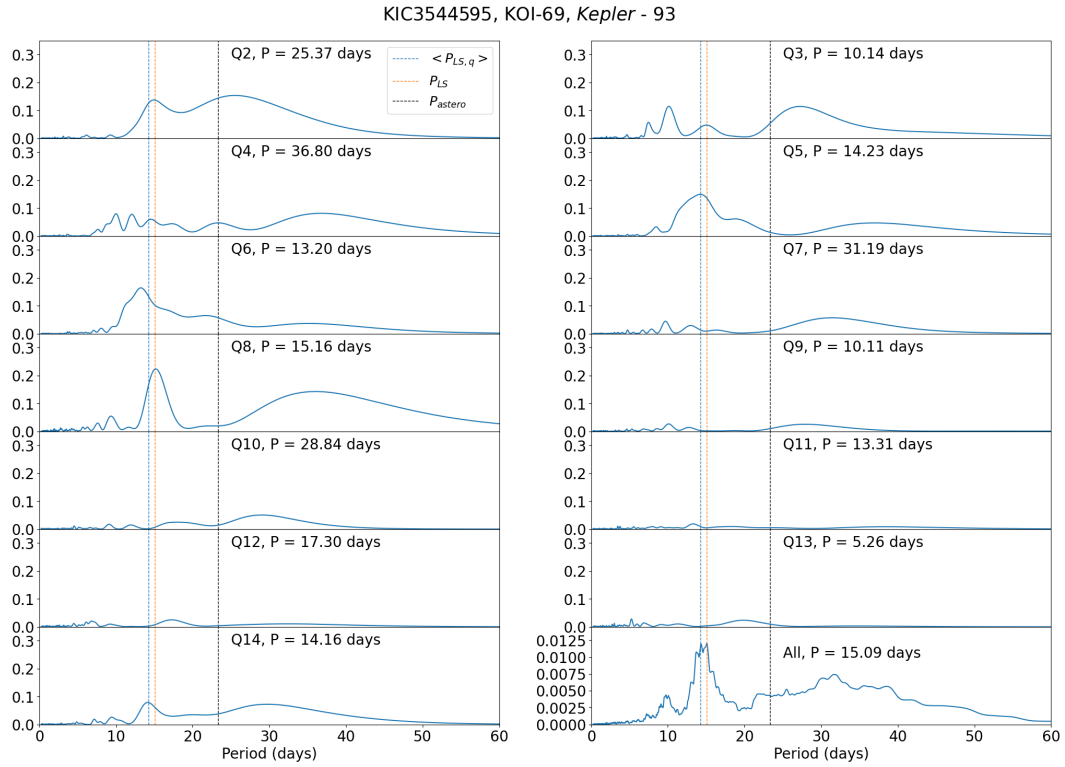
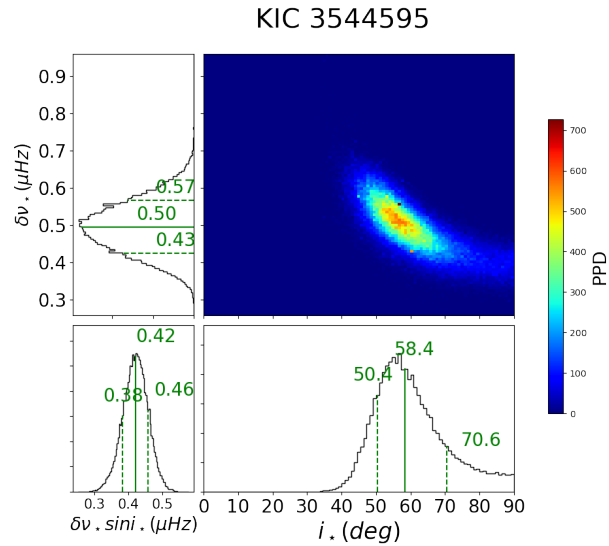


Figure 35. Asteroseismic constraints on $\delta\nu_*$ and i_* for *Kepler*-25 (Group Ba).

C.4. *Kepler-93* (KIC 3544595, KOI-69)**Figure 36.** The LS periodograms of *Kepler-93* (Group Ba) for different quarters.**Figure 37.** Asteroseismic constraints on $\delta\nu_*$ and i_* for *Kepler-93* (Group Ba).

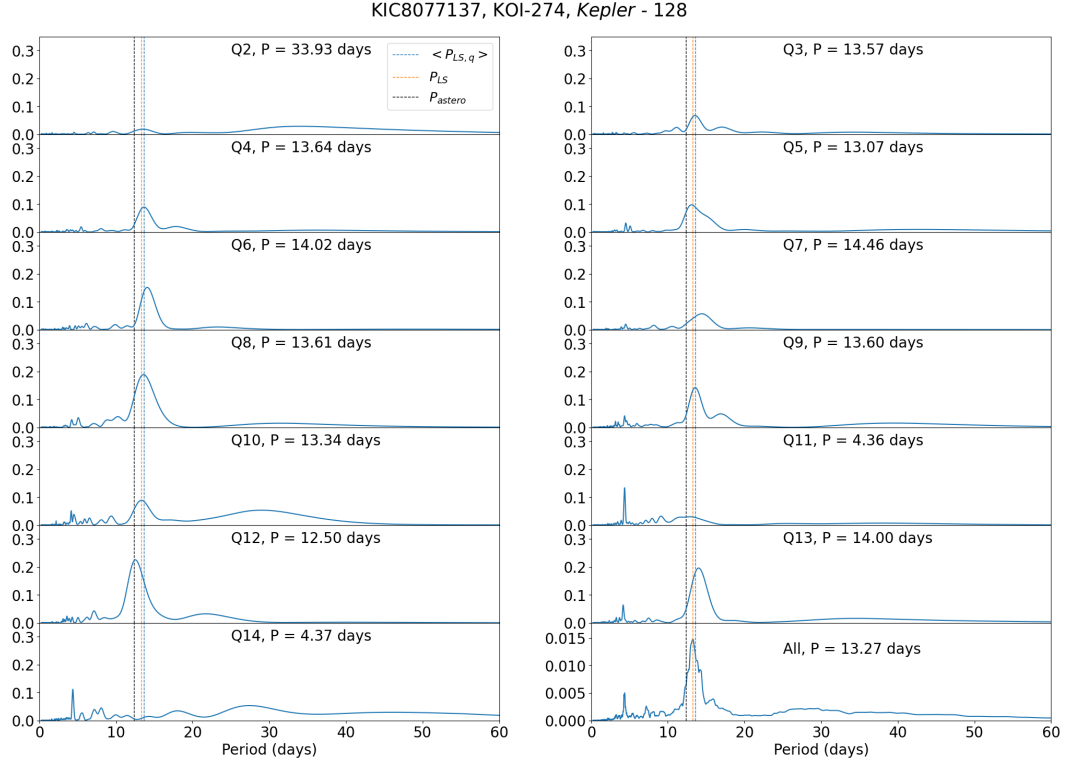
C.5. *Kepler-128 (KOI-274, KIC 8077137)*

Figure 38. The LS periodograms of *Kepler*-128 (Group Ba) for different quarters.

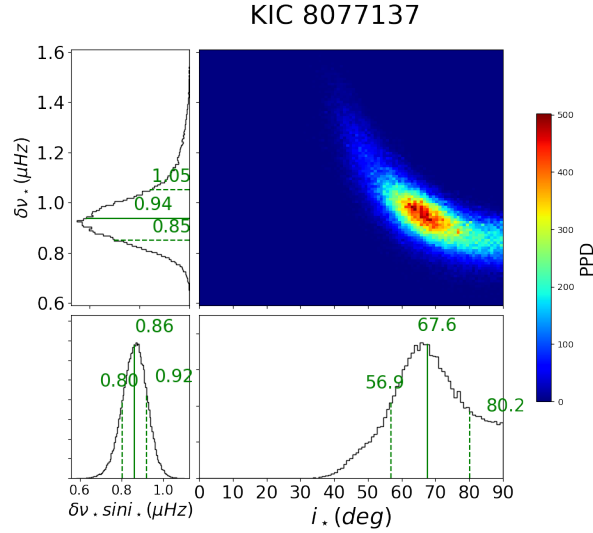
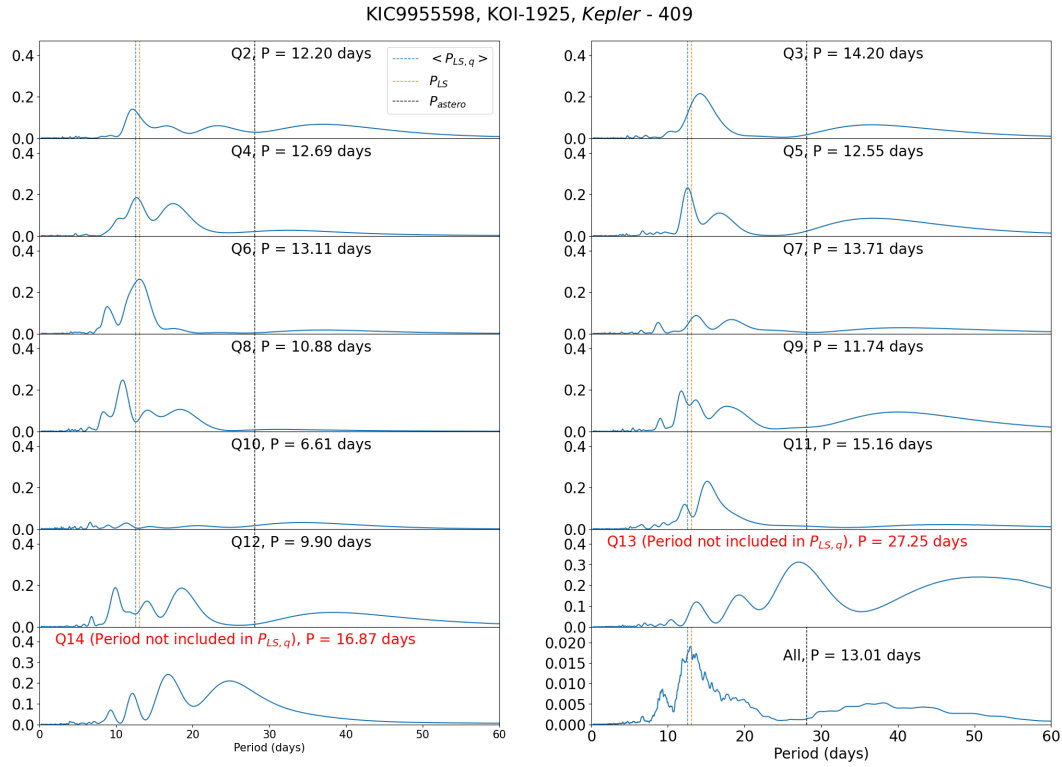
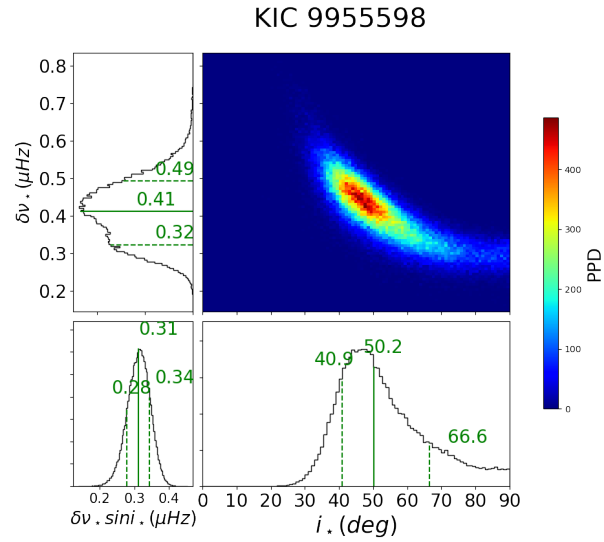


Figure 39. Asteroseismic constraints on $\delta\nu_*$ and i_* for *Kepler*-128 (Group Ba).

C.6. *Kepler-409* (KIC 9955598, KOI-1925)**Figure 40.** The LS periodograms of *Kepler-409* (Group Ab) for different quarters.**Figure 41.** Asteroseismic constraints on $\delta\nu_*$ and i_* for *Kepler-409* (Group Ab).

C.7. KIC 7970740

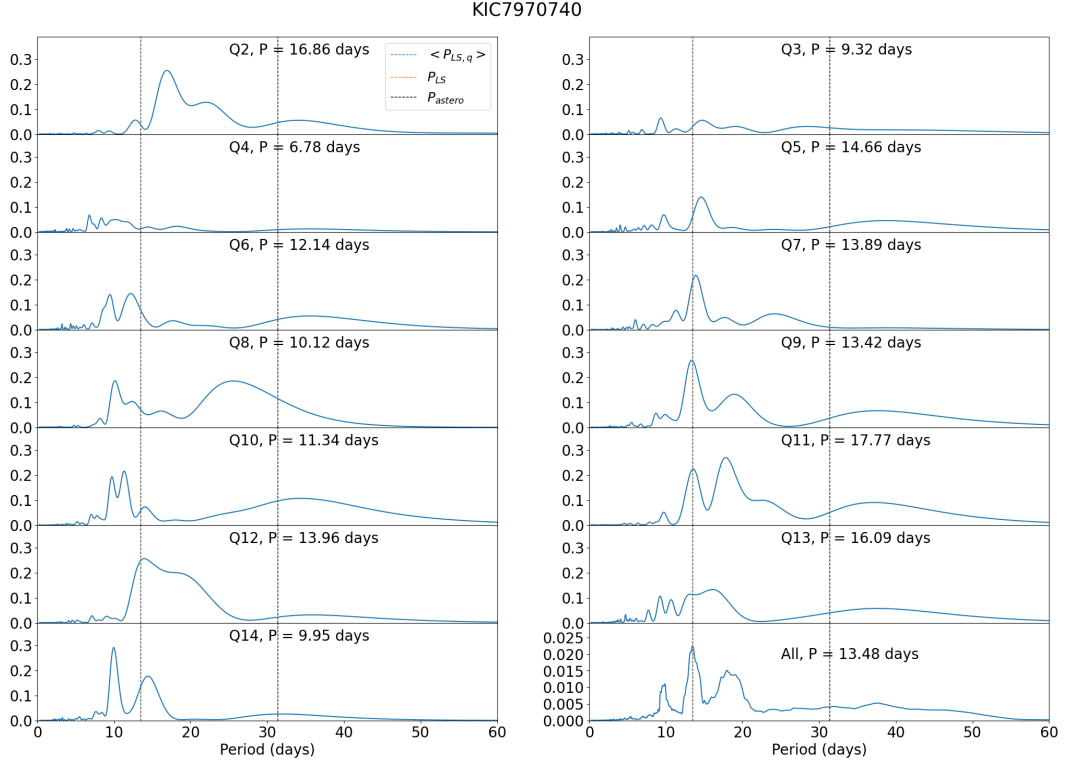


Figure 42. The LS periodograms of KIC 7970740 (Group Ab) for different quarters.

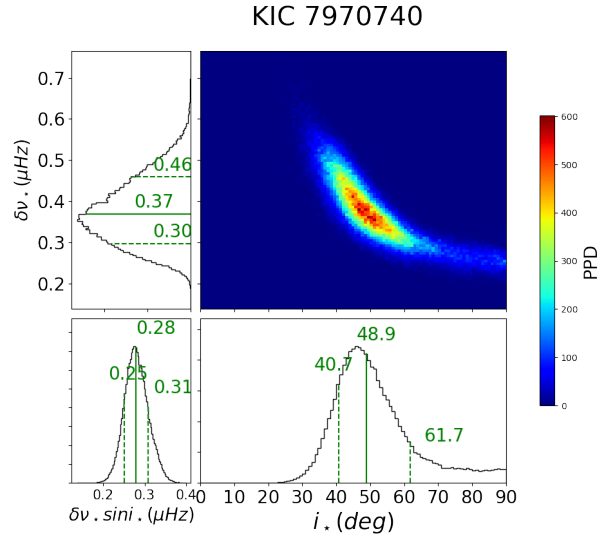


Figure 43. Asteroseismic constraints on $\delta\nu_*$ and i_* for KIC 7970740 (Group Ab).

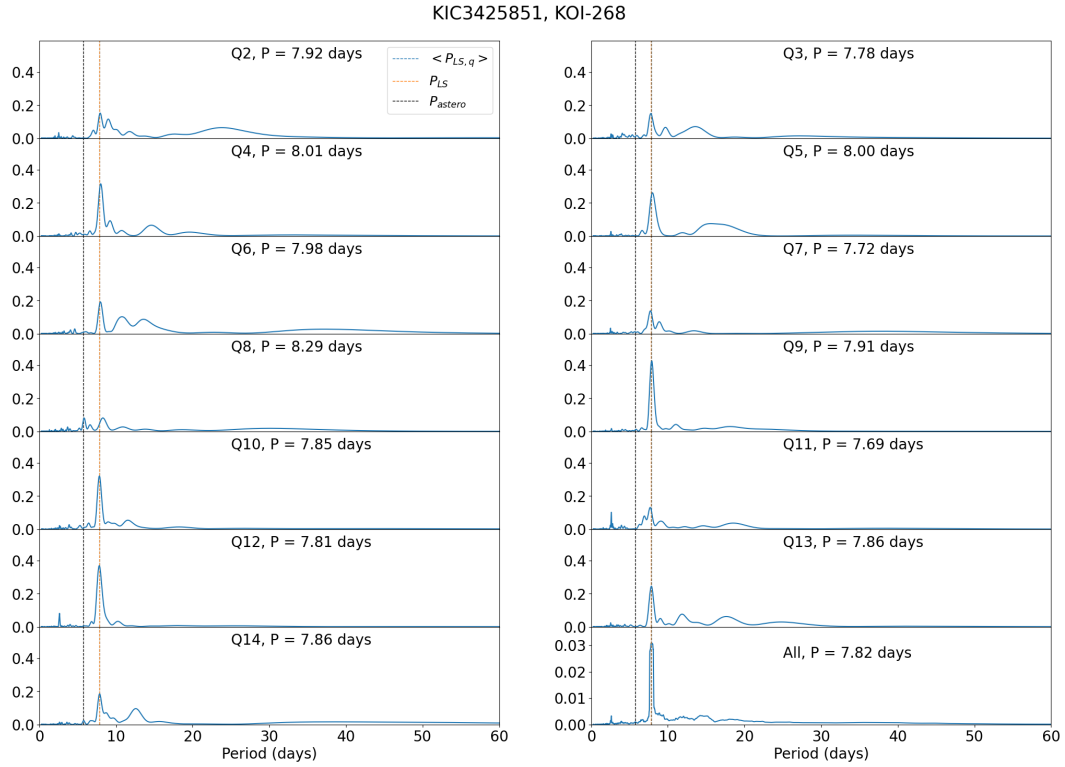
C.8. KOI-268 (*KIC 3425851*)

Figure 44. The LS periodograms of KOI-268 (Group Ab) for different quarters.

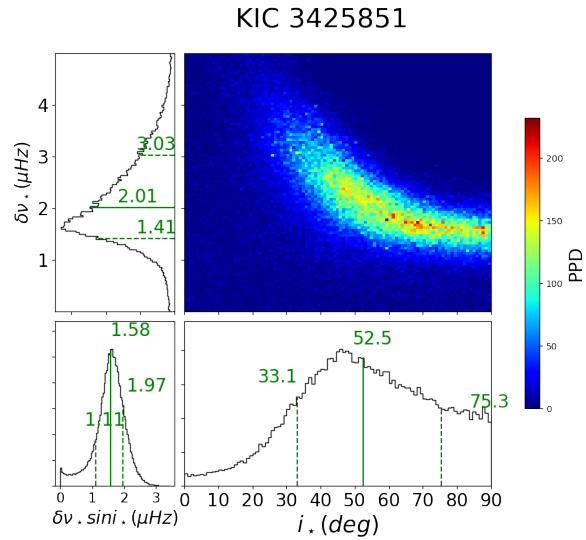


Figure 45. Asteroseismic constraints on $\delta\nu_*$ and i_* for KOI-268 (Group Ab).

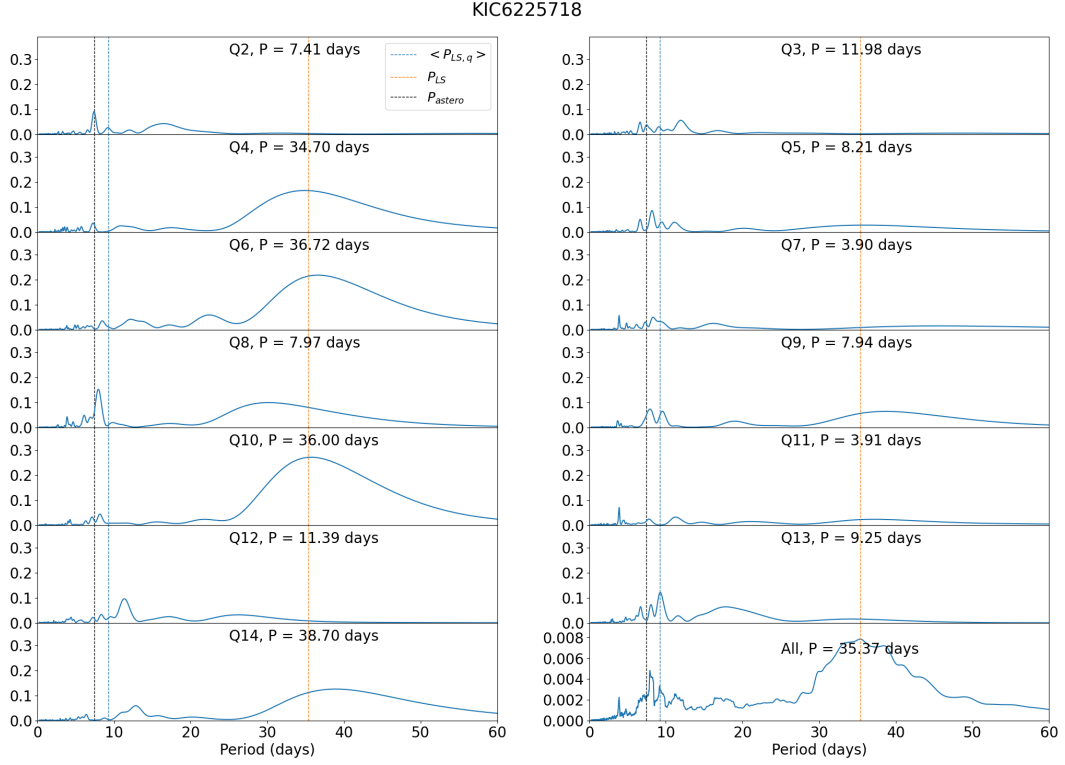
C.9. *KIC 6225718*

Figure 46. The LS periodograms of KIC 6225718 (Group Ba) for different quarters.

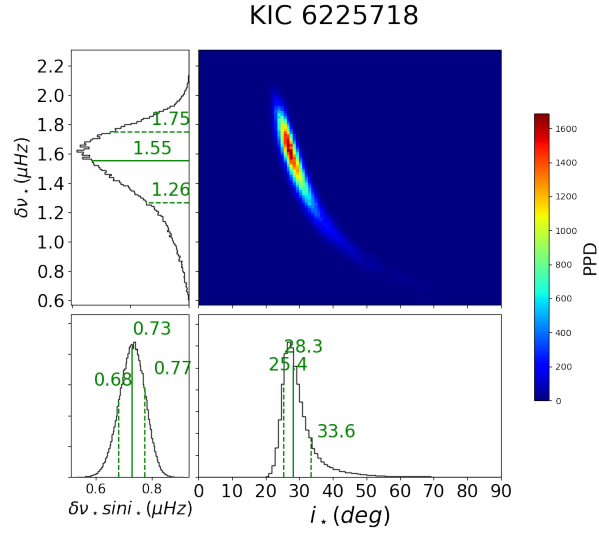


Figure 47. Asteroseismic constraints on $\delta\nu_*$ and i_* for KIC 6225718 (Group Ba).

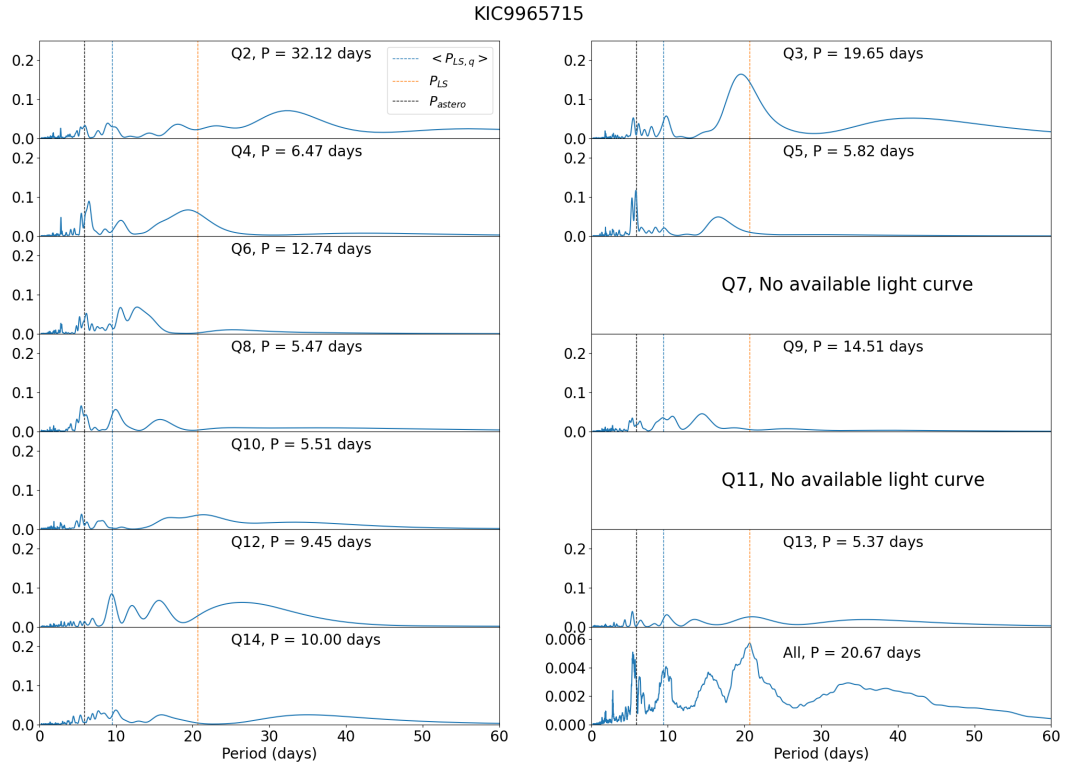
C.10. *KIC 9965715*

Figure 48. The LS periodograms of KIC 9965715 (Group Ba) for different quarters.

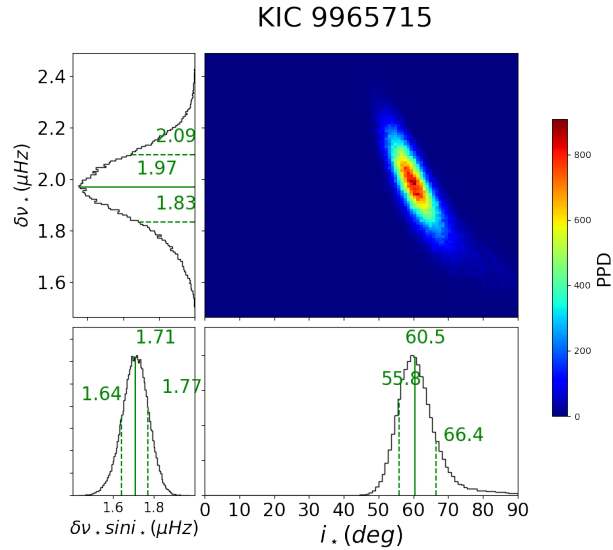
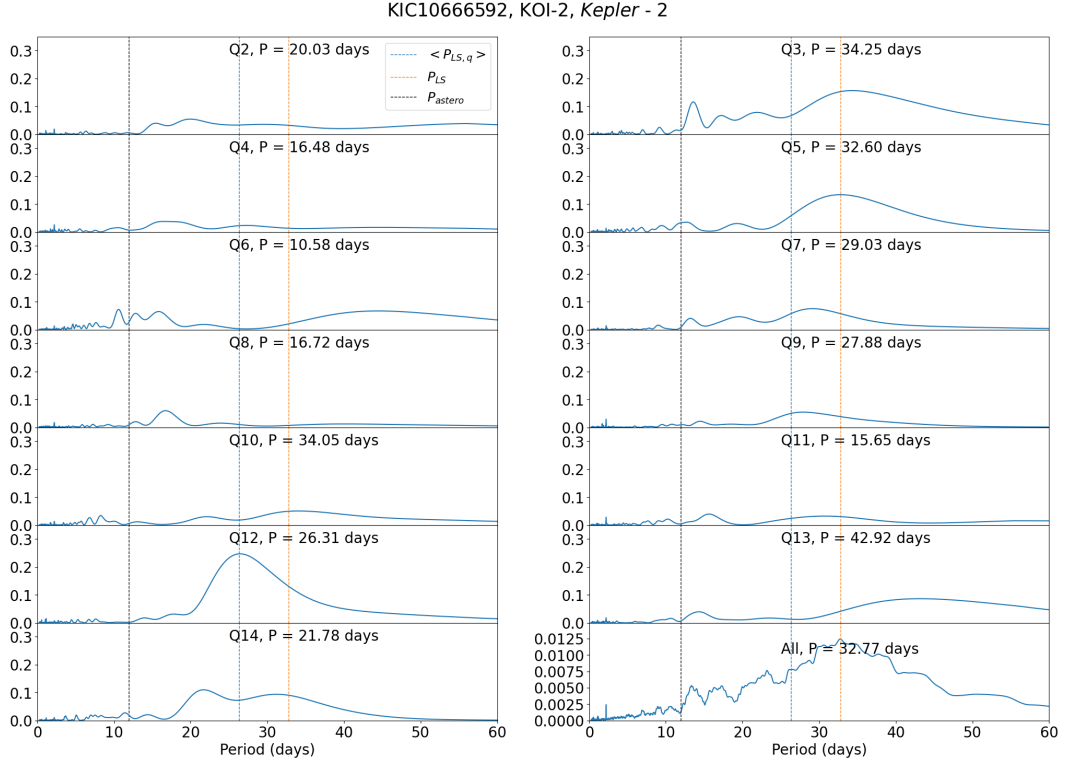
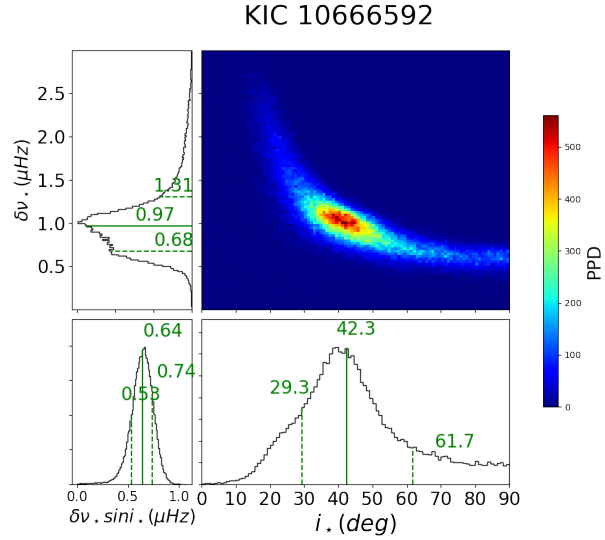
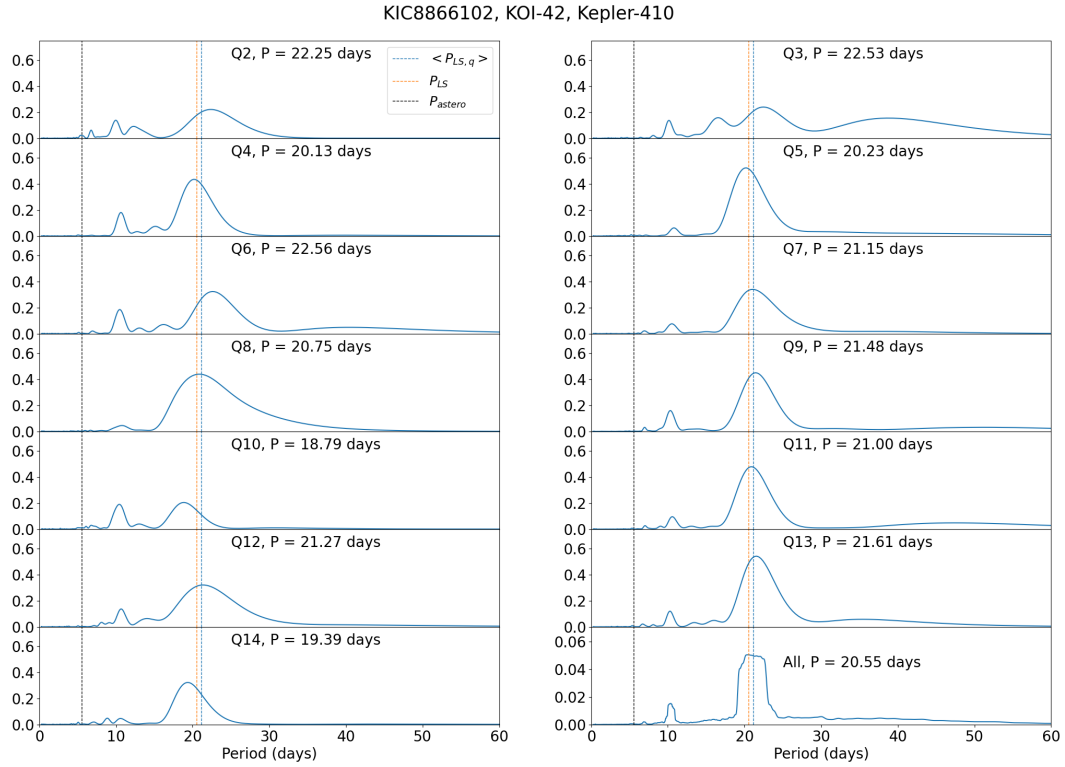
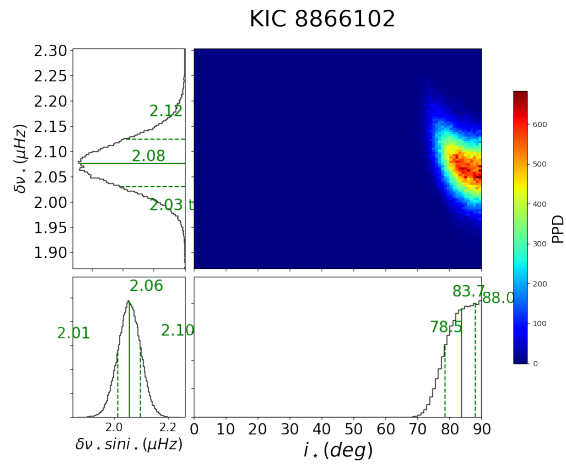


Figure 49. Asteroseismic constraints on $\delta\nu_{*}$ and i_{*} for KIC 9965715 (Group Ba).

C.11. *Kepler-2* (*HAT-P-7*, *KOI-2*, *KIC 10666592*)**Figure 50.** The LS periodograms of *Kepler-2* for different quarters.**Figure 51.** Asteroseismic constraints on $\delta\nu_*$ and i_* for *Kepler-2*.

C.12. *Kepler-410* (KOI-42, KIC 8866102)**Figure 52.** The LS periodograms of *Kepler-410* for different quarters.**Figure 53.** Asteroseismic constraints on $\delta\nu_*$ and i_* for *Kepler-410*.

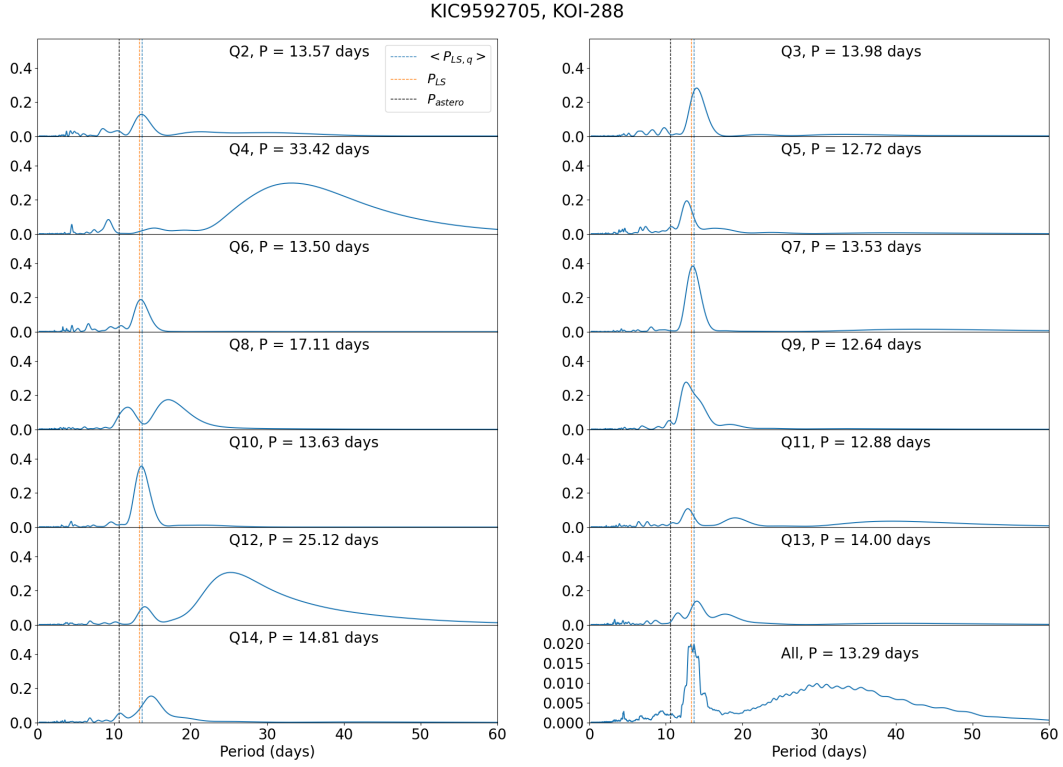
C.13. KOI-288 (*KIC 9592705*)

Figure 54. The LS periodograms of KOI-288 for different quarters.

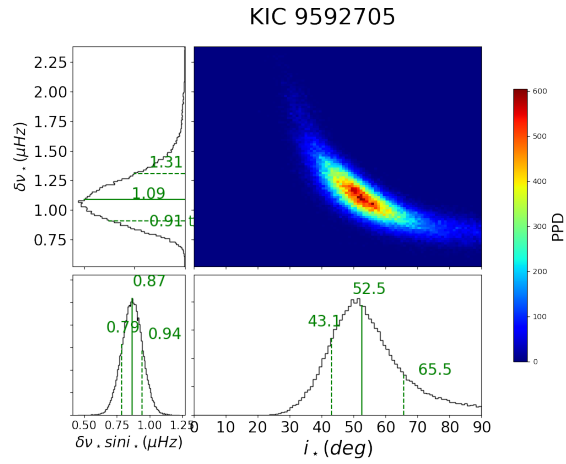


Figure 55. Asteroseismic constraints on $\delta\nu_*$ and i_* for KOI-288.

Table 2. Estimated rotation periods for 22 possible binary/multiple-star systems.

KIC	KOI ^b	<i>Kepler</i> ID	RUWE	$\langle P_{LS,q} \rangle$ (Day)	P_{LS} (Day)	P_{ACF} (Day)	$P_{wavelet}$ (Day)	P_{astero}^a (Day)	Ref.
11295426	KOI-246	<i>Kepler</i> -68	0.92	$16.07^{+4.39}_{-5.74}$	$32.90^{+12.02}_{-5.81}$	$33.26^{+11.45}_{-5.62}$	$32.85^{+13.89}_{-7.28}$	$37.33^{+15.92}_{-12.30}$	1
8866102	KOI-42	<i>Kepler</i> -410	0.97	$21.15^{+0.78}_{-0.97}$	$20.54^{+2.40}_{-1.42}$	$20.78^{+2.12}_{-1.67}$	$20.97^{+3.25}_{-3.15}$	$5.59^{+0.11}_{-0.13}$	6
10666592	KOI-2	HAT-P-7	0.98	$26.31^{+7.02}_{-9.71}$	$32.77^{+11.74}_{-7.09}$	$32.11^{+12.77}_{-6.08}$	$32.75^{+11.62}_{-11.52}$	$11.95^{+5.20}_{-3.08}$	4
6278762	KOI-3158	<i>Kepler</i> -444	1	$31.68^{+5.89}_{-5.72}$	$31.81^{+19.00}_{-5.74}$	$30.71^{+10.34}_{-4.35}$	$31.61^{+18.34}_{-7.39}$	$29.68^{+3.39}_{-6.06}$	3
3632418	KOI-975	<i>Kepler</i> -21	1.05	$12.63^{+1.09}_{-4.71}$	$12.68^{+1.07}_{-0.72}$	$12.74^{+0.63}_{-0.80}$	$12.81^{+2.53}_{-2.22}$	$12.29^{+0.75}_{-1.14}$	4
9592705	KOI-288		1.67	$13.63^{+2.33}_{-0.45}$	$13.29^{+1.18}_{-0.57}$	$13.10^{+1.33}_{-0.30}$	$13.64^{+2.53}_{-2.32}$	$10.61^{+2.11}_{-1.78}$	1
8554498	KOI-5		4.89	$17.00^{+13.72}_{-6.80}$	$13.25^{+3.99}_{-1.16}$	$35.52^{+11.28}_{-7.03}$	$35.74^{+11.21}_{-11.00}$	$24.31^{+82.77}_{-17.44}$	1
9139151			0.8	$11.82^{+1.79}_{-3.46}$	$6.30^{+0.22}_{-0.28}$	$14.08^{+0.42}_{-1.40}$	$12.09^{+7.18}_{-3.46}$	$11.59^{+0.81}_{-1.04}$	2
9139163			0.93	$6.08^{+8.21}_{-5.47}$	$5.91^{+0.24}_{-0.14}$	$16.41^{+2.76}_{-3.49}$	$15.81^{+23.09}_{-5.94}$	$3.30^{+0.44}_{-0.30}$	2
3427720			1	$13.59^{+0.53}_{-1.02}$	$13.17^{+1.51}_{-0.69}$	$13.24^{+1.45}_{-0.36}$	$13.43^{+2.63}_{-2.53}$	$25.74^{+28.39}_{-12.76}$	2
9098294			1.64	$19.20^{+1.04}_{-0.53}$	$19.31^{+2.74}_{-0.84}$	$20.12^{+1.86}_{-1.63}$	$20.14^{+3.25}_{-3.05}$	$26.57^{+7.72}_{-9.22}$	5
8179536			1.8	$5.38^{+0.27}_{-0.24}$	$5.35^{+0.20}_{-0.26}$	$13.17^{+0.23}_{-1.18}$	$5.37^{+1.29}_{-0.98}$	$6.69^{+0.75}_{-0.64}$	5
8424992			2.08	$16.73^{+10.11}_{-6.05}$	$33.78^{+11.06}_{-6.28}$	$35.21^{+9.34}_{-3.32}$	$36.05^{+9.14}_{-10.28}$	$34.44^{+70.79}_{-23.43}$	5
12317678			3.93	$9.42^{+4.56}_{-4.36}$	$13.36^{+5.05}_{-1.32}$	$13.48^{+3.49}_{-1.17}$	$14.15^{+33.42}_{-4.18}$	$10.82^{+1.58}_{-2.21}$	5
7510397			4.28	$19.53^{+12.67}_{-3.05}$	$33.50^{+12.02}_{-4.22}$	$39.63^{+5.59}_{-7.82}$	$35.23^{+12.65}_{-20.40}$	$8.37^{+3.15}_{-1.43}$	2
4914923			5.14	$10.80^{+1.95}_{-2.72}$	$7.93^{+0.46}_{-0.20}$	$7.89^{+0.39}_{-0.18}$	$14.57^{+6.35}_{-7.28}$	$19.69^{+3.57}_{-2.96}$	5
9025370			5.16	$14.55^{+8.18}_{-2.58}$	$12.35^{+3.57}_{-0.79}$	$29.80^{+8.50}_{-4.65}$	$30.89^{+8.11}_{-11.73}$	$24.53^{+3.36}_{-3.45}$	2
1435467			5.73	$7.12^{+0.91}_{-0.57}$	$7.07^{+0.52}_{-0.72}$	$6.98^{+0.23}_{-0.54}$	$6.71^{+2.74}_{-1.39}$	$7.01^{+0.86}_{-0.65}$	5
10454113			5.96	$14.56^{+0.79}_{-0.55}$	$14.55^{+1.18}_{-1.04}$	$14.33^{+0.98}_{-0.83}$	$14.67^{+2.53}_{-2.22}$	$9.89^{+3.74}_{-2.39}$	5
7871531			9.7	$16.99^{+16.78}_{-1.44}$	$34.71^{+7.68}_{-4.25}$	$35.01^{+7.49}_{-4.02}$	$35.12^{+6.25}_{-6.46}$	$28.93^{+4.85}_{-4.48}$	5
6933899			13.14	$16.25^{+0.55}_{-0.92}$	$16.18^{+1.06}_{-1.58}$	$15.93^{+0.74}_{-1.38}$	$15.81^{+3.25}_{-3.46}$	$30.84^{+3.76}_{-5.37}$	5
8379927			32.79	$17.32^{+0.71}_{-1.32}$	$17.06^{+1.71}_{-0.97}$	$17.33^{+1.39}_{-1.22}$	$17.25^{+2.63}_{-2.53}$	$10.06^{+0.41}_{-0.40}$	2

^a Data adopted from Kamiaka et al. (2018)^b KOI number only available for systems with reported planet detection.**References** (1)EB catalogue; (2)García et al. (2014) (3)Lillo-Box et al. (2014) (4)NASA Exoplanet Archive (5)RUWE (6)Eylen et al. (2014).

Table 3. Estimated rotation periods for 14 single stars in Group Aa.

KIC	KOI ^b	<i>Kepler</i> ID	$\langle P_{LS,q} \rangle$ (Day)	P_{LS} (Day)	P_{ACF} (Day)	$P_{wavelet}$ (Day)	$P_{rot, astero}^a$ (Day)	Remark
11807274	KOI-262	<i>Kepler</i> - 50	$7.82^{+0.34}_{-0.58}$	$8.09^{+0.35}_{-0.89}$	$7.95^{+0.34}_{-0.24}$	$7.95^{+2.01}_{-1.60}$	$7.60^{+0.55}_{-0.80}$	
5866724	KOI-85	<i>Kepler</i> - 65	$8.23^{+0.46}_{-0.39}$	$8.19^{+0.56}_{-0.36}$	$8.20^{+0.57}_{-0.35}$	$8.16^{+1.50}_{-1.39}$	$8.19^{+0.58}_{-0.58}$	
6521045	KOI-41	<i>Kepler</i> - 100	$12.92^{+0.20}_{-4.08}$	$13.78^{+0.76}_{-2.37}$	$13.73^{+0.75}_{-1.26}$	$13.12^{+3.25}_{-3.36}$	$24.98^{+1.96}_{-2.28}$	
8292840	KOI-260	<i>Kepler</i> - 126	$7.66^{+0.25}_{-0.70}$	$7.09^{+1.23}_{-0.35}$	$7.09^{+0.31}_{-0.27}$	$7.44^{+2.74}_{-1.70}$	$7.86^{+0.58}_{-0.61}$	
10963065	KOI-1612	<i>Kepler</i> - 408	$12.32^{+0.41}_{-0.49}$	$12.59^{+1.08}_{-0.99}$	$12.63^{+0.78}_{-1.03}$	$12.50^{+2.22}_{-2.32}$	$11.69^{+1.40}_{-0.95}$	
7670943	KOI-269		$5.25^{+0.11}_{-0.08}$	$5.35^{+0.15}_{-0.20}$	$5.30^{+0.13}_{-0.17}$	$5.27^{+0.88}_{-0.88}$	$6.08^{+0.37}_{-0.46}$	
9414417	KOI-974		$10.87^{+0.11}_{-0.07}$	$10.75^{+0.63}_{-0.39}$	$10.85^{+0.54}_{-0.48}$	$10.85^{+1.60}_{-1.50}$	$10.93^{+1.56}_{-1.75}$	
5773345			$11.54^{+2.03}_{-0.30}$	$11.20^{+0.93}_{-0.60}$	$11.24^{+0.79}_{-0.51}$	$11.57^{+5.42}_{-2.22}$	$6.49^{+1.19}_{-1.06}$	
7103006			$4.71^{+0.20}_{-0.08}$	$4.74^{+0.17}_{-0.17}$	$4.68^{+0.12}_{-0.12}$	$4.75^{+1.08}_{-0.88}$	$5.88^{+0.67}_{-0.53}$	
7206837			$4.07^{+0.03}_{-0.03}$	$4.11^{+0.01}_{-0.13}$	$4.04^{+0.08}_{-0.06}$	$4.13^{+0.57}_{-0.67}$	$4.21^{+0.48}_{-0.40}$	
7771282			$12.01^{+0.21}_{-0.44}$	$12.27^{+0.25}_{-1.01}$	$12.05^{+0.39}_{-0.82}$	$11.88^{+2.12}_{-2.01}$	$9.64^{+1.27}_{-1.38}$	
7940546			$11.72^{+0.46}_{-0.89}$	$11.63^{+1.02}_{-0.81}$	$11.61^{+1.07}_{-0.58}$	$11.67^{+2.74}_{-2.22}$	$10.70^{+1.13}_{-1.30}$	
9812850			$6.00^{+1.13}_{-1.09}$	$6.76^{+0.31}_{-0.59}$	$6.73^{+0.33}_{-0.34}$	$5.48^{+3.25}_{-1.39}$	$7.32^{+0.90}_{-1.14}$	
12009504			$9.53^{+0.49}_{-0.85}$	$9.62^{+0.72}_{-0.56}$	$9.61^{+0.33}_{-0.49}$	$9.71^{+2.22}_{-1.81}$	$9.66^{+0.60}_{-0.53}$	

^a Data adopted from Kamiaka et al. (2018)^b KOI number only available for systems with reported planet detection.^M Suggested candidate of rotation period, $\langle P_{LS,q} \rangle$ (days). Target with multiple periodic component.^A Suggested candidate of rotation period, $\langle P_{LS,q} \rangle$ (days). Target with abnormal quarter.^W Targets with weak or no periodic signals.**Table 4.** Same as Figure 3 but for 9 single stars in Group Ab.

KIC	KOI ^b	<i>Kepler</i> ID	$\langle P_{LS,q} \rangle$ (Day)	P_{LS} (Day)	P_{ACF} (Day)	$P_{wavelet}$ (Day)	$P_{rot, astero}^a$ (Day)	Remark
6196457	KOI-285	<i>Kepler</i> - 92	$15.64^{+1.54}_{-4.05}$	$16.25^{+1.88}_{-1.13}$	$16.71^{+1.08}_{-1.57}$	$16.12^{+3.15}_{-3.56}$	$5.92^{+29.78}_{-3.02}$	
8494142	KOI-370	<i>Kepler</i> - 145	$13.53^{+0.94}_{-1.71}$	$14.24^{+0.97}_{-1.49}$	$14.10^{+0.38}_{-1.31}$	$13.84^{+4.60}_{-3.87}$	$10.49^{+2.20}_{-3.82}$	
9955598	KOI-1925	<i>Kepler</i> - 409	$12.55^{+1.15}_{-1.68}$	$13.01^{+2.36}_{-1.64}$	$12.98^{+2.44}_{-1.31}$	$13.12^{+4.49}_{-3.25}$	$28.10^{+7.73}_{-4.60}$	
3425851	KOI-268		$7.86^{+0.13}_{-0.06}$	$7.82^{+0.34}_{-0.20}$	$7.87^{+0.28}_{-0.26}$	$7.95^{+1.39}_{-1.19}$	$5.76^{+2.45}_{-1.93}$	
7970740			$13.42^{+1.96}_{-3.38}$	$13.48^{+1.07}_{-0.72}$	$13.48^{+1.12}_{-0.56}$	$13.95^{+7.28}_{-3.98}$	$31.35^{+7.68}_{-6.14}$	
9353712			$11.20^{+2.89}_{-1.21}$	$10.74^{+4.75}_{-0.63}$	$14.98^{+0.39}_{-1.49}$	$11.88^{+6.46}_{-3.56}$	$6.18^{+6.66}_{-1.86}$	
9410862			$12.02^{+1.04}_{-1.22}$	$12.31^{+1.59}_{-1.73}$	$11.32^{+1.67}_{-0.76}$	$11.98^{+3.15}_{-2.53}$	$9.79^{+13.03}_{-4.08}$	
10162436			$11.67^{+1.39}_{-3.05}$	$11.92^{+2.67}_{-1.14}$	$12.30^{+1.01}_{-1.12}$	$12.29^{+6.15}_{-2.84}$	$17.27^{+6.10}_{-6.04}$	
12258514			$14.67^{+0.38}_{-2.26}$	$15.24^{+1.06}_{-1.15}$	$14.92^{+1.23}_{-0.80}$	$14.88^{+2.74}_{-2.94}$	$24.54^{+15.43}_{-10.35}$	

Table 5. Same as Figure 3 but for 19 single stars in Group Ba.

KIC	KOI ^b	<i>Kepler</i> ID	$\langle P_{LS,q} \rangle$ (Day)	P_{LS} (Day)	P_{ACF} (Day)	$P_{wavelet}$ (Day)	$P_{rot, astero}^a$ (Day)	Remark
4349452	KOI-244	<i>Kepler</i> - 25	11.90 ^{+6.27} _{-2.91}	22.24 ^{+3.63} _{-1.22}	22.49 ^{+3.36} _{-1.36}	22.93 ^{+4.18} _{-12.34}	7.75 ^{+0.46} _{-0.48}	
3544595	KOI-69	<i>Kepler</i> - 93	14.23 ^{+12.87} _{-2.56}	15.09 ^{+1.13} _{-1.74}	14.39 ^{+1.10} _{-0.90}	14.57 ^{+3.87} _{-2.94}	23.33 ^{+3.86} _{-2.92}	
8077137	KOI-274	<i>Kepler</i> - 128	13.60 ^{+0.40} _{-0.82}	13.27 ^{+1.18} _{-0.81}	13.29 ^{+1.14} _{-0.49}	13.43 ^{+2.63} _{-2.43}	12.34 ^{+1.28} _{-1.32}	
2837475			3.72 ^{+4.47} _{-0.06}	3.68 ^{+0.07} _{-0.05}	3.66 ^{+0.08} _{-0.04}	3.82 ^{+2.01} _{-0.88}	3.83 ^{+0.18} _{-0.14}	
5184732			9.75 ^{+5.43} _{-3.02}	6.70 ^{+0.31} _{-0.32}	6.70 ^{+0.21} _{-0.35}	18.08 ^{+4.80} _{-12.34}	20.27 ^{+1.32} _{-2.05}	
6106415			22.85 ^{+10.53} _{-6.95}	28.39 ^{+21.37} _{-13.60}	15.70 ^{+1.49} _{-0.97}	28.20 ^{+21.23} _{-15.65}	16.35 ^{+0.71} _{-0.96}	
6116048			9.91 ^{+4.19} _{-3.99}	16.81 ^{+2.26} _{-1.55}	16.80 ^{+2.34} _{-1.31}	16.63 ^{+3.87} _{-5.22}	17.93 ^{+0.98} _{-1.42}	
6225718			9.25 ^{+26.10} _{-1.58}	35.37 ^{+8.65} _{-5.88}	35.52 ^{+5.95} _{-6.27}	35.23 ^{+7.90} _{-6.87}	7.46 ^{+1.69} _{-0.85}	9.25 ± 2.73 ^M
6508366			3.89 ^{+0.84} _{-0.37}	3.75 ^{+0.19} _{-0.10}	6.84 ^{+0.37} _{-0.08}	3.82 ^{+4.08} _{-0.77}	5.28 ^{+0.18} _{-0.17}	
6679371			10.39 ^{+3.07} _{-4.69}	5.80 ^{+0.05} _{-0.25}	5.71 ^{+0.11} _{-0.17}	14.98 ^{+3.77} _{-10.28}	6.21 ^{+0.29} _{-0.34}	
8006161			28.70 ^{+5.10} _{-13.56}	33.04 ^{+9.43} _{-4.22}	32.37 ^{+9.69} _{-2.83}	33.78 ^{+8.11} _{-6.56}	21.51 ^{+3.88} _{-3.38}	
8394589			11.71 ^{+0.27} _{-0.66}	11.50 ^{+1.22} _{-0.93}	11.53 ^{+0.87} _{-0.38}	11.67 ^{+5.42} _{-3.15}	10.95 ^{+0.60} _{-0.56}	
8694723			8.48 ^{+6.55} _{-0.71}	7.86 ^{+0.16} _{-0.41}	7.83 ^{+0.14} _{-0.40}	7.95 ^{+1.11} _{-1.81}	9.18 ^{+1.30} _{-1.29}	
9965715			9.45 ^{+5.06} _{-3.94}	20.67 ^{+2.35} _{-2.40}	20.39 ^{+1.35} _{-2.29}	20.14 ^{+5.73} _{-6.97}	5.88 ^{+0.44} _{-0.35}	10.00 ± 4.19 ^M
10079226			10.20 ^{+5.01} _{-2.57}	14.87 ^{+1.89} _{-0.50}	15.74 ^{+0.77} _{-1.35}	15.29 ^{+2.94} _{-3.36}	15.35 ^{+2.47} _{-2.94}	
10516096			11.04 ^{+2.11} _{-3.93}	6.90 ^{+0.34} _{-0.35}	6.75 ^{+0.37} _{-0.20}	19.21 ^{+4.91} _{-13.07}	23.44 ^{+2.16} _{-3.53}	
11081729			2.73 ^{+0.14} _{-0.04}	2.70 ^{+0.04} _{-0.05}	18.14 ^{+1.12} _{-1.68}	2.79 ^{+2.22} _{-0.57}	3.40 ^{+0.19} _{-0.10}	
11253226			3.82 ^{+6.30} _{-0.08}	3.80 ^{+0.04} _{-0.09}	13.32 ^{+0.28} _{-1.21}	13.12 ^{+8.83} _{-10.18}	3.56 ^{+0.16} _{-0.15}	
11772920			15.99 ^{+1.39} _{-6.39}	16.09 ^{+1.68} _{-1.67}	15.72 ^{+2.01} _{-0.58}	16.43 ^{+23.71} _{-4.49}	34.72 ^{+5.47} _{-6.70}	

Table 6. Same as Figure 3 but for 28 single stars in Group Bb.

KIC	KOI ^b	<i>Kepler</i> ID	$\langle P_{LS,q} \rangle$ (Day)	P_{LS} (Day)	P_{ACF} (Day)	$P_{wavelet}$ (Day)	$P_{rot, astero}^a$ (Day)	Remark
11853905	KOI-7	<i>Kepler</i> - 4	19.53 ^{+13.86} _{-4.37}	35.68 ^{+9.07} _{-16.05}	36.28 ^{+9.46} _{-6.37}	34.09 ^{+9.97} _{-14.31}	28.16 ^{+23.45} _{-15.88}	
11904151	KOI-72	<i>Kepler</i> - 10	16.46 ^{+8.09} _{-2.76}	15.40 ^{+4.22} _{-2.36}	14.20 ^{+2.68} _{-0.63}	15.60 ^{+5.22} _{-3.56}	33.53 ^{+31.84} _{-19.20}	
11401755	KOI-277	<i>Kepler</i> - 36	14.02 ^{+3.35} _{-3.35}	16.82 ^{+2.14} _{-1.10}	17.06 ^{+1.32} _{-1.25}	16.63 ^{+3.67} _{-4.29}	17.60 ^{+3.75} _{-3.92}	
8478994	KOI-245	<i>Kepler</i> - 37	14.36 ^{+9.38} _{-1.77}	32.81 ^{+9.88} _{-6.31}	33.64 ^{+9.79} _{-2.96}	33.78 ^{+8.21} _{-9.25}	15.93 ^{+9.80} _{-6.06}	14.40 ± 2.12 ^M
8349582	KOI-122	<i>Kepler</i> - 95	16.49 ^{+0.90} _{-2.48}	16.97 ^{+1.64} _{-1.02}	17.36 ^{+1.16} _{-0.42}	16.94 ^{+44.77} _{-3.46}	40.18 ^{+19.59} _{-15.59}	
4914423	KOI-108	<i>Kepler</i> - 103	16.48 ^{+3.41} _{-7.39}	19.39 ^{+4.69} _{-3.44}	21.72 ^{+2.13} _{-3.14}	19.42 ^{+5.94} _{-10.59}	18.03 ^{+13.47} _{-10.08}	
5094751	KOI-123	<i>Kepler</i> - 109	13.48 ^{+2.54} _{-7.78}	7.29 ^{+0.36} _{-0.25}	16.50 ^{+0.85} _{-3.10}	15.08 ^{+6.46} _{-8.52}	17.92 ^{+50.67} _{-12.49}	13.58 ± 2.08 ^M
10586004	KOI-275	<i>Kepler</i> - 129	14.16 ^{+7.78} _{-4.11}	10.10 ^{+0.42} _{-0.62}	10.15 ^{+0.19} _{-0.72}	14.67 ^{+23.50} _{-6.56}	16.05 ^{+12.92} _{-5.80}	
11133306	KOI-276	<i>Kepler</i> - 509	16.53 ^{+1.76} _{-2.10}	15.75 ^{+2.59} _{-2.28}	15.85 ^{+2.15} _{-2.57}	15.70 ^{+5.42} _{-3.46}	17.95 ^{+28.71} _{-10.48}	
4143755	KOI-281	<i>Kepler</i> - 510	16.94 ^{+5.03} _{-4.79}	15.18 ^{+12.04} _{-2.17}	15.26 ^{+2.08} _{-2.27}	15.70 ^{+19.89} _{-20.75}	33.21 ^{+62.62} _{-20.75}	
4141376	KOI-280	<i>Kepler</i> - 1655	13.61 ^{+12.22} _{-6.62}	13.54 ^{+1.29} _{-0.99}	13.70 ^{+0.85} _{-1.28}	13.53 ^{+3.46} _{-3.36}	11.74 ^{+2.53} _{-3.35}	
7296438	KOI-364		13.17 ^{+6.19} _{-2.95}	26.42 ^{+3.03} _{-3.49}	25.83 ^{+3.22} _{-3.31}	25.93 ^{+5.01} _{-4.49}	22.00 ^{+43.25} _{-11.74}	13.17 ± 4.39 ^A
3456181			8.76 ^{+7.72} _{-4.38}	18.30 ^{+3.31} _{-3.57}	11.57 ^{+0.77} _{-0.46}	27.69 ^{+7.90} _{-16.99}	11.51 ^{+3.57} _{-3.95}	
3656476			17.24 ^{+12.26} _{-0.66}	16.91 ^{+2.12} _{-1.37}	17.09 ^{+2.37} _{-0.55}	16.94 ^{+3.36} _{-3.46}	36.64 ^{+10.72} _{-9.34}	
3735871			9.51 ^{+3.66} _{-3.85}	12.77 ^{+1.21} _{-1.93}	13.04 ^{+0.87} _{-0.83}	12.40 ^{+3.05} _{-3.56}	15.96 ^{+2.39} _{-4.21}	
5950854			20.99 ^{+11.19} _{-6.23}	31.44 ^{+16.83} _{-10.91}	36.50 ^{+14.91} _{-17.77}	30.78 ^{+16.06} _{-11.73}	9.76 ^{+96.92} _{-4.85}	
6603624			13.85 ^{+13.89} _{-3.28}	19.22 ^{+3.26} _{-4.18}	33.54 ^{+6.02} _{-5.38}	32.95 ^{+9.76} _{-6.87}	34.86 ^{+258.42} _{-26.93}	
7106245			10.53 ^{+8.99} _{-0.99}	36.89 ^{+15.82} _{-11.88}	12.85 ^{+0.49} _{-0.92}	35.33 ^{+16.79} _{-26.39}	19.69 ^{+19.14} _{-11.26}	10.53 ± 3.58 ^A
7680114			24.62 ^{+5.07} _{-11.84}	30.87 ^{+13.31} _{-6.37}	30.02 ^{+15.54} _{-5.49}	28.62 ^{+18.65} _{-7.18}	19.37 ^{+22.09} _{-7.08}	
8150065			10.73 ^{+4.58} _{-1.17}	45.39 ^{+12.81} _{-7.90}	45.30 ^{+12.82} _{-7.72}	45.76 ^{+10.59} _{-8.63}	22.24 ^{+39.49} _{-13.95}	10.73 ± 1.25 ^A
8228742			10.96 ^{+7.94} _{-3.21}	19.90 ^{+2.83} _{-2.02}	19.22 ^{+2.36} _{-2.36}	19.52 ^{+4.80} _{-10.28}	13.88 ^{+6.35} _{-2.46}	
8760414			16.00 ^{+21.16} _{-3.46}	34.91 ^{+9.19} _{-3.49}	34.91 ^{+9.31} _{-3.10}	36.57 ^{+8.87} _{-6.56}	22.58 ^{+112.30} _{-15.98}	
8938364			12.89 ^{+4.27} _{-3.62}	16.58 ^{+1.52} _{-3.62}	16.52 ^{+0.80} _{-1.61}	15.60 ^{+4.49} _{-4.29}	45.61 ^{+52.07} _{-28.32}	
9206432			10.12 ^{+1.92} _{-2.05}	9.96 ^{+0.68} _{-0.40}	9.94 ^{+0.77} _{-0.36}	9.92 ^{+3.05} _{-2.53}	6.56 ^{+3.91} _{-2.42}	
10068307			9.72 ^{+8.18} _{-0.41}	9.35 ^{+0.57} _{-0.39}	9.33 ^{+0.65} _{-0.15}	19.73 ^{+9.87} _{-5.84}	14.88 ^{+4.67} _{-2.89}	
10644253			11.46 ^{+2.13} _{-0.98}	33.31 ^{+11.45} _{-3.68}	34.02 ^{+8.63} _{-4.33}	34.61 ^{+15.55} _{-6.46}	31.29 ^{+85.88} _{-22.90}	11.46 ± 0.72 ^M
10730618			8.67 ^{+1.44} _{-0.50}	8.90 ^{+0.60} _{-0.77}	9.24 ^{+0.18} _{-1.12}	8.57 ^{+2.53} _{-2.53}	8.46 ^{+1.43} _{-1.13}	
12069127			8.71 ^{+9.10} _{-7.77}	17.38 ^{+1.61} _{-3.15}	17.36 ^{+1.42} _{-1.60}	16.84 ^{+5.42} _{-3.87}	17.27 ^{+13.21} _{-7.43}	

REFERENCES

- Aguirre, V. S., Lund, M. N., Antia, H. M., et al. 2017, *The Astrophysical Journal*, 835, 173.
<https://iopscience.iop.org/article/10.3847/1538-4357/835/2/173><https://iopscience.iop.org/article/10.3847/1538-4357/835/2/173/meta>
- Aigrain, S., Llama, J., Ceillier, T., et al. 2015, *MNRAS*, 450, 3211.
<https://academic.oup.com/mnras/article-abstract/450/3/3211/1072143>
- Appourchaux, T., Michel, E., Auvergne, M., et al. 2008, *A&A*, 488, 705
- Astropy Collaboration, Robitaille, T. P., Tollerud, E. J., et al. 2013, *A&A*, 558, A33
- Astropy Collaboration, Price-Whelan, A. M., Sipőcz, B. M., et al. 2018, *AJ*, 156, 123
- Barclay, T., Rowe, J. F., Lissauer, J. J., et al. 2013, *Nature*, 494, 452.
<http://arxiv.org/abs/1301.0842>
- Benomar, O., Masuda, K., Shibahashi, H., & Suto, Y. 2014, *PASJ*, 66, 94
- Benomar, O., Bazot, M., Nielsen, M. B., et al. 2018, *Science*, 361, 1231
- Brasseur, C. E., Phillip, C., Fleming, S. W., Mullally, S. E., & White, R. L. 2019, *Astrocute: Tools for creating cutouts of TESS images*, *Astrophysics Source Code Library*, record ascl:1905.007, ascl:1905.007
- Brewer, J. M., Fischer, D. A., Valenti, J. A., & Piskunov, N. 2016, *The Astrophysical Journal Supplement Series*, 225, 32.
<https://doi.org/10.3847/0067-0049/225/2/32>
- Bruntt, H., Basu, S., Smalley, B., et al. 2012, *MNRAS*, 423, 122
- Campante, T. L., Lund, M. N., Kuszlewicz, J. S., et al. 2016, *ApJ*, 819, 85
- Ceillier, T., Van Saders, J., García, R. A., et al. 2016, *MNRAS*, 456, 119.
<http://archive.stsci.edu/kepler/koi/search.php>
- Ceillier, T., Tayar, J., Mathur, S., et al. 2017, *A&A*, 605, A111.
<https://doi.org/10.1051/0004-6361/201629884>
- Chaplin, W. J., Sanchis-Ojeda, R., Campante, T. L., et al. 2013, *ApJ*, 766, 101
- Chowdhury, S., Joshi, S., Engelbrecht, C. A., et al. 2018, *Ap&SS*, 363, 260
- Donahue, R. A., Saar, S. H., & Baliunas, S. L. 1996, *ApJ*, 466, 384
- Evans, D. F. 2018, *Research Notes of the American Astronomical Society*, 2, 20
- Eylen, V. V., Lund, M. N., Aguirre, V. S., et al. 2014, *The Astrophysical Journal*, 782, 14.
<https://doi.org/10.1088/0004-637x/782/1/14>
- Fabrizius, C., Luri, X., Arenou, F., et al. 2021, *A&A*, 649, A5.
<https://doi.org/10.1051/0004-6361/202039834>
- García, R. A., Ballot, J., García, R. A., & Ballot, J. 2019, *Living Reviews in Solar Physics*, 16, 4.
<http://irfu.cea.fr/Sap/>
- García, R. A., Ceillier, T., Mathur, S., & Salabert, D. 2013, in *Astronomical Society of the Pacific Conference Series*, Vol. 479, *Progress in Physics of the Sun and Stars: A New Era in Helio- and Asteroseismology*, ed. H. Shibahashi & A. E. Lynas-Gray, 129
- García, R. A., Ceillier, T., Salabert, D., et al. 2014, *A&A*, 572, A34
- Ginsburg, A., Sipőcz, B. M., Brasseur, C. E., et al. 2019, *AJ*, 157, 98
- Gizon, L., & Solanki, S. K. 2003, *ApJ*, 589, 1009
- Hall, O. J., Davies, G. R., van Saders, J., et al. 2021, *Nature Astronomy*, 5, 707
- Hartmann, L. W., & Noyes, R. W. 1987, *ARA&A*, 25, 271
- Hirano, T., Sanchis-Ojeda, R., Takeda, Y., et al. 2012, *ApJ*, 756, 66
- Howard, R., & Harvey, J. 1970, *SoPh*, 12, 23
- Huber, D., Chaplin, W. J., Christensen-Dalsgaard, J., et al. 2013, *ApJ*, 767, 127
- Hunter, J. D. 2007, *Computing in Science & Engineering*, 9, 90
- Kamiaka, S., Benomar, O., & Suto, Y. 2018, *Monthly Notices of the Royal Astronomical Society*, 479, 391. <https://academic.oup.com/mnras/advance-article/doi/10.1093/mnras/sty1358/5001890>
- Kamiaka, S., Benomar, O., Suto, Y., et al. 2019, *AJ*, 157, 137
- Karoff, C., Metcalfe, T. S., Chaplin, W. J., et al. 2013, *MNRAS*, 433, 3227
- Kjeldsen, H., & Bedding, T. R. 1995, *A&A*, 293, 87
- Kraft, R. P. 1967, *ApJ*, 150, 551
- Ledoux, P. 1951, *ApJ*, 114, 373

- Lightkurve Collaboration, Cardoso, J. V. d. M., Hedges, C., et al. 2018, Lightkurve: Kepler and TESS time series analysis in Python, Astrophysics Source Code Library, ascl:1812.013
- Lillo-Box, J., Barrado, D., & Bouy, H. 2014, A&A, 566, A103. <https://doi.org/10.1051/0004-6361/201423497>
- Lomb, N. R. 1976, Astrophysics and Space Science, 39, 447. <http://dx.doi.org/10.1007/BF00648343>
- Lund, M. N., Silva Aguirre, V., Davies, G. R., et al. 2017, ApJ, 835, 172
- Mabelcalim. 2014, waipy, <https://github.com/mabelcalim/waipy>, GitHub
- Marcy, G. W., Isaacson, H., Howard, A. W., et al. 2014, ApJS, 210, 20
- McQuillan, A., Mazeh, T., & Aigrain, S. 2013, The Astrophysical Journal Letters, 775, L11
- McQuillan, A., Mazeh, T., & Aigrain, S. 2014, ApJS, 211, 24
- Molenda-Żakowicz, J., Sousa, S. G., Frasca, A., et al. 2013, MNRAS, 434, 1422
- Mosser, B., Michel, E., Belkacem, K., et al. 2013, A&A, 550, A126
- Nielsen, M. B., Gizon, L., Schunker, H., & Karoff, C. 2013, A&A, 557, 10. <http://cdsarc.u-strasbg.fr/viz-bin/qcat?J/A+A/557/L10>
- Nielsen, M. B., Schunker, H., Gizon, L., & Ball, W. H. 2015, Astronomy & Astrophysics, 582, A10. https://www.aanda.org/articles/aa/full/{_}html/2015/10/aa26615-15/aa26615-15.html<https://www.aanda.org/articles/aa/abs/2015/10/aa26615-15/aa26615-15.html>
- Paxton, B., Bildsten, L., Dotter, A., et al. 2011, ApJS, 192, 3
- Petigura, E. A., Howard, A. W., Marcy, G. W., et al. 2017, AJ, 154, 107
- Pinsonneault, M. H., An, D., Molenda-Żakowicz, J., et al. 2012, ApJS, 199, 30
- Reiners, A., & Schmitt, J. H. M. M. 2003, A&A, 412, 813
- Reinhold, T., & Gizon, L. 2015, Astronomy & Astrophysics, 583, A65. <http://www.aanda.org/10.1051/0004-6361/201526216>
- Reinhold, T., & Reiners, A. 2013, Astronomy & Astrophysics, 557, A11. <http://www.aanda.org/10.1051/0004-6361/201321161>
- Reinhold, T., Shapiro, A. I., Solanki, S. K., et al. 2020, Science, 368, 518. <https://www.science.org/doi/abs/10.1126/science.aay3821>
- Santos, A. R. G., Cunha, M. S., Avelino, P. P., García, R. A., & Mathur, S. 2017, A&A, 599, A1. <https://doi.org/10.1051/0004-6361/201629923>
- Santos, A. R. G., García, R. A., Mathur, S., et al. 2019, The Astrophysical Journal Supplement Series, 244, 21. <https://doi.org/10.3847/1538-4365/ab3b56>
- Scargle, J. D. 1982, ApJ, 263, 835
- Schou, J., Antia, H. M., Basu, S., et al. 1998, ApJ, 505, 390
- Skumanich, A. 1972, \apj, 171, 565
- Stumpe, M. C., Smith, J. C., Catanzarite, J. H., et al. 2014, Publications of the Astronomical Society of the Pacific, 126, 100. <https://doi.org/10.1086%2F674989>
- Suto, Y., Kamiaka, S., & Benomar, O. 2019, AJ, 157, 172
- Suto, Y., Sasaki, S., Nakagawa, Y., & Benomar, O. 2022, arXiv e-prints, arXiv:2205.04836
- Tassoul, M. 1980, ApJS, 43, 469
- Thompson, M. J., Christensen-Dalsgaard, J., Miesch, M. S., & Toomre, J. 2003, ARA&A, 41, 599
- Torrence, C., & Compo, G. P. 1998, Bulletin of the American Meteorological Society, 79, 61. <http://paos.colorado.edu/research/wavelets/bams{-}79{-}01{-}0061.pdf><http://journals.ametsoc.org/doi/abs/10.1175/1520-0477{ }281998{ }29079{ }3C0061{ }3AAPGTWA{ }3E2.0.CO{ }3B2>
- Van Eylen, V., Lund, M. N., Silva Aguirre, V., et al. 2014, ApJ, 782, 14
- van Saders, J., Ceillier, T., Metcalfe, T., et al. 2016, \nat, 529, 181
- VanderPlas, J. T. 2018, The Astrophysical Journal Supplement Series, 236, 16. <http://stacks.iop.org/0067-0049/236/i=1/a=16?key=crossref.2d79c6c284b1df1e8149df501e36ea6b><https://iopscience.iop.org/article/10.3847/1538-4365/aab766>
- Wes McKinney. 2010, in Proceedings of the 9th Python in Science Conference, ed. Stéfan van der Walt & Jarrod Millman, 56 – 61
- Winn, J. N., Fabrycky, D., Albrecht, S., & Johnson, J. A. 2010, ApJL, 718, L145
- Wolniewicz, L. M., Berger, T. A., & Huber, D. 2021, The Astronomical Journal, 161, 231. <https://doi.org/10.3847/1538-3881/abee1d>

Zechmeister, M., & Kürster, M. 2009, *Astronomy & Astrophysics*, 496, 577.
<https://www.aanda.org/articles/aa/pdf/2009/11/aa11296-08.pdf><http://www.aanda.org/10.1051/0004-6361:200811296>